



UNIVERSITY OF COPENHAGEN

NIELS BOHR INSTITUTE, FACULTY OF SCIENCE

PROGRESS REPORT CONCLUDING PART A OF THE 4+4 PH.D. PROGRAM

Generation of exotic quantum states in a cold ensemble of Caesium atoms

Stefan Lund Christensen

August 2012

Academic supervisor:
Prof. Eugene S. Polzik

Progress report

Stefan Lund Christensen

Generation of exotic quantum states in a cold ensemble of Caesium atoms

Danish National Research Foundation
Centre for Quantum Optics (QUANTOP)
Niels Bohr Institute
Graduate School of Science
Faculty of Science
University of Copenhagen

Stefan Lund Christensen
Version 1.3 (Submission version),
Copenhagen, August 20, 2012
Copyright ©2012. All rights reserved.

Principal academic supervisor: Prof. Eugene S. Polzik

Additional academic supervisors: Asst. Prof. Jürgen Appel
Assoc. Prof. Jörg H. Müller

External censor : Prof. Michael Drewsen

Submission date : 20th of August 2012

Defence date : 6th of September 2012

Abstract

In this progress report we present results showing the experimental realization of non-classical states in an atomic ensemble. We will consider two such non-classical states, a spin squeezed and a collective single excitation state. To create a spin squeezed state we start from a coherent spin state, which minimizes the Heisenberg uncertainty principle. By performing quantum non-demolition measurements we can reduce the noise of this state below the standard quantum limit. The noise reduction is based on non-classical correlations between the atoms, and we thus conclude that the atomic ensemble is in an entangled state. A description of the experimental setup used to generate a spin squeezed state is presented. This is followed by a discussion of data showing the creation of spin squeezed states with a noise reduction of -1.7 dB in the atomic quadrature operators.

Having shown the realization of such states we turn to atomic Fock states, with a discrete number of excitations in the ensemble. In particular we consider a collective single excitation state. We describe how this non-classical and non-Gaussian state of the ensemble is generated by detection of a single forward scattered photon. Experimental results, showing that we fulfil the main experimental requirements for the creation of this state is presented: state selective excitation, single photon detection and filtering together with a projection noise limited sensitivity. The proposal and preliminary experimental results are supported by a simulation showing the feasibility of the proposed method for creation and detection of the collective single excitation state. This leads us to conclude that we are in a position where the creation of this state is within our reach.

Sammendrag

I denne midtvejsrapport præsenterer vi resultater, der viser den eksperimentielle realisation af ikke-klassiske tilstande i et atomart-ensemble. Vi vil fokusere på sådanne ikke-klassiske tilstande, en spin klemt og en kollektiv enkelt eksitations tilstand. Den spin klemte tilstand skabes ved at foretage kvantemekaniske ikke-destruktive målinger på en koherent spin tilstand i ensemblet. Via disse målinger kan vi reducere støjen af en sådan tilstand under standard kvantegrænsen. Denne reduktion af støjen beror på ikke-klassiske korrelationer imellem atomerne, de er i en sammenfilteret tilstand. En beskrivelse og diskussion af de eksperimentelle metoder brugt til at skabe en spin klemt tilstand fremlægges. Dette efterfølges af en præsentation og diskussion af data, der viser en støjreduktion på -1.7 dB i en af de atomare kvadraturoperatorer.

Efter at have fremlagt den eksperimentelle realisation af en spin klemt tilstand, vil vi beskrive atomare Fock tilstande. Dette er tilstande i det atomare ensemble med et diskret antal eksitationer i ensemblet, vi vil i særdeleshed analysere tilstanden af det atomare ensemble med en enkelt kollektiv eksitation. Denne ikke-Gaussiske og ikke-klassiske tilstand bliver skabt via detektion af en enkelt foton. Eksperimentelle resultater, der viser, at vi opfylder de centrale krav for at skabe og karakterisere denne tilstand, præsenteres og inkluderer selektiv eksitation, detektion og filtrering af enkelte fotoner og sensitivitet, så projektionsstøjen af det atomare ensemble kan opløses. Disse resultater understøttes af en simulation og fra dette kan vi konkludere, at den foreslåede metode til at skabe og detektere den kollektive enkelt eksitations tilstand er mulig, og at det er inden for rækkevidde.

Preface

This progress report is a presentation of my work done at QUANTOP from September 2010 to the end of July 2012, and concludes part A of my 4+4 Ph.D project. Starting with little experience in the field of experimental quantum optics, I would still be stuck trying to find the big on-button for the experiment if it had not been for the help and encouragement of my co-workers. I am especially grateful to Jürgen Appel. During the last two years he has shared his immense knowledge on experimental physics. Whenever I have a problem he somehow always had an idea on how it could be solved. This combined with his patience and willingness in answering my questions has made everything not just easier but also more enjoyable. Much of the work presented here is as much his, as it is my accomplishments.

I would also like to thank my fellow Ph.D. students Heidi L. Sørensen and Jean-Baptiste Béguin for their help in improving several aspects of the experiment, and for always being around to discuss physics. Thanks are also due to Jörg H. Müller for always being willing to offer a help and advice when needed. It is also a pleasure to mention the pioneering experimentalists Daniel Oblak, Patrick Windpassing, Niels Kjærgaard and Anne Louchet-Chauvet for building up the experiment I have been so fortunate to work on.

Last but surely not least I would like to thank my supervisor Eugene Polzik, first for giving me the opportunity to work in the inspiring research environment of QUANTOP, and secondly for always being willing to share his knowledge and view on our research field. Summing all of this up only confirms that, two years ago I made the right choice when I applied for a Ph.D. at QUANTOP, and it is with confidence that I can say that I feel extremely privileged to have two more QUANTOP years left.

Contents

Abstract	iii
Preface	iv
Publications	vii
1 Introduction	1
I Theory	4
2 Atoms	5
2.1 Caesium	5
2.2 Pseudo spin operators	7
2.2.1 Bloch sphere	7
2.3 Atomic noise	9
3 Light	10
3.1 Quantum description of light	10
3.1.1 Fock states	11
3.1.2 Coherent states	11
3.2 Schwinger operators	12
3.3 Light propagation in a MZI	13
4 Light atom interaction	15
4.1 Absorption and phase shift	15
4.2 Quantum non-demolition measurements	17
4.2.1 Spin squeezing by QND measurements	18
4.2.2 Squeezing criteria	19
5 Atomic Fock states	21
5.1 Idealized generation method	21
5.2 Properties	22
II Experiment	25
6 Overview of setup	26
6.1 Atom trapping and cooling	26
6.1.1 Magneto optical trap	27
6.1.2 Dipole trap	28
6.2 MZI setup	29

6.2.1	Probe setup	31
6.2.2	Noise scaling	31
6.2.3	Locking the MZI path length	33
6.3	Microwave	34
7	Calibrations and optimizations	36
7.1	State preparation	36
7.2	Microwave calibrations	37
7.3	Magnetic field calibrations	38
8	Squeezing measurements	41
8.1	Decoherence measurement	41
8.2	Squeezing measurement	42
8.2.1	Quadrature measurements and tomography efficiency . . .	45
9	Towards generation of an atomic Fock state	48
9.1	Implementation in experimental setup	48
9.2	State selective excitation	50
9.3	Single photon detection	52
9.3.1	Filter cavities	53
9.4	Projection noise limited	57
9.5	Simulation	57
III	Outlook	61
10	Conclusion	62
11	Next steps and improvements	63
11.1	Dipole trapped atomic ensemble	63
11.2	Fiber based atomic trap	64
IV	Appendices	67
12	Setup drawings	68
	Bibliography	70

Publications

Submitted

1. T. Kiesel, W. Vogel, S. L. Christensen, J. B. Béguin, J. Appel and E. S. Polzik
Atomic nonclassicality quasiprobabilities
Submitted to *Phys. Rev. Lett.*
2. S. L. Christensen, J. B. Béguin, H. L. Sørensen, E. Bookjans, D. Oblak, J. H. Müller, J. Appel and E. S. Polzik
Towards quantum state tomography of a single polariton state of an atomic ensemble
Submitted to a focus issue of the *New Journal of Physics* on quantum tomography.

In preparation

3. S. L. Christensen, J. B. Béguin, J. Appel and E. S. Polzik
Trapping-light induced thermo-optical effects in tapered nanofibers.
Submitted to *JOSA B*.

Introduction

... quantum phenomena do not occur in a Hilbert space, they occur in a laboratory.

— Asher Peres

Since its birth in the beginning of the last century quantum mechanics have fascinated and frustrated physicists in equal amounts. The main reason for this is the many peculiar features of quantum mechanics, such as entanglement, quantum measurement, the superposition principle and Heisenberg uncertainty relation, all topics which we will be dealing with in this report. We will especially focus on how distinctly non-classical states can be created in a physical system. The system forming the back bone of this report is an atomic ensemble, and we will present results showing the creation and detection of a spin squeezed state together with experimental progress towards the creation and detection of a single collective excitation state in this ensemble.

From the Heisenberg uncertainty principle it is clear that a measurements of an observable always have fluctuations. These fluctuations are inherent in nature and originate from the probabilistic nature of quantum mechanics. More specifically, Heisenberg's uncertainty relations limit the product of the variances of two non-commuting operators. It do *not* limit the fluctuations of a single operator, thus allowing for a noise reduction of one operator accompanied by a corresponding increase in the complementary operator. States in which the fluctuations in one operator are reduced below the standard quantum limit, are said to be squeezed. Such states have been realized in a wide range of different systems [Appel et al. 2009a; Wu et al. 1986; Gross et al. 2010]. In particular we will be squeezing a single component of the pseudo-spin vector describing the atomic ensemble creating *spin* squeezed states. Besides the fundamental interest of these states due to their non-classical properties [Kiesel et al. 2012; Sørensen et al. 2001], spin squeezed states find several applications. With their reduced noise, they can be used for improvements in precision measurements [Wineland et al. 1994]. The improvement of such precision measurement over the last few decades means that the most sensitive measurements performed, in for example atomic clocks, are approaching the standard quantum limit. The use of squeezed states in such precision measurements experiments has been accomplished [Louchet-Chauvet et al. 2010; Wasilewski et al. 2010], and allows for improved sensitivity. The large interest in spin squeezed states has recently culminated in a review article [Ma et al. 2011], presenting an overview of the wide range of research regarding spin squeezed states.

The creation of a spin squeezed state shows excellent control of the experimental apparatus and light atom-interaction, since it requires sensitivity on the scale of the intrinsic quantum mechanical noise. It is thus a good starting point for the

preparation of even more exotic states. In this report we present results regarding states of an atomic ensemble with a discrete number of excitations, with a focus on the state with a single collective excitation. This state is heralded via the detection of a single, forward scattered photon in close analogy to the ideas presented in [Duan et al. 2001] and used in photonic systems [Neergaard-Nielsen et al. 2006; Ourjoumtsev et al. 2007]. The state has a non-Gaussian marginal distribution and a negative Wigner function [Christensen et al. 2012], which is a clear sign of its non-classicality [Kot et al. 2012]. Besides the fundamental interest of this state due to its distinct quantum mechanical features, it finds several applications. It can serve as the needed non-Gaussian resource for quantum information processing applications [Ohliger et al. 2012]. It is a central requirement for hybrid discrete-continuous quantum repeater protocols, and the generation of Schrödinger cat states in the atomic ensemble [Brask et al. 2010]. Using the quantum non-demolition dispersive measurement method that allowed us to create a spin squeezed state, the quantum properties of the collective single excitation state can be characterized. A central point is that our proposal allows for the creation and detection of the single excitation state directly in the atomic ensemble. This has several advantages compared to other methods. First the direct creation in the atomic ensemble with a long coherence times means that heralded state is readily available for on-demand use. Secondly, in comparison to protocols where the quantum state of the atomic ensemble is created by mapping of a photonic state [Choi et al. 2008; Matsukevich et al. 2004] on to the ensemble, our method do not suffer from the inherent loss mechanism in the mapping of a quantum state from light to atoms. Third our state tomography is again done directly in the atomic ensemble in a non-destructive manner, allowing for the state to be used as a resource, in contrast to methods where the atomic state is mapped onto a photonic state which is then characterized [MacRae et al. 2012].

As described above, and hopefully will be clear through out this report, we are today in a position where the generation of quantum states of a wide range of systems is being done on a regular basis. In this respect the opening quote of this report is of utmost relevance. We as researchers are in a position where quantum mechanics have once and for all moved from pen and paper into the laboratory.

Theses

It is good custom to always be clear about what one is doing therefore a short description of the theses and goals of this report is given

- Discussion of the concept of spin squeezed states and how these can be created via quantum non-demolition measurements.
- Using and improving the experimental apparatus, described in [Oblak 2010; Windpassinger 2008], to generate spin squeezed states of the atomic ensemble, of not only the angular uncertainty of the pseudo-spin vector but also in the regularized atomic quadrature operators.
- Description of a collective single excitation state in the atomic ensemble, together with an experimental proposal on the generation and tomography of this state.
- Preliminary experimental results, backed by a simulation, showing the feasibility of the experimental setup to create and detect a collective single excitation state.

Report layout

The report is split into two main parts, one theoretical and one experimental, below a chapter by chapter outline is given.

Chapter 1: We introduce the atomic ensemble, and describe it via pseudo-spin operators and describe the central topic of quantum noise.

Chapter 2: A quantum mechanical description of light is presented, and special care is taken in describing light propagation in a Mach-Zehnder interferometer.

Chapter 3: Having introduced the two systems of interest, light and atoms, we are in this chapter dealing with the interactions between them. We consider the concept of quantum non-demolition measurements, and describe how this allows for the creation of spin squeezed states in the atomic ensemble.

Chapter 4: The collective single excitation state of the atomic ensemble is introduced and a simplified implementation model, based on the DLCZ protocol, is presented. We show how the created state has a clearly non-Gaussian feature and a negative Wigner function.

Chapter 5: A brief overview of the setup is given in which we present the methods used to trap and probe the atomic ensemble.

Chapter 6: We consider both the initial state preparation, calibration of the microwave pulses together with calibrations of the applied magnetic fields.

Chapter 7: We present the experimental method and results showing the creation of a spin squeezed state of the atomic ensemble, one of the main results of the presented work.

Chapter 8: In this chapter preliminary results regarding the creation and detection of the collective single excitation state is presented. A simulation shows that even with the experimental imperfection the created state retains its non-Gaussian features, again a main result of this report.

Chapter 9: This chapter contains the conclusion where we sum up the work done, in respect to the creation of the spin squeezed and single excitation states.

Chapter 10: Finally we give an outlook, where we consider future perspectives for the experiment considered and our new ventures into a light-atom interfaces based on a tapered nanofiber.

Part I
Theory

Atoms

In the front line of today's research into the quantum world many different physical systems are used, this could be all from quantum dots, flux qubits, rare earth doped crystals to ions. In the work presented here we work with an atomic system, which like any other system has both pros and cons. To start with the positive side atomic systems have since the introduction of laser cooling in the early nineties been one of the driving forces for the big subject of quantum technologies. This means that atomic systems are in general very well understood and that we as researchers have a big toolbox of techniques to manipulate atomic systems. On the negative side the properties of atoms are given to us by nature, and if there is something about them which we do not like, there is not much we can do about it. In this chapter we consider the atomic ensemble, which will be a central part of this thesis. We introduce the general framework of atomic pseudo-spin operators together with the Bloch sphere representation which will be used through out this report. At the end we discuss the quantum mechanical noise of atomic states, and introduce the concept of spin squeezed states. Such states are central to the work presented here, and in chapt. 8, we present data showing the creation and characteristic of such a state.

2.1 Caesium

Our atom of choice is the only natural isotope of Caesium (Cs), which has 133 nucleons in its core. Cs is one of the alkali atoms and thus only has a single electron in the outermost shell, here in the h -shell, making it somewhat simple to describe. The level diagram is shown in fig. 2.1, we will mainly be concerned with the ground state, which is the $6S_{1/2}$ manifold. From this state we will be looking at two optical transitions, namely to the $6P_{1/2}$ (D1-line) and to the $6P_{3/2}$ (D2-line). Each of these manifolds (ground, and two excited) are further split due to the different possible alignment configurations of the electron and nucleus spin. To distinguish between those, we introduce the F quantum number. If an external magnetic field is applied the degeneracy of the F states is lifted since the atoms will experience the linear Zeeman¹ shift given by [Steck 2010]

$$\Delta\omega_{Zeeman} = \mu_B g_F m_F B = \pm 2\pi m_F B \cdot 350 \frac{\text{kHz}}{\text{Gauss}}. \quad (2.1)$$

From an experimental point of view, it is already clear that the $m_F = 0$ states are favourable, is since they, to first order, do not experience a Zeeman shift. To simplify the notation we will use the standard bra and ket notation. We write

¹The big problem arises if the magnetic field is inhomogeneous, since this will give a Zeeman shift which is dependent on the spatial position of the atoms.

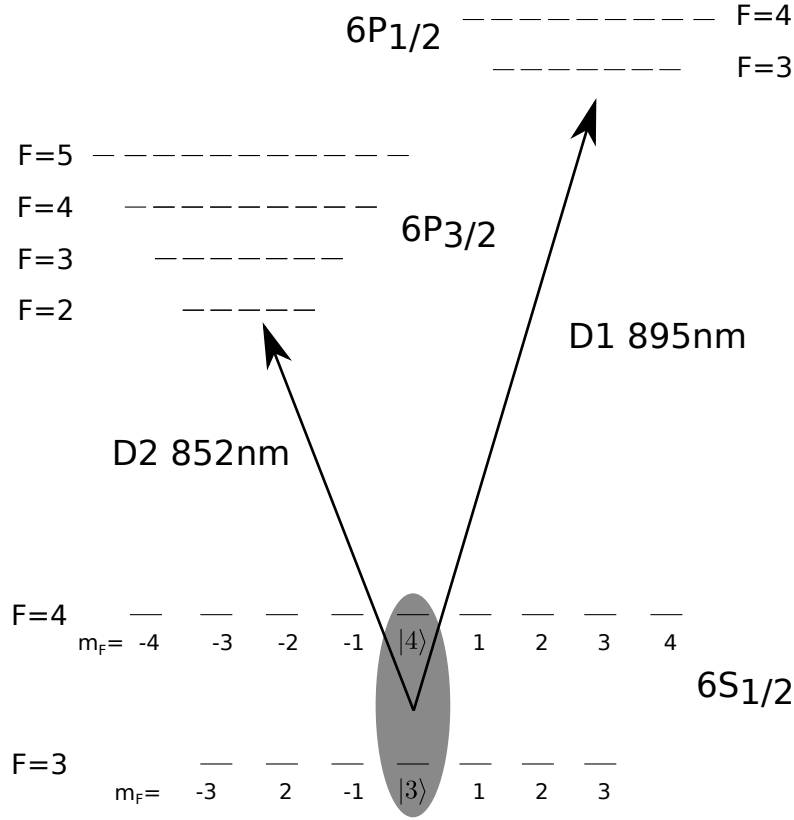


Figure 2.1: A simplified level diagram of Cs, where only the optical D1 and D2 lines are considered.

the atomic state as $|F, m_F\rangle$, and will use a prime to distinguish between ground and excited states. In this work we will mainly be dealing with the so-called clock levels² these are the two hyperfine ground levels ($m_F = 0$) of the $6S_{1/2}$ manifold. Since we will refer to the clock-states over and over again, we introduce the following shorthand notation

$$|3\rangle \equiv |F = 3, m_F = 0\rangle, \quad (2.2a)$$

$$|4\rangle \equiv |F = 4, m_F = 0\rangle. \quad (2.2b)$$

As we know the world is not perfect and to second order the clock levels do experience a quadratic Zeeman shift of $427.45\text{Hz}/\text{Gauss}^2$ [Steck 2010]. This shift has been measured and could be used to calibrate the magnetic field³, see sec. 7.3. Since the atomic states form an orthonormal basis, we can expand any pure, non entangled, state as a linear superposition of the different levels

$$|\Psi\rangle = \sum_{i=1}^{N_{\text{at}}} c_i |\psi\rangle_i, \quad (2.3)$$

where N_{at} is the number of atoms in the ensemble. It is however convenient to use the density matrix formula, since this allows us to describe classical statistical mixtures of states. If we denote the probability of being in a state $|\psi\rangle_i$ with p_i the density operator is for none entangled states given as $\hat{\rho} \equiv \sum_i p_i |\psi\rangle_i \langle\psi|$ [Sakurai 1978]. With the density matrix formalism at hand we are now in a position to introduce atomic operators, namely pseudo-spin operators, which is a standard formalism to describe two level systems.

²Termed so since the definition of the second, and thus time, is defined from the energy difference between these levels.

³In practice we use one of the $|F = 3, m_F = 0\rangle \rightarrow |F = 4, m_F = \pm 1\rangle$ transition since it is much more sensitive.

2.2 Pseudo spin operators

The pseudo-spin operators for the atomic ensemble are introduced for several reasons. They allow us to make a clear analogy between our two level system of choice and the standard spin system of quantum mechanics. Using this analogy we also get a geometrical visualization of the atomic states, through the Bloch sphere picture. Here we will introduce it using the two level system formed by the clock levels of Cs. We define three operators as

$$\hat{f}_x \equiv \frac{1}{2} (|3\rangle\langle 4| + |4\rangle\langle 3|) = \frac{1}{2} (\hat{\rho}_{34} + \hat{\rho}_{43}), \quad (2.4a)$$

$$\hat{f}_y \equiv -\frac{i}{2} (|3\rangle\langle 4| - |4\rangle\langle 3|) = -\frac{i}{2} (\hat{\rho}_{34} - \hat{\rho}_{43}), \quad (2.4b)$$

$$\hat{f}_z \equiv \frac{1}{2} (|4\rangle\langle 4| - |3\rangle\langle 3|) = \frac{1}{2} (\hat{\rho}_{44} - \hat{\rho}_{33}). \quad (2.4c)$$

Note that \hat{f}_z is half of the population difference between the two clock levels. It is straightforward to show that the above operators satisfy angular momentum like commutation relations

$$[\hat{f}_i, \hat{f}_j] = i\epsilon_{ijk}\hat{f}_k, \quad (2.5)$$

where ϵ_{ijk} is the Levi-Civita tensor. Thus the operators are members of the SU(2) group [Sakurai 1978] just like the normal Cartesian spin components. In analogy with this we form the *pseudo-spin* vector as

$$\hat{\mathbf{f}} \equiv \begin{pmatrix} \hat{f}_x \\ \hat{f}_y \\ \hat{f}_z \end{pmatrix}. \quad (2.6)$$

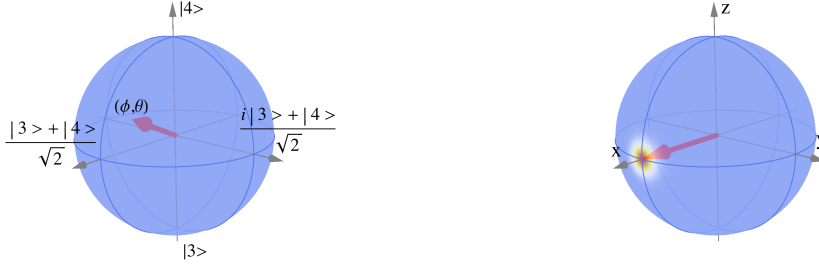
In our experiment we will *not* be dealing with a single atom but instead an ensemble with $N_{\text{at}} \approx 10^5$ atoms. When we perform a measurement we will always be dealing with the *collective* state of the ensemble. To get collective ensemble operators one simply sums up the individual atomic operators i.e

$$\hat{F}_i \equiv \sum_{j=1}^{N_{\text{at}}} \hat{f}_i^{(j)} \text{ for } i = x, y, z, \quad (2.7)$$

and where $\hat{f}_i^{(j)}$ is the pseudo spin operator of the j -th atom. The total ensemble operators are still in the SU(2) group, i.e. they have angular momentum like commutation relations and we can again form a pseudo-spin vector $\hat{\mathbf{F}}$. We note that the operators \hat{F}_x, \hat{F}_y and \hat{F}_z are symmetric under particle exchange and that \hat{F}_z is half of the ensemble population difference. It is exactly the population difference which will be the central parameter of the atomic ensemble, and it is what we will be measuring through out this report.

2.2.1 Bloch sphere

To describe how a spin-1/2 system evolves in an external magnetic field Felix Bloch introduced what is now known as the Bloch sphere representation. This representation is now a standard way used to describe two level systems be it spins, atoms or qubits. It is a mapping of the pseudo-spin vector onto a unit sphere. We recall that unitary operations, thus time evolution, are trace and norm preserving [Sakurai 1978]. This means that the vector $\hat{\mathbf{F}}$ does *not* change its length but the ratio of its components can change making the vector trace out a path on a sphere (of fixed radius) over time. Note that the length of the pseudo-spin vector, $|\hat{\mathbf{F}}|$, is proportional to the total number of atoms. As an example we discuss how to represent the coherent superposition state (CSS) of the ensemble.



(a) A Bloch sphere where the position of some of the central states are situated. We note how the equatorial plane describes even superposition states.

(b) A Bloch sphere with an error disk drawn at the tip of the Bloch vector, to illustrate the probabilistic nature of quantum mechanics manifesting itself as projection noise.

Figure 2.2: Examples of the Bloch sphere representation.

Coherent superposition states

One of the simplest collective ensemble states is a product state of identical single atomic states, i.e. $|\Psi\rangle = \prod_{i=1}^{N_{\text{at}}} |\psi\rangle_i$. For a two level systems we can write a general state as [Nielsen et al. 2000]

$$|\psi\rangle_i = \cos\left(\frac{\theta}{2}\right) |4\rangle_i + e^{i\phi} \sin\left(\frac{\theta}{2}\right) |3\rangle_i, \quad (2.8)$$

which is parametrized by the two angles ϕ and θ . In order to represent this on the Bloch sphere we calculate the expectation values ($\langle \cdot \rangle$) for each component of the collective ensemble pseudo-spin vector

$$\langle \hat{F}_x \rangle = \frac{N_{\text{at}}}{2} \sin(\theta) \cos(\phi), \quad (2.9a)$$

$$\langle \hat{F}_y \rangle = \frac{N_{\text{at}}}{2} \sin(\theta) \sin(\phi), \quad (2.9b)$$

$$\langle \hat{F}_z \rangle = \frac{N_{\text{at}}}{2} \cos(\theta). \quad (2.9c)$$

Thus we can describe the ensemble state by its length (atom number) and the two angles θ and ϕ . To get a bit of intuition we can now simply compute the above expectation values for different angles. If we take $\theta = 0$ we have $\langle \hat{F}_x \rangle = \langle \hat{F}_y \rangle = 0$ and $\langle \hat{F}_z \rangle = N_{\text{at}}/2$ i.e the pseudo-spin vector points to the north pole of the Bloch sphere and from eq. (2.8) we see that all atoms are in the upper clock state, $|4\rangle$. Taking $\theta = \pi$ instead, all the atoms are in the lower state, $|3\rangle$ and the pseudo-spin vector is pointing to the south pole. If we now look at $\theta = \pi/2$ we get the single atomic state

$$|\psi\rangle = \frac{1}{\sqrt{2}} \left(|3\rangle + e^{i\phi} |4\rangle \right), \quad (2.10)$$

an equal superposition of being in the upper and lower clock level. The pseudo-spin vector now takes the form $\langle \hat{F}_x \rangle = N_{\text{at}} \cos(\phi)/2$, $\langle \hat{F}_y \rangle = N_{\text{at}} \sin(\phi)/2$ and $\langle \hat{F}_z \rangle = 0$, which corresponds to the pseudo-spin vector being in the equatorial plane. States corresponding to the different positions on the Bloch sphere are shown on fig. 2.2(a). Before we can get a complete handle on the atomic state, we still need to consider the probabilistic nature of quantum mechanics, which gives notion to the so-called quantum noise.

2.3 Atomic noise

A central part of the work described in this report, is the quantum noise of the atomic ensemble, what we shall term as the atomic projection noise. In this section we, for the first time, consider this intrinsic quantum mechanical noise of the atomic ensemble. In the experiment it is exactly these noise properties of the system we will be measuring, and allowing us to describe the quantum mechanical state of the ensemble. To start this discussion we cut straight to the case, and consider the Heisenberg uncertainty relation

$$\text{var}(\hat{\delta}_i) \cdot \text{var}(\hat{\delta}_j) \geq \frac{1}{4} |\langle [\hat{\delta}_i, \hat{\delta}_j] \rangle|^2. \quad (2.11)$$

Where the variance of an operator is given as

$$\text{var}(\hat{\delta}) \equiv \langle \hat{\delta}^2 \rangle - \langle \hat{\delta} \rangle^2. \quad (2.12)$$

Since the three components of the pseudo-spin vector do not commute, eq. (2.5), it is clear that we must assign some uncertainty to the pseudo-spin vector. A central point comes by noting that the above inequality does not set any lower bound on the variance of the individual operators. We are thus allowed to reduce the variance of one operator below the right hand side, as long as the variance of the complementary operator increases accordingly. This is exactly what we will exploit to create spin squeezed states [Kitagawa et al. 1993]. If we once again consider the CSS with the individual atomic states given by the general two level state described by eq. (2.8) we can calculate the variance of each of the pseudo-spin vector components. The $\langle \hat{F}_i \rangle^2$ term in eq. (2.12) is trivial to compute given that we have the expectation values from eq. (2.9). The $\langle \hat{F}_i^2 \rangle$ is found by noting that

$$\hat{f}_i^2 = \frac{1}{4} (|4\rangle\langle 4| + |3\rangle\langle 3|), \quad (2.13)$$

for $i = x, y, z$. Assuming that the atomic ensemble is in a product state (no correlations between the atoms) we find

$$\text{var}(\hat{F}_x) = \frac{N_{\text{at}}}{4} [1 - \sin^2(\theta) \cos^2(\phi)], \quad (2.14a)$$

$$\text{var}(\hat{F}_y) = \frac{N_{\text{at}}}{4} [1 - \sin^2(\theta) \sin^2(\phi)], \quad (2.14b)$$

$$\text{var}(\hat{F}_z) = \frac{N_{\text{at}}}{4} [1 - \cos^2(\phi)]. \quad (2.14c)$$

To incorporate this uncertainty into our Bloch sphere representation we will draw an ellipse (circle for non-squeezed states), at the tip of the pseudo-spin vector given by eq. (2.14) see fig. 2.2(b).

Before we proceed it is important to note that it is customary to give measurement precision *not* in terms of the variance but by the standard deviation

$$\text{stdev}(\hat{\delta}) \equiv \sqrt{\text{var}(\hat{\delta})}. \quad (2.15)$$

Since the spin magnitude (signal) is proportional to N_{at} and the measurement uncertainty or standard deviation (noise) grows with $\sqrt{N_{\text{at}}}$ one can always increase the measurement precision (signal to noise ratio) by measuring on a larger ensemble. This point will especially be relevant when we have to quantify the amount of squeezing obtained, see sec. 4.2.2.

Light

After having considered the atoms we now turn to the second central system in our experiment, namely light. In our experiment light is used to measure the internal state of the atoms, through the state dependent atomic phase shift imprinted on a light pulse passing through the atomic ensemble. Due to the high sensitivity required to resolve the atomic projection noise it is of utmost importance that we understand and are able to control the light and especially its fluctuations. In this chapter we introduce the quantum mechanical description of the electro-magnetic field together with its noise properties. A central point of this chapter is the description of a light mode as it propagates in a Mach-Zender interferometer (MZI). Via the MZI we measure the relative phase between of light propagating in its two arms. If an atomic ensemble is situated in one arm and the other propagate in free space, one can (if not limited by anything else) measure the atomic phase shift. In this chapter we will take the liberty to cut corners and focus on the most important features for the work presented. The discussion will be largely based on [Oblak 2010; Windpassinger 2008].

3.1 Quantum description of light

With the emergence of quantum optics it quickly became clear that light, when considered on the level of single photons, has very strange and unintuitive properties¹, many of which originate from the quantization of light. Here we will just jump ahead and postulate that the electro magnetic field can be described by the following Hamiltonian

$$\hat{\mathcal{H}} = \hbar\omega \left(\hat{a}_{k,s}^\dagger \hat{a}_{k,s} + \frac{1}{2} \right) \quad (3.1)$$

where $\hat{a}_{k,s}^\dagger$ is the creation operator for a photon of frequency ω in the mode defined by the wave vector k and polarization $\varepsilon_{k,s}$, and $\hat{a}_{k,s}$ is the annihilation operator for the same mode. The two operators do not commute, $[\hat{a}, \hat{a}^\dagger] = 1$ and are non-hermitian. Noting that $\hbar\omega$ is the energy of a single photon leads to the definition of the photon number operator as

$$\hat{N}_{\text{ph},k,s} \equiv \hat{a}_{k,s}^\dagger \hat{a}_{k,s} \quad (3.2)$$

We see the appearance of the zero point energy given by the last term in eq. (3.1), this means that even the electro-magnetic mode with no photons will carry energy, this is what we now know as the vacuum energy. We now turn to the question of which basis states to use, and will introduce the two standard bases for light. We start by considering the Fock states.

¹This could be: photon bunching, and Hong-Ou-Mandel experiments.

3.1.1 Fock states

A natural basis for the electro-magnetic field is the Fock states, $|n\rangle$, also known as number states. They are defined such that²

$$\hat{a}^\dagger |n\rangle = \sqrt{n+1} |n+1\rangle, \quad (3.3a)$$

$$\hat{a} |n\rangle = \sqrt{n} |n-1\rangle, \quad (3.3b)$$

$$\hat{a} |0\rangle = 0. \quad (3.3c)$$

From this it is clear that the Fock states are also the energy eigenstates³

$$\hat{\mathcal{H}} |n\rangle = E_n |n\rangle, \quad E_n = \hbar\omega \left(n + \frac{1}{2} \right). \quad (3.4)$$

The Fock states are a good basis if one is concerned with the quantum features of light. From an experimental point of view they are far from the output of lasers, in order to describe this we introduce the coherent states.

3.1.2 Coherent states

There are several ways of defining the coherent states. Here we will follow the approach taken in [Gerry et al. 2005], and define them as eigenstates of the photon annihilation operator⁴

$$\hat{a} |\alpha\rangle = \alpha |\alpha\rangle. \quad (3.5)$$

From which it is clear that $\langle \alpha | \hat{N}_{\text{ph}} | \alpha \rangle = |\alpha|^2$, this is the mean photon number in a coherent state and it is denoted by \bar{n} . A very useful thing to have in mind is that the coherent light states are displaced vacuum states [Leonhardt 1997]

$$|\alpha\rangle = \hat{D}_\alpha |0\rangle \quad (3.6)$$

where

$$\hat{D}_\alpha = \exp \left[\alpha \hat{a}^\dagger - \alpha^* \hat{a} \right]. \quad (3.7)$$

The last thing we calculate is the fluctuations of the photon number for the coherent states. Using the commutation relation we quickly find

$$\langle \alpha | \hat{N}_{\text{ph}}^2 | \alpha \rangle = \langle \alpha | \hat{a}^\dagger \hat{a} \hat{a}^\dagger \hat{a} | \alpha \rangle \quad (3.8a)$$

$$= \langle \alpha | \hat{a}^\dagger \hat{a}^\dagger \hat{a} \hat{a} + \hat{a}^\dagger \hat{a} | \alpha \rangle \quad (3.8b)$$

$$= \bar{n}^2 + \bar{n}. \quad (3.8c)$$

From this we easily calculate the variance of the photon number in the coherent states as

$$\text{var}(\hat{N}_{\text{ph}}) = \bar{n}. \quad (3.9)$$

These fluctuations are what we will term as light shot noise, and it is these fluctuations which in the end will limit our readout of the atomic states. The reason for this is that to preserve the desired non-destructiveness of our measurement we need to put an upper limit on the number of photons used. From the fluctuations of the photon number the corresponding fluctuations of the quadrature variables of light can be calculated [Gerry et al. 2005]. It is found that the coherent states minimize the Heisenberg uncertainty relation and are thus termed minimum uncertainty states. These properties make the coherent states the quantum analogue of classical light states and it is the best description of laser

²When we consider atomic fock states we will see similar equations.

³Eigenstates of the Hamiltonian and photon number operator \hat{N}_{ph} .

⁴We have suppressed the subscripts for notational clarity.

light. The analogy between the coherent light states and coherent superposition states in the atomic ensemble is clear. Both are minimum uncertainty states of the relevant quadrature operators⁵, and can be created by displacing the vacuum state. The similarities between the description of light and atoms, will be present through out this report. Just as for the atomic ensemble we introduce a new set of operators which is more favourable when we describe the use of light as a meter.

3.2 Schwinger operators

In the experimental setup we consider two light modes, one for each arm of the MZI. In this respect a standard formalism is that of Schwinger operators [Schwinger 1952] also known as light pseudo-spin operators

$$\hat{S}_x \equiv \frac{1}{2} (\hat{a}^\dagger \hat{b} + \hat{b}^\dagger \hat{a}) \quad (3.10a)$$

$$\hat{S}_y \equiv -\frac{i}{2} (\hat{a}^\dagger \hat{b} - \hat{b}^\dagger \hat{a}) \quad (3.10b)$$

$$\hat{S}_z \equiv \frac{1}{2} (\hat{a}^\dagger \hat{a} - \hat{b}^\dagger \hat{b}), \quad (3.10c)$$

having angular momentum like commutation relations⁶ i.e $[\hat{S}_i, \hat{S}_j] = i\epsilon_{ijk}\hat{S}_k$. Together with the *total* photon number operator $\hat{N}_{\text{ph}} \equiv \hat{N}_{\text{ph},a} + \hat{N}_{\text{ph},b}$. We note the analogy to the Bloch vector description of atoms, and see that if we form the vector

$$\hat{\mathbf{S}} = \begin{pmatrix} \hat{S}_x \\ \hat{S}_y \\ \hat{S}_z \end{pmatrix}, \quad (3.11)$$

We can also visualise the light state on a ‘‘Bloch’’ sphere representation. Before we turn to the question of how to describe light propagating in a MZI, we make a quick remark about quantum fluctuations.

Just as it was the case for the atomic operators the Schwinger operators will have an associated noise, originating from Heisenberg uncertainty relations, see eq. (2.11). Using the commutator for the Schwinger operators we find that

$$\text{var}(\hat{S}_i) \cdot \text{var}(\hat{S}_j) \geq \epsilon_{ijk}^2 \frac{\langle \hat{S}_k \rangle}{4}. \quad (3.12)$$

We will be measuring the difference in photon number between the two modes i.e $\langle \hat{S}_z \rangle$ which has the noise

$$\text{var}(\hat{S}_i) = \frac{1}{4} \bar{n}, \quad (3.13)$$

where \bar{n} is the mean photon number, i.e. the expectation value of \hat{N}_{ph} . It is thus clear that the measurement on the light, which we use to deduce the population difference in the ensemble, also have quantum fluctuations. In the final experiment we will keep the number of photons fixed, and we thus expect the contribution of light noise to be constant as the number of atoms is varied.

⁵We will introduce the atomic quadrature operators in the Holstein-Primakoff approximation in sec. 8.2.1

⁶Either one quickly notes the similarity to the Pauli spin operators or simply employ the known commutation relations for \hat{a} and \hat{a}^\dagger .

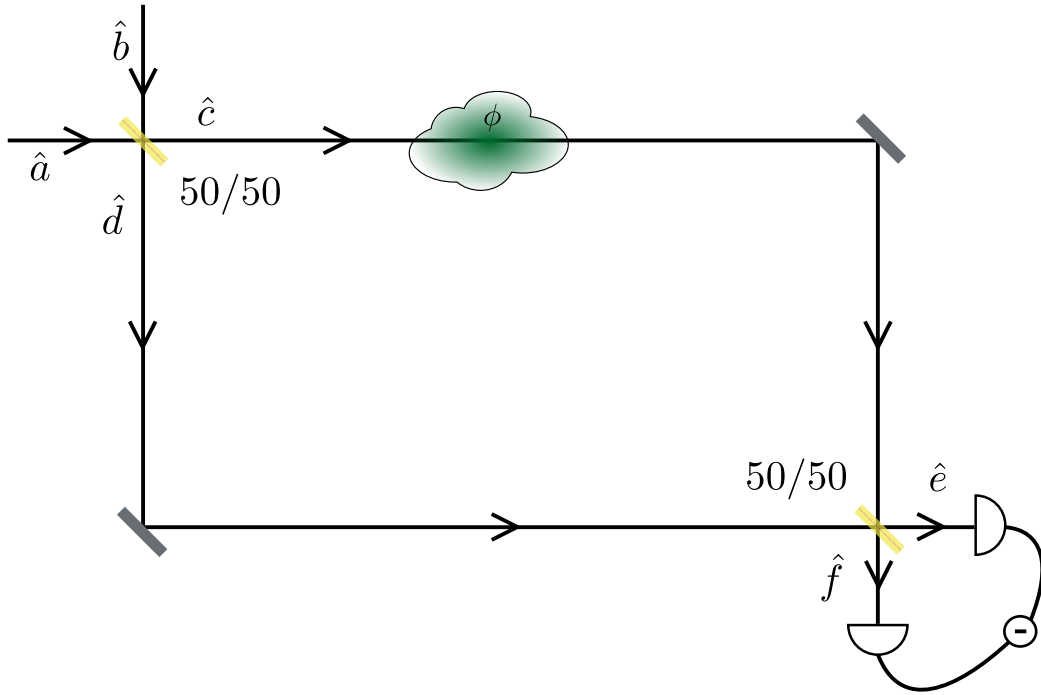


Figure 3.1: Schematic for the theoretical description of the MZI based on different light modes.

3.3 Light propagation in a MZI

Having briefly introduced the standard formalism for the quantum mechanical description of light, we now turn to a more specific setting (and maybe unfamiliar setting for the reader), namely propagation in a MZI. As with much else in this report, we will follow [Windpassinger 2008; Oblak 2010]. A schematic of the idea about a MZI is seen in figure 3.1, it consists of two symmetric 50/50 beam splitters and a variable phase shift in one arm, denoted by ϕ . It is pointed out that in the experiment the first beam splitter is *not* a 50/50 beam splitter, as described in sec. 6.2. The reason that the case of a 50/50 beam splitter is still worth considering is that it nice illustrates how the MZI can be used to measure the atomic phase shift. In the experiment, ϕ will be due to the atomic cloud and depends on the internal atomic state. Before we put it all together we consider the elements one by one. If we know the annihilation and creation operators for a given mode at a certain point, in the MZI, we can always compute the Schwinger operators. Considering the symmetric 50/50 beam splitter it is a standard result that⁷

$$\begin{pmatrix} \hat{c} \\ \hat{d} \end{pmatrix} = \frac{1}{\sqrt{2}} \begin{pmatrix} 1 & i \\ i & 1 \end{pmatrix} \begin{pmatrix} \hat{a} \\ \hat{b} \end{pmatrix}. \quad (3.14)$$

Now the two modes acquire a differential phase shift, due to the different optical lengths $\delta l = \frac{\lambda}{2\pi}\phi$ in the two arms. Again using the matrix representation we can write this as

$$\begin{pmatrix} \hat{c}' \\ \hat{d}' \end{pmatrix} = \begin{pmatrix} e^{i\phi/2} & 0 \\ 0 & e^{-i\phi/2} \end{pmatrix} \begin{pmatrix} \hat{c} \\ \hat{d} \end{pmatrix}, \quad (3.15)$$

we note that for simplicity we have divide the total relative phase shift of ϕ into a phase shift of $\phi/2$ in of each mode \hat{c} and \hat{d} . As it is clear from eq. (3.10) we can now compute the corresponding transformations in terms of the Schwinger

⁷For definitions of the transmitted and reflected modes see fig. 3.1.

operators and find that a 50/50 beam splitter is described by

$$\begin{pmatrix} \hat{S}_x \\ \hat{S}_y \\ \hat{S}_z \end{pmatrix}_{\text{out}} = \begin{pmatrix} 1 & 0 & 0 \\ 0 & 0 & 1 \\ 0 & -1 & 0 \end{pmatrix} \begin{pmatrix} \hat{S}_x \\ \hat{S}_y \\ \hat{S}_z \end{pmatrix}_{\text{in}}, \quad (3.16)$$

and for the differential phase shift

$$\begin{pmatrix} \hat{S}_x \\ \hat{S}_y \\ \hat{S}_z \end{pmatrix}_{\text{out}} = \begin{pmatrix} \cos(\phi) & \sin(\phi) & 0 \\ -\sin(\phi) & \cos(\phi) & 0 \\ 0 & 0 & 1 \end{pmatrix} \begin{pmatrix} \hat{S}_x \\ \hat{S}_y \\ \hat{S}_z \end{pmatrix}_{\text{in}}. \quad (3.17)$$

With the above description in terms of transformation matrices and the input and output vectors all we need to do in order to track the light modes through the MZI is a bit of matrix multiplication. To get a feel for how this all works we look at the example of having a coherent state as an input in mode \hat{a} and vacuum in mode \hat{b} . As always we can then write the total input state as the tensor product $|\psi\rangle_{\text{in}} = |\alpha\rangle_a \otimes |0\rangle_b$. In the following we suppress the tensor product for notional simplicity. With this input state we can calculate the desired Schwinger operators and find

$$\hat{\mathbf{S}}_{\text{in}} = \begin{pmatrix} 0 \\ 0 \\ \frac{|\alpha|^2}{2} \end{pmatrix}. \quad (3.18)$$

If we do the calculation using the beam splitter relation in eq. (3.14), one (to little surprise) find that the input gets split evenly between both outgoing modes. The next thing to consider is the differential phase shift here chosen to be $\phi = \pi/2$, which changes the ratio between the \hat{S}_x and \hat{S}_y components. Again performing the transformation of the 50 : 50 beam splitter and measuring the photon number difference i.e \hat{S}_z we get zero mean value. As described in sec. 3.2 the measurement will fluctuate due to the shot noise of light. Now turning to the case of greatest interest for the work presented here where ϕ is due to the atomic induced phase shift. With this the differential phase shift becomes $\phi = \pi/2 + \phi_{\text{atoms}}$, where the $\pi/2$ comes from the path-length difference in the absence of atoms. Doing the same calculations and then measuring \hat{S}_z we get

$$\langle \hat{S}_z \rangle = \frac{1}{2} N_{\text{ph}} \sin(\phi_{\text{atoms}}), \quad (3.19)$$

which is the normal interference fringe that. As mentioned earlier the first beam splitter in the experimental setup is not symmetric with a 50/50 splitting ration, instead it is closer to 90/10. The introduction of this strong reference beam is made in analogy to optical homodyne detection, as described in sec. 6.2, and allows us to gain a factor ≈ 2 in sensitivity. Having now introduced the two systems of interest, light and atoms, we now turn to the question of what will happen when the two interact.

Light atom interaction

Having now introduced the two systems, light and atoms, separately we will in this chapter consider how the two systems interact. It is shown how light passing through an atomic ensemble experience both absorption and a phase shift depending on the internal atomic state. By measuring this atomic induced phase shift, we can infer the population difference in the ensemble, which is proportional to the z -component of the pseudo-spin vector, \hat{F}_z , of the atomic ensemble. In this way we can characterize the quantum mechanical properties of the ensemble. In the second part of this chapter we introduce the concept of quantum non-demolition (QND) measurements. In particular we consider how such QND measurements allow for the creation of a spin squeezed state of the atomic ensemble. As with many other parts of the theory part, a lot of calculations have been written down by my predecessors and we will here just outline the key formulas and for details refer to [Oblak 2010; Windpassinger 2008].

4.1 Absorption and phase shift

In the following we consider a two level system consisting of the states $|g\rangle$ and $|e\rangle$ interacting with a electro-magnetic field, of frequency ω , the Hamiltonian for the system of interest is

$$\hat{\mathcal{H}}_{\text{tot}} = \hat{\mathcal{H}}_{\text{atom}} + \hat{\mathcal{H}}_{\text{light}} + \hat{\mathcal{H}}_{\text{int}}, \quad (4.1)$$

where we will focus on the interaction Hamiltonian, since this contains all the interesting dynamics. In the dipole and rotating wave approximation¹ the interaction is given as

$$\hat{\mathcal{H}}_{\text{int}} = \hbar g \left(\hat{a} \hat{\rho}_{eg} + \hat{a}^\dagger \hat{\rho}_{ge} \right), \quad (4.2)$$

where

$$\hat{\rho}_{ij} \equiv |i\rangle \langle j|. \quad (4.3)$$

We have introduced the coupling constant g , given in terms of the dipole matrix element

$$g = -\sqrt{\frac{\omega}{2\epsilon_0 V \hbar}} \boldsymbol{\varepsilon} \cdot \mathbf{d}_{eg}, \quad (4.4)$$

where V is the mode volume, $\boldsymbol{\varepsilon}$ the polarization vector and the dipole matrix element is

$$\mathbf{d}_{eg} = \langle e | e \hat{\mathbf{x}} | g \rangle. \quad (4.5)$$

¹In which we have averaged out fast oscillating terms $\approx 2\omega$ by using slowly varying operators.

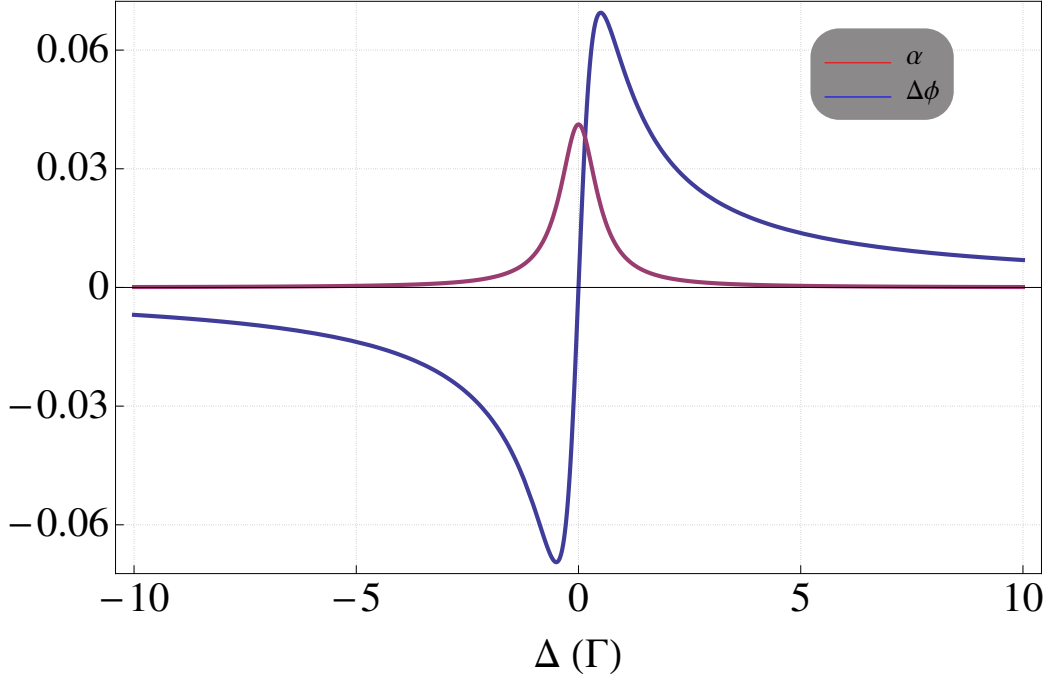


Figure 4.1: A plot of the absorption and phase shift as a function of detuning, note that we have only considered a single resonance in this plot.

Here \hat{x} is the operator valued position vector between the nucleus and electron. We see that a creation of a photon happens if the atom goes from the excited to the ground state and that an annihilation (absorption) of a photon correspond to the atom going from the ground to excited state. Knowing the full Hamiltonian and using the Heisenberg equation of motion

$$\frac{\partial}{\partial t} \hat{O}(t) = \frac{i}{\hbar} [\hat{\mathcal{H}}_{\text{tot}}, \hat{O}(t)] \quad (4.6)$$

we can calculate the time evolution of all the light and atom operators. Extending the discussion to an ensemble of finite length l_a and adding the decay rates manually we find the time evolution of the electric magnetic field as [Oblak 2010, chap. 4]

$$\hat{a}(t) = \hat{a}(t=0) \exp \left[-i\omega t + g^2 \frac{-i\Delta + \Gamma/2}{\Delta^2 + (\Gamma/2)^2} (\hat{\rho}_{gg} - \hat{\rho}_{ee}) t \right] \quad (4.7a)$$

$$= \hat{a}(t=0) \exp [-i(\omega t + \Delta\phi) - \alpha], \quad (4.7b)$$

where $\Gamma = 5.2 \text{ MHz}$ is the natural linewidth and we have introduced

$$\Delta\phi = g^2 \frac{\Delta}{\Delta^2 + (\Gamma/2)^2} (\hat{\rho}_{gg} - \hat{\rho}_{ee}) t \quad (4.8a)$$

$$\alpha = -g^2 \frac{\Gamma/2}{\Delta^2 + (\Gamma/2)^2} (\hat{\rho}_{gg} - \hat{\rho}_{ee}) t. \quad (4.8b)$$

From equation eq. (4.7b) it is clear that we can interpret α as an attenuation i.e absorption of the light field and $\Delta\phi$ as a phase shift. A plot showing the absorption and phase shift as a function of detuning is seen in fig. 4.1

There are a few things to note, first of all both $\Delta\phi$ and α are dependent on the population in the ground states, which is the quantity of interest. A more subtle thing is the different scaling with the detuning. We will be interested in quantum coherences which gets destroyed by spontaneous scattering events (absorption of

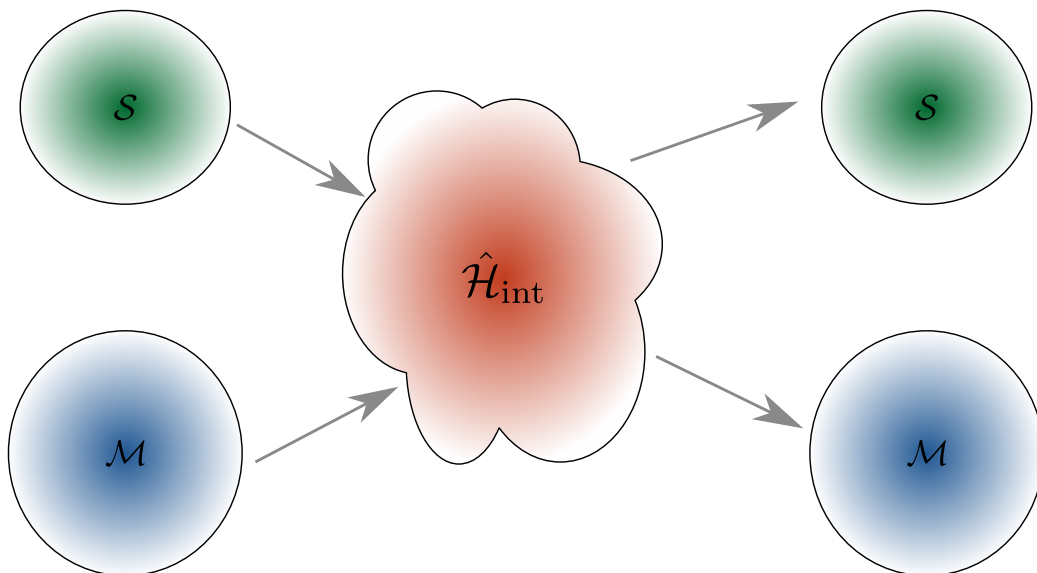


Figure 4.2: Schematic of how we describe a quantum mechanical measurement. First the meter and system are separated, we then let them interact via the Hamiltonian $\hat{\mathcal{H}}_{\text{int}}$ and afterwards, the two now in general entangled systems, are again separated. Lastly a projective measurement is performed on the meter.

photons). If one detunes far enough from resonance we can suppress these events (scaling as Δ^{-2}) while still keeping information about the population difference by measuring the phase shift (scaling as Δ^{-1} as $\Delta \rightarrow \pm\infty$). It is important to note that the quantity of interest for optimal squeezing is the signal to noise ratio. If we are detuned by several linewidth then this quantity is approximately constant (see fig. 4.1) and there is thus no gain in detuning even further [Appel et al. 2009a].

In order to take into account the full atomic structure (D1 and D2 lines) of the Cs atoms, we can sum over all these states weighted with the corresponding transition strengths [Windpassinger 2008; Oblak 2010]. In the experiment we will use a dual color probing scheme where one color probes the atoms in $|4\rangle$ and a different color probes atoms in $|3\rangle$. Since the frequency difference between these states (and thus the two lasers) is $\nu_{\text{clock}} \approx 9$ GHz they will not affect atoms in the other level, allowing us to treat them independently. One can write out explicit formulas for this and the interested reader is encouraged to look at the much more thorough discussion given in [Windpassinger 2008; Oblak 2010].

4.2 Quantum non-demolition measurements

The idea of quantum non-demolition (QND) measurements was first introduced around 20 years ago and has since been a driving force in the continued exploration of the quantum world. Before we continue to the main topic of this section we first describe how we can model quantum mechanical measurements. Consider the system, \mathcal{S} , when doing a measurement we are interested in estimating the mean value of a given observable². To extract this information we let the system interact with our chosen meter \mathcal{M} , and describe this interaction by the Hamiltonian $\hat{\mathcal{H}}_{\text{int}}$ see fig. 4.2. Lastly a projective measurement is performed on the meter.

In the above model any measurement can disturb the system by introduce extra quantum fluctuations. This means that if a subsequent measurement is

²In our case this will be the ensemble population difference, $\propto \hat{F}_z$

performed on the system it might not give the same result, we say that the measurement destroys the system. As the name suggest in QND measurements we are interested in the case where this does not happen. We will consider the situation where a measurement of an observable $\hat{O}(t)$ is performed at time t and again later at time t' the same result is obtained. An equivalent statement is

$$[\hat{O}(t), \hat{O}(t')] = 0, \quad (4.9)$$

for all times t and t' . We call $\hat{O}(t)$ a QND observable and an example of such a observable would be a constant of motion. It follows directly from the Heisenberg equation of motion, see eq. (4.6), that if an observable \hat{O} is a constant of motion then

$$[\hat{\mathcal{H}}_{\text{tot}}, \hat{O}(t)] = 0. \quad (4.10)$$

It has been shown that the above condition can be relaxed to [Poizat et al. 1994]

$$[\hat{\mathcal{H}}_{\text{int}}, \hat{O}(t)] = 0. \quad (4.11)$$

Having now established the criteria for a QND measurement we need to quantify them, which is done by three different measures

Measurement efficiency: Correlations between the meter *after* the interaction and the system value of interest *before* the interaction.

Back action: How much extra noise does the measurement introduce in the system i.e correlation of the system value of interest before and after the system meter interaction.

State preparation: Correlations between meter and system variable *after* the interaction [Walls et al. 2008].

With the ideas about QND measurements we now describe how these can be used to generate spin squeezed states of the atomic ensemble.

4.2.1 Spin squeezing by QND measurements

In order to show how a QND measurement can create spin squeezed states³ we follow the approach in [Oblak 2010; Hammerer et al. 2010] and consider the simple interaction Hamiltonian that couples the z-component of two spins \hat{S}_z and \hat{F}_z together

$$\hat{\mathcal{H}}_{\text{int}} = k\hat{S}_z\hat{F}_z, \quad (4.12)$$

where the coupling strength is given by k . Assuming that both spins have large angular momenta aligned into the y -direction we can treat \hat{S}_y and \hat{F}_y classical and only consider the quantum nature of the x and z components of the two spins⁴. Using the Heisenberg equations of motion we can find input output relations given by ($\hbar = 1$)

$$\hat{F}_x^{\text{out}} = \hat{F}_x^{\text{in}} - k\hat{F}_y^{\text{in}}\hat{S}_z = \hat{F}_x^{\text{in}} - k\frac{N}{4}\hat{S}_z^{\text{in}}, \quad (4.13a)$$

$$\hat{F}_z^{\text{out}} = \hat{F}_z^{\text{in}}, \quad (4.13b)$$

³In sec. 8.2 we will present a related calculation in the context of two sub-sequent measurements on the atomic ensemble, which also shows the spin squeezing can be obtained via QND measurements.

⁴In effect this is the Holstein-Primakoff approximation.

where we have used

$$\langle \hat{F}_y \rangle = \frac{N}{4}. \quad (4.14)$$

Since the two spins enters symmetric in the interaction Hamiltonian similar equations holds for the other spin (with the replacement $N \rightarrow n$). We will now consider the variances of \hat{F}_x^{out} and \hat{F}_z^{out} *conditioned* on a detection of \hat{S}_x giving x_s . These variances are computed for the general case in [Hammerer et al. 2010], and after a somewhat lengthy calculation we find [Oblak 2010, sec. 5.1.1]

$$\text{var}(\hat{F}_x) = (1 + \kappa^2) \frac{N}{4} \quad (4.15a)$$

$$\text{var}(\hat{F}_z) = \frac{1}{1 + \kappa^2} \frac{N}{4} \quad (4.15b)$$

with $\kappa = knN$, being the signal to noise ratio (projection noise to shot noise). From eq. (4.15) it is clear that the noise in \hat{F}_z has been reduced with a corresponding increase in the complementary operator \hat{F}_x . Doing similar calculations, as above, where one do *not* condition on a specific detection result of \hat{S}_x one finds that the atomic ensemble is *not* squeezed [Hammerer et al. 2010]. In chapt. 8, we present the experimental realization of such a spin squeezed state.

4.2.2 Squeezing criteria

When quantifying and comparing experiments it is always important to be very clear in exactly which parameter is considered. In this section we introduce two ways of quantifying the amount of squeezing, we start with the most intuitive criteria.

Kitagawa and Ueda criteria

In the early nineties in a seminal paper by M. Kitagawa and M. Ueda [Kitagawa et al. 1993] the concept of spin squeezed states was introduced. The method of generating spin squeezed states where through a non-linear interaction. This would smear out the error disk of a coherent super position state, thus creating a noise reduction of a given observable. As it has been stated several times squeezing in a given observable is when the noise of that observable is reduced below the bound set by Heisenberg uncertainty relation after the measurement (or interaction), see eq. (2.11). The crucial point to note here is that a measurement might reduce the mean value of the observable in question, where we have introduced the decoherence parameter η . From Heisenberg uncertainty relation we thus obtain the following demand to claim spin squeezing

$$\text{var}(\hat{F}_z^{\text{out}}) < (1 - \eta) \text{var}(\hat{F}_z^{\text{in}}). \quad (4.16)$$

An important thing to note follows from the comment made at the end of sec. 2.3, where it was shown that the measurement precision will increase as the number of atoms is increased. It is thus clear that if one creates a squeezed state according to the Kitagawa and Ueda squeezing criterion it *does not* imply improved measurement precision.

Wineland's criteria

It is exactly the problem regarding the measurement precision that Wineland et al. [Wineland et al. 1994] overcomes with their more strict squeezing criterion.

For metrology applications the precision is set by the angular uncertainty, $\delta\alpha$, of the Bloch vector introduced in sec. 2.2.1 given by

$$\delta\alpha \approx \arcsin \left(\frac{\sqrt{\text{var}(\hat{F}_z)}}{|\langle \hat{F}_x \rangle|} \right), \quad (4.17)$$

and it is this parameter which will need to be reduced in order to obtain metrology relevant squeezing. We thus get

$$\frac{\sqrt{\text{var}(\hat{F}_z^{\text{out}})}}{|\langle \hat{F}_x^{\text{out}} \rangle|} < \frac{\sqrt{\text{var}(\hat{F}_z^{\text{in}})}}{|\langle \hat{F}_x^{\text{in}} \rangle|} \Leftrightarrow \quad (4.18a)$$

$$\text{var}(\hat{F}_z^{\text{out}}) < (1 - \eta)^2 \text{var}(\hat{F}_z^{\text{in}}), \quad (4.18b)$$

as the metrology relevant squeezing parameter. An important consequence of this squeezing criterion is that the spins must have non-classical correlations and are thus in an entangled state [Sørensen et al. 2001].

Atomic Fock states

In this chapter we present the theory of the atomic Fock states, in particular we focus on the state with a collective single excitation in the atomic ensemble. A method allowing for the generation of this highly non-classical (negative Wigner function) and non-Gaussian (entangled) state is presented. The ideas presented are in close analogy to methods used in photonic systems, where combinations of discrete excitation and measurements in the continuous variable basis are extensively used. The material presented here have recently been submitted to a focus issue of the New Journal of Physics on quantum tomography as well as the arXiv [Christensen et al. 2012].

5.1 Idealized generation method

We consider an atomic system of N_{at} spin-1/2 particles described by the states $|\uparrow\rangle$ and $|\downarrow\rangle$. Initially all atoms are prepared in the $|\uparrow\rangle$ state (fig. 5.1a), the quantum state of the ensemble can be written as the product state

$$|\Psi_0\rangle = \bigotimes_{j=1}^{N_{\text{at}}} |\uparrow\rangle \quad (5.1a)$$

$$= |\uparrow\uparrow \dots \uparrow\uparrow\rangle. \quad (5.1b)$$

A weak off-resonant excitation pulse is shined onto the ensemble. Conditioned on the detection of a single forward scattered Raman photon, a single spin flip occurs in the collective atomic state of the ensemble. This detection event heralds the preparation of a single excitation of a collective zero-transverse-momentum spin wave in the atomic ensemble (fig. 5.1b). The success probability of this forward scattering is kept low, so that the probability of two and more photons scattered forward is negligible sec. 5.2. The state of the ensemble [Duan et al. 2001] becomes

$$|\Psi_1\rangle = \hat{a}^\dagger |\Psi_0\rangle \quad (5.2a)$$

$$= \frac{1}{\sqrt{N_{\text{at}}}} \sum_{j=1}^{N_{\text{at}}} |\uparrow\uparrow \dots \uparrow\downarrow_j \uparrow \dots \uparrow\uparrow\rangle, \quad (5.2b)$$

where we have defined the collective creation operator

$$\hat{a}^\dagger \equiv \frac{1}{\sqrt{N_{\text{at}}}} \sum_{j=1}^{N_{\text{at}}} (|\downarrow\rangle \langle \uparrow|)_j. \quad (5.3)$$

A subsequent microwave $\pi/2$ -pulse rotates this collective entangled state (fig. 5.1c) so that it becomes a superposition of $|\uparrow\rangle$ and $|\downarrow\rangle$ with a non-Gaussian population

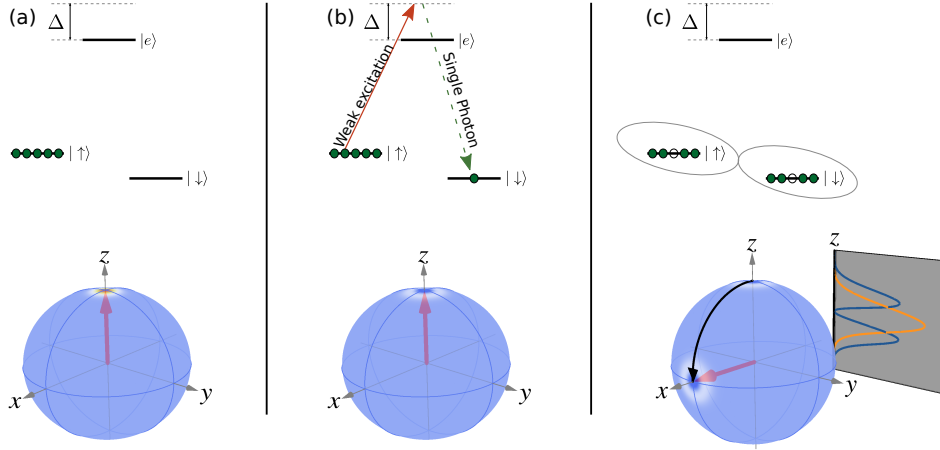


Figure 5.1: The atomic levels and Bloch spheres at different stages of the implementation (a) Preparing all atoms in $|\Psi_0\rangle$ and shine a weak blue detuned excitation pulse (b) detection of a forward scattered Raman photon signals the generation of a collective excitation in the ensemble (c) a microwave $\pi/2$ rotation rotates the state $|\Psi_1\rangle$ into the equatorial plane of the Bloch sphere, the insert shows a plot of the clearly non-Gaussian (Gaussian) marginal distribution of the $|\Psi_1\rangle$ ($|\Psi'_0\rangle$) state after a rotation to the equatorial plane in blue (orange).

difference between the two hyperfine levels. From this it is clear that *conditioned* on whether a single photon is detected or not the marginal distributions will be profoundly different, see insert on fig. 5.1c.

In the ideal case of perfect tomography of a pure single excitation state the population difference should be a marginal distribution of a Wigner function with a single excitation, a $n = 1$ Fock state as shown above. In a realistic case of finite efficiency of both the state preparation and the tomography we show that the marginal distribution still retain its non-Gaussian and non-classical features, as discussed in detail, see sec. 9.1. We now consider the probability of creating excitations in the atomic ensemble together with the relevant marginal distributions.

5.2 Properties

In this section we will expand on some of the properties of the single excitation state described above, and show that the created state has a non-Gaussian marginal distribution and a negative Wigner function, allowing us to classify the state as non-classical. Due to the analogy for photonic systems, what is presented in this section might look familiar to the reader. We start by considering the n 'th excited state is given as

$$|\Psi_n\rangle = \left[\binom{N_{\text{at}}}{n} \right]^{-1/2} \sum_{\text{Total of } n \text{ atoms down}} |\uparrow\uparrow \dots \uparrow\downarrow \dots \uparrow\downarrow \dots \uparrow\rangle \quad (5.4)$$

where the sum is over *all* possible permutations and we have introduced the standard binomial coefficient. We start by considering the action of working with

the creation operator on the general n 'th excited state

$$\hat{a}^\dagger |\Psi_n\rangle = \frac{1}{\sqrt{N_{\text{at}}}} \sum_{j=1}^{N_{\text{at}}} (|\downarrow\rangle\langle\uparrow|)_j \left[\binom{N_{\text{at}}}{n} \right]^{-1/2} \sum_{\text{Total of } n \text{ atoms down}} |\uparrow\uparrow \dots \uparrow\downarrow \dots \uparrow\downarrow \dots \uparrow\rangle \quad (5.5a)$$

$$= (n+1) \left[N_{\text{at}} \cdot \binom{N_{\text{at}}}{n} \right]^{-1/2} \sum_{\text{Total of } n+1 \text{ atoms down}} |\uparrow\uparrow \dots \uparrow\downarrow \dots \uparrow\downarrow \dots \uparrow\rangle \quad (5.5b)$$

$$= (n+1) \left[\frac{\binom{N_{\text{at}}}{n+1}}{N \cdot \binom{N_{\text{at}}}{n}} \right]^{1/2} |n+1\rangle \quad (5.5c)$$

$$= (n+1) \left[\frac{N-n}{N(n+1)} \right]^{1/2} |n+1\rangle \quad (5.5d)$$

$$\approx \sqrt{n+1} |n+1\rangle, \quad (5.5e)$$

where the last approximation holds for $N_{\text{at}} \gg n$ and we see the clear similarity to eq. (3.3a).

After the detection of the single photon, which heralds the creation of the single excitation, we rotate the state in to the equatorial plane by a microwave $\pi/2$ pulse. To describe this we introduce the operator $\mathbf{M}_{\mu W}^{\pi/2}$ which rotates *each* atom according to

$$|\rightarrow\rangle \equiv \mathbf{M}_{\mu W}^{\pi/2} |\downarrow\rangle = \frac{1}{\sqrt{2}} (|\downarrow\rangle + |\uparrow\rangle), \quad (5.6a)$$

$$|\leftarrow\rangle \equiv \mathbf{M}_{\mu W}^{\pi/2} |\uparrow\rangle = \frac{1}{\sqrt{2}} (|\downarrow\rangle - |\uparrow\rangle). \quad (5.6b)$$

The total ensemble state becomes

$$|\Psi'_n\rangle = \mathbf{M}_{\mu W}^{\pi/2} |\Psi_n\rangle. \quad (5.7)$$

In the experiment we will be measuring the marginal distribution of \hat{F}_z which is the population difference in the ensemble. To show that the created state has a non-Gaussian marginal distribution we calculate the probability to detect n atoms in the $|\downarrow\rangle$ state given we are in the state $|\Psi'_1\rangle$ (the overlap between $|\Psi_n\rangle$ and $|\Psi'_1\rangle$)

$$P(n|\Psi'_1) = |\langle\Psi_n|\Psi'_1\rangle|^2 \quad (5.8a)$$

$$= \left[\binom{N_{\text{at}}}{n} \right]^{-1/2} \left| \sum_{\text{Total of } n \text{ atoms down}} \langle\uparrow\uparrow \dots \uparrow\downarrow \dots \uparrow\downarrow \dots \uparrow| \leftarrow\leftarrow \dots \leftarrow\rightarrow\leftarrow \dots \leftarrow\rangle \right|^2 \quad (5.8b)$$

$$= \left[\binom{N_{\text{at}}}{n} \right]^{-1/2} \left| \sum \left[(\langle\uparrow|\leftarrow\rangle)^{N_{\text{at}}-n} \cdot \langle\downarrow|\leftarrow\rangle^{n-1} \cdot \langle\downarrow|\rightarrow\rangle \right] n \right. \quad (5.8c)$$

$$\left. + \left[(\langle\uparrow|\leftarrow\rangle)^{N_{\text{at}}-n-1} \cdot \langle\uparrow|\rightarrow\rangle \cdot \langle\downarrow|\leftarrow\rangle^n \right] (N_{\text{at}} - n) \right|^2 \quad (5.8d)$$

$$= \left(\frac{1}{2} \right)^{N_{\text{at}}} \binom{N_{\text{at}}}{n} \frac{4}{N_{\text{at}}} \left(n - \frac{N_{\text{at}}}{2} \right)^2. \quad (5.8e)$$

A similar calculation assuming we are in the $|\Psi'_0\rangle$ state yields

$$P(n|\Psi'_0) = |\langle\Psi_n|\Psi'_0\rangle|^2 \quad (5.9a)$$

$$= \left(\frac{1}{2} \right)^{N_{\text{at}}} \binom{N_{\text{at}}}{n}. \quad (5.9b)$$

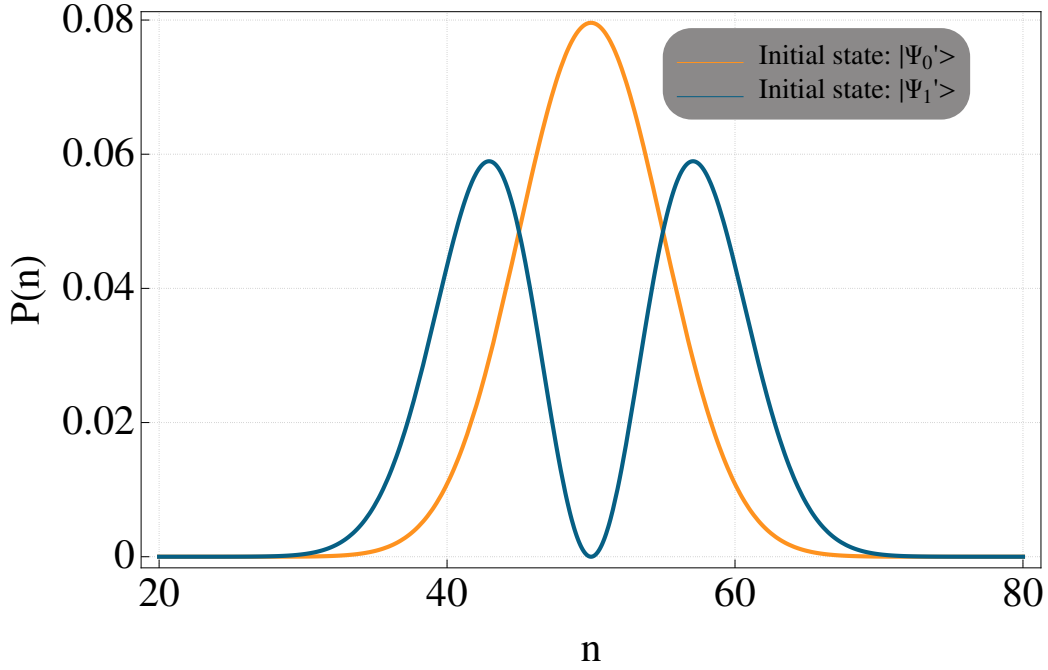


Figure 5.2: Probability to detect n atoms in the state $|\downarrow\rangle$ given the initial state of the ensemble as $|\Psi_0\rangle$ orange and $|\Psi_1\rangle$ blue.

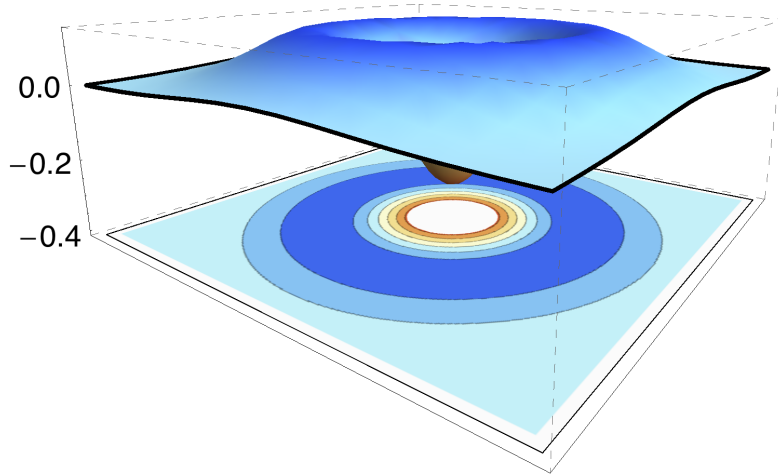


Figure 5.3: Plot of the Wigner function for the state $|\Psi_1\rangle$ with a corresponding contour plot. We clearly see that the Wigner function takes negative values, showing that the state is non-classical.

In fig. 5.2 we have plotted the probability of detecting n atoms being in the $|\downarrow\rangle$ state given we have $N_{\text{at}} = 100$, taking either $|\Psi_0\rangle$ or $|\Psi_1\rangle$. This is the marginal distributions of the state¹

From the marginal distributions we can calculate the Wigner functions which is shown in fig. 5.3. We see that the Wigner function clearly has negativities, this allow us to characterize the state as being non-classical Kot et al. 2012. We here note that there are several criteria for non-classicality and that a negative Wigner function is one of the strongest. Having now introduced the main theoretical framework used in this report we are now entering the experimental part.

¹For large N_{at} be approximated by the square modulus of the standard harmonic oscillator wave functions.

Part II
Experiment

Overview of setup

In this chapter we introduce the experimental apparatus. First we have the trapping of atoms in a magneto optical trap (MOT) from which they are transferred into a far off-resonant dipole trap (FORT). After this we combine optical pumping, microwave pulses and purification pulses to prepare a pure state of the atomic ensemble. In this way an ensemble with $\approx 10^5$ atoms where more than 97% of the atoms are in the same state is produced. At this point we are ready to create the quantum state of interest. This is usually done by microwave pulses, and for the collective single excitation state the detection of a single photon is needed. This is followed by the implementation of our QND probing method which allows us to characterize the quantum state of the atomic ensemble. As the last part we have the data acquisition which is done by an oscilloscope producing raw data files which are then passed on to us for further analysis. To get the show on the road we start by considering the trapping of atoms.

6.1 Atom trapping and cooling

As stated in chapt. 2, there is a huge toolbox of well developed techniques to interface and manipulate atomic ensembles. This means that most of the methods discussed in this section are neither exotic or special. Since we are dealing with standard techniques and no major change of the experimental setup has been done since [Oblak 2010; Windpassinger 2008] I will skip certain parts and try to focus on the key aspects, neglecting the more technical side.

The atoms are situated in a glass cell produced by Starna with outer dimensions of $120 \times 48 \times 48 \text{ mm}^3$. The glass cell is anti reflection coated¹ on the outside and is connected to a vacuum chamber with a pressure of around 10^{-9} mbar, which is maintained by a Varian Starcell ion pump². To obtain the needed vapour pressure of Cs in the cell we have connected four SAES getter sources (dispensers). Since the work of [Oblak 2010; Windpassinger 2008] the vacuum has been broken³ and we used this opportunity to exchange the getter sources.

¹The cell has been around for a long time, and we fear that the high powers used for the dipole trap might have burned the anti-reflection coating at some positions of the cell. This was felt first hand when we during late 2011 had a huge amount of extra noise in our apparatus. After around two months of investigation the solution where to move the cell around 5 mm.

²We do not have a pressure gauge connected permanently since all we are interested in is for the pressure to be low enough to create a MOT.

³Due to a power failure in the lab.

6.1.1 Magneto optical trap

As with all other cold atom experiments, the initial stages of atom trapping is based on a MOT. We use a standard six laser beam configuration, together with a set of anti-Helmholtz coils⁴ to produce the required magnetic field gradient. Three coil pairs are used to compensate static magnetic background fields. The complete optical setup used for the MOT is shown in fig. 12.2. Each MOT beam is coupled into a fiber, its output goes to custom beam expanders giving beams with a diameter of ≈ 30 mm. In each MOT beam we have around 4 mW of cooling light ($F = 4 \rightarrow F' = 5$ transition) mixed with 2 mW of repump light ($F = 3 \rightarrow F' = 4$ transition). The MOT light comes from two homebuilt external cavity diode lasers (ECDL), in the Littrow configuration. Each laser uses a 100 mW diode from Axcel photonics⁵ running with an output of about 20 mW, after the external cavity. The cooler (repumper) is locked via Doppler free absorption spectroscopy to the $F = 4 \rightarrow F' = 3 \times 4$ ($F = 4 \rightarrow F' = 2 \times 3$) crossover transition. The error signal, required for locking, is generated via a Pound-Drever-Hall like method where sidebands are generated by a 20 MHz (4 MHz) modulation of the laser diode current. The laser linewidth has previously been measured to be 500 kHz over a few seconds [Windpassinger 2008]. To be able to sweep the light frequency around the resonance we send both lasers through individual double pass acoustic optical modulator (AOM) setups. The needed output power is obtained by using two slave laser⁶ with an output of 100 mW. Each slave is frequency stabilized via injection locking to its corresponding master laser. The slave outputs is sent through a single pass AOM for fast on and off switching and power control. To prevent any light leaking through the AOMs a mechanical shutter is placed in each beam. The cooler and repumper are overlapped on a polarizing beam splitter (PBS) and are then split in to six separate beams that are coupled into individual fibers. The magnetic coils, AOMs and shutters are all connected to National Instruments analogue output cards allowing us to computer control it all. This is done via the CAMOT (Carlos MOT Controller) LabView program which due to a computer breakdown and following update to Windows 7 has gone through a complete redesign since the work of [Oblak 2010; Windpassinger 2008].

MOT loading

The experimental sequence starts by loading the atoms from the background vapour pressure into a MOT. The cooler and repumper are detuned $\approx -2\Gamma$ from their respective transitions together with a magnetic field gradient of around 12 Gauss/cm. In this configuration we load atoms for around 2000 ms. Afterwards we enter a phase of sub-Doppler cooling lasting approximately 200 ms. This is done by ramping up the detuning of both the cooler and repumper while turning down the repump power. During this the dipole trap is on, and when the sub-Doppler cooling is done we turn off the MOT beams and are left with an elongated atomic cloud trapped in the FORT. All the above numbers are ball park estimates, and are optimized on a daily basis in the experiment, with the goal of seeing as many atoms in the dipole trap as possible.

⁴The coils have a radius of 11.5 cm and have 41 windings.

⁵Type number: M9-852-0100-S30.

⁶We use diodes from Eagleyard.

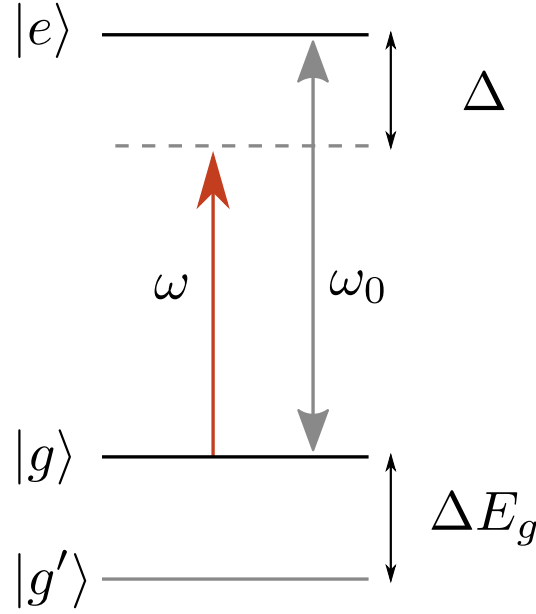


Figure 6.1: A two level atom with the states $|g\rangle$ and $|e\rangle$ interacting with an electromagnetic field at frequency ω . Due to the interaction with the electro-magnetic field the atomic levels experience an intensity dependent AC-Stark shift. Due to the transverse intensity profile of the laser we now have a position dependent trapping potential.

6.1.2 Dipole trap

The theory and operation of dipole traps⁷ for neutral atoms have over the last decades been developed into textbook knowledge [Grimm et al. 1999]. We consider a two level atom, with energy eigenstates $|g\rangle$ and $|e\rangle$ and a transition frequency of ω_0 , interacting with an electro-magnetic field

$$\mathbf{E}(\mathbf{r}) = \varepsilon E_0(\mathbf{r}) e^{i\omega t} \quad (6.1)$$

at a position \mathbf{r} and with a polarization ε . Denoting the Rabi frequency by Ω the interaction Hamiltonian is given by

$$\hat{\mathcal{H}}_{\text{int}} = \hbar \left[\omega_0 |e\rangle \langle e| + \omega_0 \hat{a}^\dagger \hat{a} + \Omega \left(|e\rangle \langle g| \hat{a} e^{i\Delta t} + |g\rangle \langle e| \hat{a}^\dagger e^{-i\Delta t} \right) \right], \quad (6.2)$$

where the zero point energy is chosen such that $E_g = 0$. Writing this in matrix form and diagonalizing it, we find energy eigenvalues for the combined light-atom system. Taking the laser to be detuned by Δ from resonance, see fig. 6.1, the light gives rise to a level shift of the ground states of

$$\Delta E_g = \frac{\hbar \Omega^2}{\Delta}. \quad (6.3)$$

This shift is known as the AC-Stark shift, and has been calculated under the assumption that $\Delta \gg \Omega$. The Rabi frequency is proportional to the electromagnetic field and given as

$$\Omega \equiv \frac{-e E_0(\mathbf{r}) |\langle e | \varepsilon \cdot \mathbf{x} | g \rangle|}{\hbar}. \quad (6.4)$$

The energy shift is proportional to the electric-field intensity (Ω^2) and inverse proportional to the detuning (Δ). Depending on the sign of the detuning (negative

⁷Also known as optical tweezers, if you are doing biophysics.

for red detuned light and positive for blue detuned) the ground states energy is shifted down (red detuned) or up (blue detuned). Since the transverse intensity profile of a laser beam is Gaussian it is clear that the energy shift will be position dependent. Taking the laser to be red detuned we will form a trapping potential with a spatial profile corresponding to the intensity profile of the laser.

To formalise this we consider the intensity of the electro-magnetic field,

$$I(\mathbf{r}) = \frac{1}{2} \epsilon c E(\mathbf{r})^2, \quad (6.5)$$

from this and the dipole matrix element [Grimm et al. 1999], we find a trapping potential given by

$$U(\mathbf{r}) = \frac{3\pi c^2 \Gamma}{2\omega_0^3 \Delta} I(\mathbf{r}). \quad (6.6)$$

Both the D1 and D2 lines play a role, and we thus need to sum the two resulting potentials

$$U(\mathbf{r}) = \frac{\pi c^2}{2} \left(2 \frac{\Gamma_{D2}}{\omega_{0,D2}^3 \Delta_{D2}} + \frac{\Gamma_{D1}}{\omega_{0,D1}^3 \Delta_{D1}} \right) I(\mathbf{r}), \quad (6.7)$$

where we have weighted the D1 and D2 lines according to their respective transition strengths. Finally we use the transverse Gaussian intensity profile of a laser beam propagating in the z -direction and find

$$U(\mathbf{r}) = U_0 \frac{w_0^2}{w(z)^2} \exp\left(-\frac{2r^2}{w(z)^2}\right), \quad (6.8)$$

where w_0 is the spot size of the beam and $w(z)$ describes the beam waist along the propagation direction. The trap minima is given by

$$U_0 = \frac{c^2}{w_0^2} P \left(2 \frac{\Gamma_{D2}}{\omega_{0,D2}^3 \Delta_{D2}} + \frac{\Gamma_{D1}}{\omega_{0,D1}^3 \Delta_{D1}} \right), \quad (6.9)$$

where P is the laser power, which is directly measurable.

Since the work of [Oblak 2010; Windpassinger 2008] a new laser is used for the dipole trap⁸. This is a EM4 laser diode⁹ with a wavelength of 1064 nm and an output of up to 250 mW. This is sent to a Nufern fiber amplifier¹⁰ which has a output power of up to 10 W. After passing through an AOM used for switching purpose we focus the beam down to a waist of $\approx 50 \mu\text{m}$ via a $f = 100 \text{ mm}$ achromatic lens. To overlap it with the probe arm of the MZI we use two dichroic mirrors, see fig. 6.2. The power monitoring is done after the second dichroic mirror, where powers in the range of 3 – 5 W are observed depending on the amplifier setting. Assuming a power in the dipole trap of 5 W we find a trapping minimum of $280 \mu\text{K}$.

6.2 MZI setup

To measure the state dependent atomic phase shift, described in chapt. 4, we use a MZI. This allows us to measure the relative phase between a probe mode and a reference mode, as described in sec. 3.3. In this section we consider the interferometric setup together with the layout of the two probe lasers and the effect

⁸The reason for this was a strange mode behaviour of the old Versadisk laser [Oblak 2010, sec. 9.1.2]

⁹Part number: EM509.

¹⁰Part number: PSFA-1064-50-10W

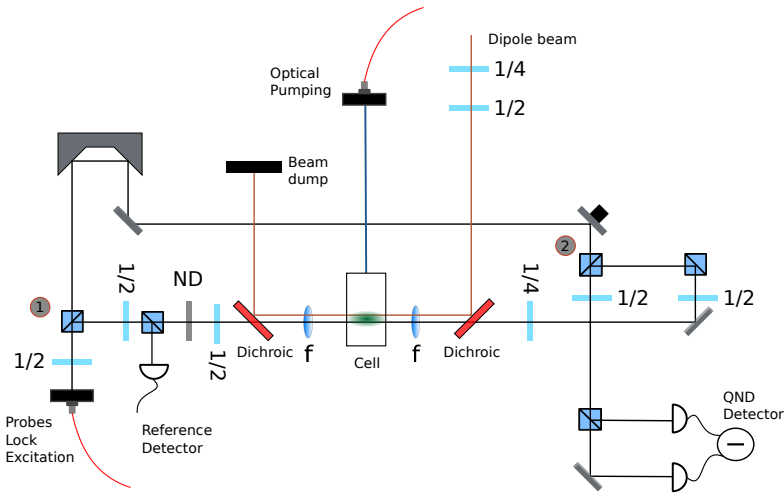


Figure 6.2: The optical setup of the MZI used for the measurements of squeezing.

on some classical noise sources on the setup. In fig. 6.2 the full interferometric setup is shown. All beams (the two probes and the interferometer lock laser) arrive to the MZI via the same single mode optical fiber giving a near perfect mode matching of the beams. After the fiber, the beam is split into a probe and a reference (local oscillator), this is done with a PBS (marked 1 on fig. 6.2). We start by considering the path of the probe mode. First we split off light for a power reference measurement via a PBS. We then attenuate the probe beam via an absorbing neutral density filter. The beam now passes through a $\lambda/2$ zero order waveplate allowing us to set its polarization. The setting of this waveplate depends on which kind of experiment we want to perform. For a squeezing measurement we use π polarized light. Afterwards the beam is focused down to a spot size of $\approx 30\mu\text{m}$. To obtain the highest spatial overlap of the probe beam with the trapping beam, the same achromatic lens pair is used. The focused beam now passes through the atomic sample, and is afterwards collimated by an achromatic lens identical to the first. After this the beam is sent towards a PBS (marked 2 on fig. 6.2) where it gets overlapped with the reference arm. We now consider the reference beam, which gets transmitted through the first PBS. After this it goes to a cat-eye mirror used to change the path length difference between the two interferometer arms. After the cat-eye we use a piezo mounted mirror to guide the beam onto the overlapping PBS. The piezo mirror is used for several purposes, first in initial calibration and optimization of the interferometer visibility. Secondly it is used during the experimental run to compensate long term drifts. The now overlapped probe and reference beams pass through a $\lambda/2$ waveplate, before it gets split by a PBS and is detected using a homebuilt shot noise limited difference detector [Windpassinger 2008; Windpassinger et al. 2009], termed the QND detector.

Here it is important to note two things, first the described detection of the probe light is essentially a balanced homodyne detection [Leonhardt 1997], where the weak probe (recall we attenuate the probe by a ND filter) is mixed with a strong classical field (local oscillator). Secondly we estimate the effect of the mismatch between the waist of the probe and the trapping laser. Since $w_{0,\text{trap}} > w_{0,\text{probe}}$, atoms will always fill the whole probe volume, but they might move in and out of this volume. The main problem with this is that two successive QND measurements will not be perfectly correlated. This is since in the time between the two measurements some atoms might have moved out and others into the probe volume. The good news is that this effect is estimated to be rather small since we have transverse trap frequencies on the order of 1 kHz whereas the

probing frequency is tens of kHz, meaning that this effect will not be profound.

6.2.1 Probe setup

To probe the atomic ensemble we use two ECDL¹¹, each probing atoms in either the $|3\rangle$ (purple) or $|4\rangle$ (orange) state. The probe layout has not changed since the work of [Oblak 2010; Windpassinger 2008], and we will only briefly outline it here, a full setup drawing can be seen in fig. 12.1. The locking is based on a digital phase lock [Appel et al. 2009b], operating in the following way: The beat-note between two lasers is measured and stabilized to an external reference frequency, by controlling the laser current and piezo position. By setting the external reference frequency we can now tune the laser frequency as desired. The purple probe is locked to the MOT repumper and the orange probe to the purple probe. Each probe goes through a single pass AOM used to pulse the probes. To get power control and stability both probes go through a motorized waveplate and a PBS before they are overlapped. By turning the waveplates we can thus keep the power ratio of the two probes constant. To control the pulsing of the probe lasers we use a DIO64 from Viewpoint systems with 64 digital outputs and a timing resolution of 50 ns. The output of this card controls all parts of the experiment with high requirements for timing, like the probe pulses. The DIO64 card is interfaced via a separate LabView program synchronised to the CAMOT program.

The dual-colour probing method used was proposed in [Saffman et al. 2009; Louchet-Chauvet et al. 2010] and gives us several advantages. First and most importantly it gives a large reduction of the acoustic noise, as described in sec. 6.2.2, allowing us to reach projection noise limited sensitivity. Secondly it allows us to tune the AC-Stark shift of each clock-level individually, by changing the detuning of the relevant probe laser. In this way we can to first order cancel the differential AC-Stark shift between the clock-levels.

6.2.2 Noise scaling

In this section we consider how different classical noise sources affect the detected signal, given by the photo current output, $i_-(t)$, of the QND detector. This discussion will be useful for several reasons, first it allows us to choose parameters of the MZI such that we become as insensitive to external noise sources as possible. Furthermore we will use the knowledge gained to perform a noise scaling analysis on the obtained data which allows us to distinguish between different noise sources. The discussion will closely follow [Oblak 2010, chapt. 6].

The photo current output from the QND detector is given as

$$i_-(t) = \langle i_- \rangle + \delta i_-(t), \quad (6.10)$$

and mainly we will be interested in the fluctuations $\delta i_-(t)$ with $\langle \delta i_-(t) \rangle = 0$. It is often the case that we have knowledge about the spectrum of a given noise source, to use this it is favourable to make a Fourier decomposition of the fluctuating term, which combined with Parseval's identity allows us to write the variance of the photo current output as [Oblak 2010, eq. (6.3)]

$$\text{var}(i_-(t)) = \int_{-\infty}^{\infty} |g(\omega)|^2 W_i(\omega) d\omega. \quad (6.11)$$

Here $g(\omega)$ characterizes the detector bandwidth and choice of mode function and $W_i(\omega)$ is the spectral power density. We start by considering the explicit

¹¹In our laboratory a laser gets referred to by its colour and we call the two probes orange and purple.

expression for the *classical* part of the photo current output, which we will not derive here but instead refer to [Oblak 2010, eq. (6.5)]

$$i_- = k \cos(\tilde{\phi}) \frac{N_{\text{ph}}}{t_p}, \quad (6.12)$$

where t_p is the pulse duration, $\tilde{\phi}$ is the relative phase between the two MZI arms and k describes losses through the MZI¹². In the following we consider some of the central classical noise sources, starting with the frequency fluctuations.

Frequency noise

The frequency noise of the laser will be converted to fluctuations of the relative phase between the two modes of the MZI. To model this we assume, for now, that the optical path length difference Δl does not fluctuate allowing us to write

$$\delta\tilde{\phi} = \delta\omega \frac{\Delta l}{c}, \quad (6.13)$$

Using this in eq. (6.12) gives

$$i_- = k \cos\left(\tilde{\phi} + \delta\omega \frac{\Delta l}{c}\right) \frac{N_{\text{ph}}}{t_p}. \quad (6.14)$$

Assuming that $\delta\omega \Delta l / c \ll 1$ and doing a Taylor expansion of the cosine to first order

$$\cos\left(\tilde{\phi} + \delta\omega \frac{\Delta l}{c}\right) \approx \cos(\tilde{\phi}) - \frac{\delta\omega \Delta l}{c} \sin(\tilde{\phi}). \quad (6.15)$$

This can be inserted directly into eq. (6.11) yielding

$$\text{var}(i_-)_{\text{Freq}} = \left[k \frac{\Delta l}{c} \sin(\tilde{\phi}) \frac{N_{\text{ph}}}{t_p} \right]^2 \int_{-\infty}^{\infty} |g(\omega)|^2 W_i(\omega) d\omega. \quad (6.16)$$

The first thing we note is the *quadratic scaling* with photon number, which is a clear signature of classical noise. We also see that if $\tilde{\phi} = n\pi$ the fluctuations will not be present in our signal¹³. In order to become as insensitive as possible we will choose Δl as small as possible, which means that we want to be as close to the white light position as possible. The reason for not setting $\Delta l = 0$ will become clear in a bit, when we consider the acoustic noise.

Intensity noise

We consider the intensity fluctuations of the laser which will manifest itself as

$$\text{var}(i_-)_{\text{Int}} = \left[k \cos(\tilde{\phi}) \frac{N_{\text{ph}}}{t_p} \right]^2 \int_{-\infty}^{\infty} |g(\omega)|^2 W_i(\omega) d\omega. \quad (6.17)$$

First we see the quadratic scaling with N_{ph} , allowing for the distinguishing between quantum and classical noise. The central thing is the dependence on $\cos^2(\tilde{\phi})$. By setting $\tilde{\phi} = \pi(n + \frac{1}{2})$ we will become insensitive to intensity fluctuations.

Acoustic noise

The term acoustic noise is used for anything that makes fluctuations of the path length difference between the MZI arms. This can be mirror vibrations, people

¹²Absorption, transmissions and non-perfect mode overlap, gain, quantum efficiency of the detector and power used in the reference arm.

¹³In the experiment we will use $\tilde{\phi} = n\pi + \frac{1}{2}$ since this allows us to cancel intensity noise of the probe lasers, but (sadly) makes us maximally sensitive to frequency noise.

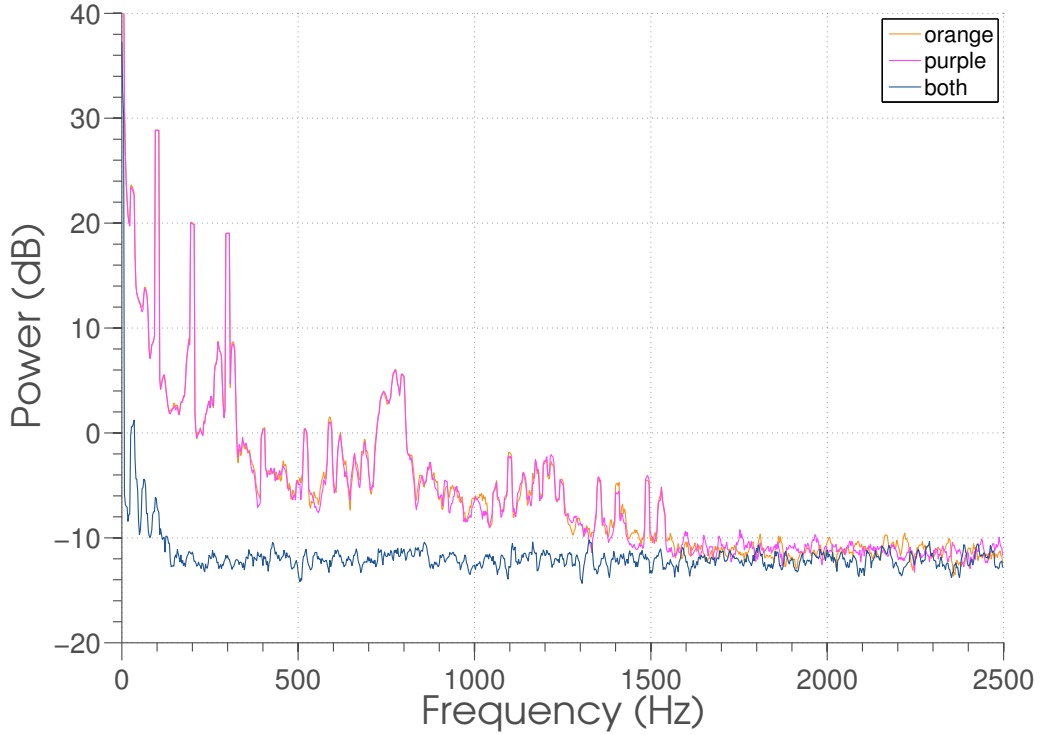


Figure 6.3: Noise spectrum of the empty MZI, with single and dual colour probing methods. Note the substantial noise reduction obtained by using the dual colour method, in which common mode noise of the lasers are cancelled out.

walking in the lab and so forth. Due to the many different sources the acoustic noise is hard to track down, and might be considered the biggest enemy of the experiment. Doing a similar analysis, as for the frequency noise now with fixed ω and fluctuating Δl , we find that the output of the QND detector fluctuates as

$$\text{var}(i_-)_{\text{Acco}} = \left[k\omega \sin(\tilde{\phi}) \frac{N_{\text{ph}}}{t_p} \right]^2 \int_{-\infty}^{\infty} |g(\omega)|^2 W_i(\omega) d\omega, \quad (6.18)$$

we again find a quadratic scaling with the photon number. But this time we do not find any direct way to suppress the noise. The way out of this comes by using our dual-colour probing method. By using two probes (each measuring the atom number in one of the clock levels) of equal powers that are out of phase with one another¹⁴. Since the two probes are out of phase with each-other we will be measuring their *difference* at the MZI output. The acoustic fluctuations which are common mode (affecting both lasers the same way) will thus cancel out. We have measured the interferometer noise power spectrum, shown in fig. 6.3, using either a single (orange or purple) probe or the dual colour probing described. For the whole frequency range up to 1.5 kHz a clear noise reduction of 10 – 30 dB, is seen.

6.2.3 Locking the MZI path length

To reach the required stabilities of the apparatus, i.e. projection noise limited sensitivity, the path-length difference of the MZI is actively stabilized via a feedback to the piezo. This is done with a ECDL with $\lambda = 830 \text{ nm}$, which is far detuned from any atomic transition, and the thus do not interact with the

¹⁴The relative phase of the two probes can be tuned via the path length difference Δl , and it is exactly this requirement that does not allow us to choose $\Delta l = 0$ in order to suppress the frequency fluctuations of the lasers.

atoms. The laser is on/off modulated with a frequency of 100 kHz via an AOM. To ensure that the locking laser and probe lasers trace out identical optical paths in the MZI they are coupled into the same fiber, see sec. 6.2.1. To obtain an error signal we directly use the demodulated interference output of the QND detector. This is sent to a PI that generates the corresponding feedback for the piezo. In order to make sure that the lock pulses do *not* affect the phase shift measurement we switch off the lock laser around the series of probe pulses.

6.3 Microwave

In this section we consider the coherent interaction between the atomic ensemble and the electro-magnetic field from our microwave source, with a Rabi frequency χ . The interaction Hamiltonian between a magnetic field $\hat{\mathbf{B}}(t) = \hat{\mathbf{B}}_0 e^{-i\omega t}$, and a two level atom with magnetic moment $\hat{\boldsymbol{\mu}}$ is

$$\hat{\mathcal{H}}_{\text{int}} = -\hat{\boldsymbol{\mu}} \cdot \hat{\mathbf{B}}. \quad (6.19)$$

Our microwave source has an output in the order of 10 W and a frequency of 9 GHz and we can thus neglect its quantum properties, and substitute all operators with their classical expectation values. By applying a magnetic bias field with a magnitude around 1 Gauss along the z -axis (vertical direction) the interaction becomes $-\mu_0 B_0$, which assumes that only $\Delta m_F = 0$ transitions will occur¹⁵. In the rotating wave approximation¹⁶ the evolution of the Bloch vector, \mathbf{F} , can be described by [Milonni et al. 2010]

$$\frac{d}{dt} \mathbf{F} = \mathbf{F} \times \boldsymbol{\Omega}, \quad (6.20)$$

where

$$\boldsymbol{\Omega} \equiv \begin{pmatrix} \text{Re}(\chi) \\ \text{Im}(\chi) \\ \Delta_0 \end{pmatrix}. \quad (6.21)$$

We note that, if the microwave is turned off, the Bloch vector will perform a constant rotation around the z axis¹⁷ with a frequency given by the generalized Rabi frequency

$$\Omega = |\boldsymbol{\Omega}| = \sqrt{\Delta_0^2 + |\chi|^2}, \quad (6.22)$$

where Δ_0 is the detuning from resonance. Secondly by choosing appropriate pulse durations it is clear from eq. (6.20) that we can perform arbitrary rotations of the Bloch vector. In our experiment we make extensive use of the microwave pulses both in the state preparation, see sec. 7.1, and to perform echo sequences as used in sec. 9.2.

The microwave source is homebuild and a detailed description is given in [Oblak 2010, p. 10.2.2]. It is based on an oven controlled 500 MHz quartz oscillator locked to a stable 10 MHz reference frequency from a GPS to allow for absolute frequency stability. The 500 MHz output gets mixed to 9 GHz, putting us in the range of the atomic transition. This signal is then mixed with a 192 MHz output from a DDS, meaning that the upper sideband will be resonant with the atomic transition. The signal passes through a filter cavity to make sure that the lower side band does not reach the atoms and is then amplified to give an output of approximately 10 W. The DDS is very flexible with a minimum frequency step

¹⁵Corresponding to a π polarization of the microwave output.

¹⁶Average out fast ($\approx 2\omega$) oscillating terms, by introducing slowly varying operators.

¹⁷This is exactly what is used in Ramsey spectroscopy, see sec. 7.2

of ≈ 0.2 Hz over large range which together with a variable phase makes it very versatile. This combined with the low phase noise -125 dB with respect to the carrier [Oblak 2010] gives us a very good experimental control over the microwave pulses.

Calibrations and optimizations

In all experiments, a lot of time is spent on calibrations and initial preparations before the central part of the experiment starts, our case is no exception. Some calibrations and optimizations are done on a daily basis and others are done in a more infrequent manner. In this chapter we will start by describing our state preparation method, afterwards we consider the calibration of the microwave pulses and at the end we describe the calibration of the magnetic fields.

7.1 State preparation

In this section we will describe our initial state preparation, with the goal of preparing the ensemble as pure as possible. This is done by applying a sequence of optical pumping pulses, microwave pulses and optical purification pulses, the whole process is outlined in fig. 7.1. This part of the experiment is delicate and has caused a few problems during my time. The reason for this is that our probing method is sensitive to the whole $F = 3, 4$ manifolds [Oblak 2010]. Whereas the microwave *only* interacts with a specific hyperfine transition. To

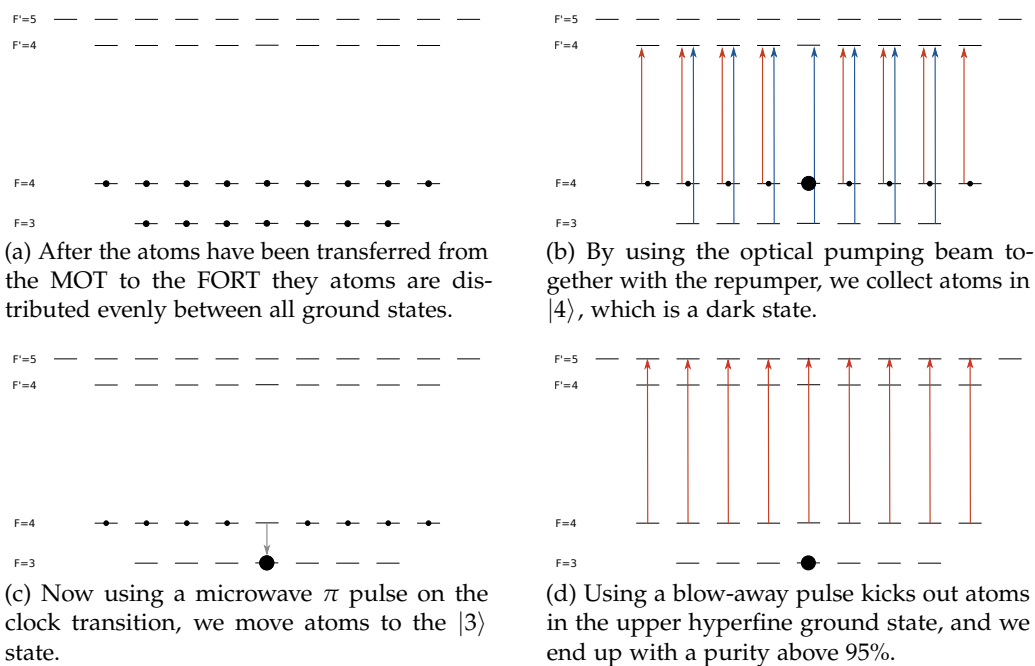


Figure 7.1: The applied sequence for the initial state preparation, figure inspired by J. Appel.

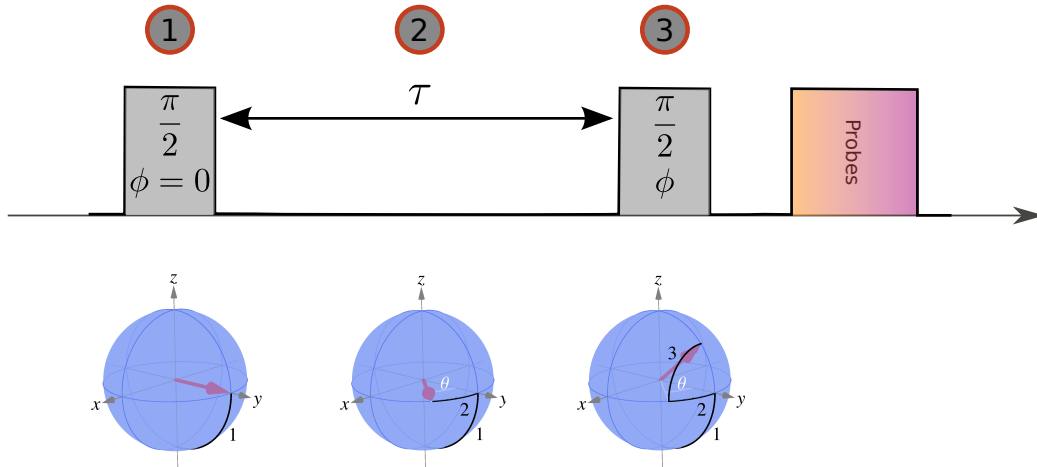


Figure 7.2: The Ramsey pulsing sequence shown together with the evolution of the Bloch vector.

illustrate this consider that after our state preparation we are left with 5% of the atoms in states with $m_F \neq 0$. Now doing a $\pi/2$ pulse to create a coherent spin state we will only address 95% of the atoms in the ensemble. The remaining atoms will still be measured by our probing, and will thus perturb the result. If the remaining fraction of atoms and their distribution in the hyperfine manifolds where constant we could take this into account in the data analysis, but as with everything else it will fluctuate from run to run, and thus add noise in form of a fluctuating atom number.

To perform the optical pumping we use a separate beam, coming from the MOT cooler slave¹. Via a double pass AOM it is shifted down such that it is on the $F = 4 \rightarrow F' = 4$ transition and afterwards coupled into a single mode fiber, see fig. 12.1. At the fiber output the beam is expanded and hits the atomic cloud orthogonal to the elongated axis, see fig. 6.2. After the atoms have been transferred to the dipole trap they will be evenly distributed among the hyperfine levels. Using an optical pumping pulse (duration around $1500\mu\text{s}$), together with repumper light allows us to pump atoms into the $|4\rangle$ state. Now both the optical pumping and repump laser are turned off, and we use the microwave to only address the atoms in the $|4\rangle$ state. By performing a π -pulse we transfer atoms from $|4\rangle$ to $|3\rangle$, *without* addressing other hyperfine transitions. We now *only* use the MOT cooler beam going along the gravitational axis to kick out the atoms which are in the $F = 4$ state. This part of the optical setup has changed since [Oblak 2010; Windpassinger 2008]. Previously all six MOT beams were used and the atoms were removed from the trap by heating. Whereas we now try to give each atom "kicks" along the weakest trap direction. This has given an improvement of a few percent in the purity of the ensemble. Using this method we can transfer around 70% of the initial number of atoms into the clock states, with only a few percent in other hyperfine levels.

7.2 Microwave calibrations

As it has become clear from the previous section we are making extensive use of microwave pulses in our experiment. In this section we will describe how the

¹More specifically we use the zero order from the AOM controlling the power of the cooler slave, see fig. 12.2.

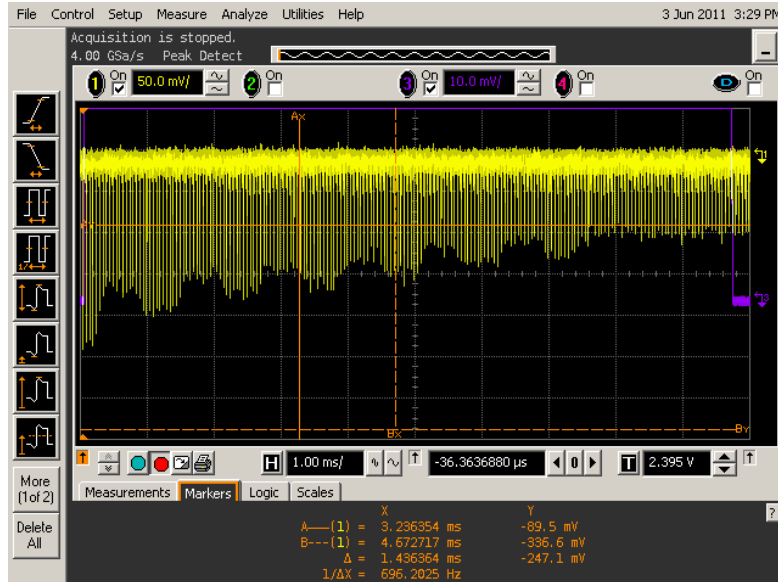


Figure 7.3: A screen shot of the scope, measuring the population in the $F = 4$ manifold (yellow) as the microwave frequency is swept across several hyperfine transitions. It is clearly seen how the population changes, which is due to the microwave becoming resonant with a hyperfine transition. Note that the frequency of the microwave is increasing from left to right.

daily calibrations of the pulse duration and transition frequency is done. To set the $\pi/2$ duration, τ_p , we start with all atoms in the $|3\rangle$ state and compare the result obtained by doing a $\pi/2$ and a $3\pi/2$ pulse. If $\tau_p > \tau_{\pi/2}$ the $\pi/2$ pulse will transfer more than half of the atoms to $|4\rangle$ and we will observe a positive signal², whereas after a $3\pi/2$ -pulse we will have more atoms in the $|3\rangle$ state and observe a negative signal. If $\tau_p < \tau_{\pi/2}$ the situation is reversed. Doing this iteratively we find the optimal setting for $\pi/2$ pulse duration.

To find the transition frequency, ω_{clock} , we run a Ramsey sequence, which is depicted in fig. 7.2. Starting with all atoms in the $|3\rangle$ state, and doing a $\pi/2$ pulse with a phase $\phi = 0$, this rotates the Bloch vector around the x -axis into the equatorial plane. Now waiting for a time τ according to eq. (6.20) the Bloch vector will precess in the equatorial plane³. The total precession angle will be given by $\theta = \tau\Delta_0$, where Δ_0 is the detuning of the microwave from the resonance. To convert this accumulated angle into a population difference (which is what we can measure) a $\pi/2$ pulse is done, now with a phase of either $\phi = \pi/2$ or $3\pi/2$, giving a rotation around the y axis either clockwise or counter-clockwise. The idea is now that, if $\theta = 0$ then we would obtain the same result for the two settings of the phase, whereas for $\theta \neq 0$ we will obtain either a positive or negative signal depending on the phase of the last microwave pulse. Again doing this iteratively we can find the optimal setting for the transition frequency. Note that the longer we wait, the more sensitive we become. Using this method we can normally optimize the frequency to within ≈ 50 Hz.

7.3 Magnetic field calibrations

As previously mentioned we have a pair of MOT coils and three coil pairs to compensate for static magnetic fields and give the magnetic bias field. In this

²For completeness we note that the sign of the signal is set by the chosen lock point of the MZI, and might as well just be negative.

³Remember that we are in a frame rotating with the atomic transition frequency.

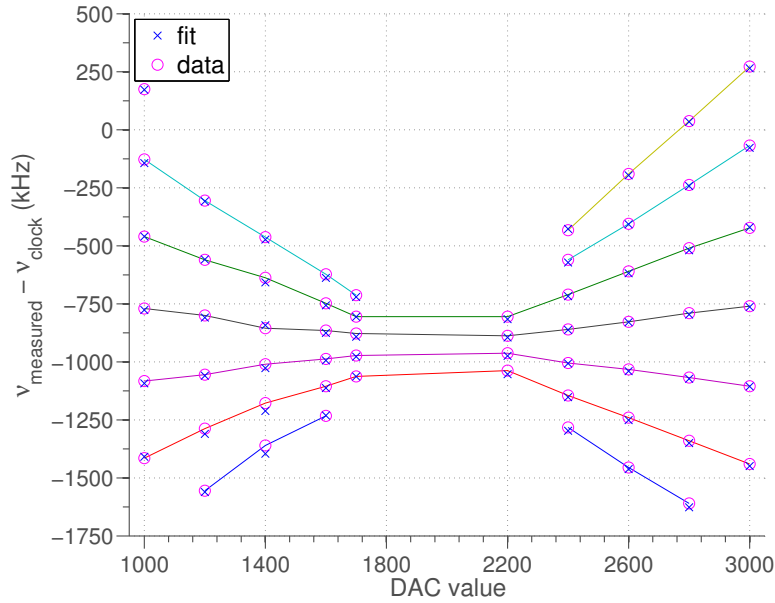


Figure 7.4: Frequencies of different hyperfine transitions as a function of the magnetic bias field, found via the adiabatic sweep described in the text. To convert DAC values to frequencies we combine all experimental points (magenta circles) into one data set and fit corresponding expected values (blue crosses). Note that the solid lines are *not* the fits, but hand drawn to emphasise which data points comes from the same hyperfine transitions.

section we first consider how the magnetic field from the compensation coils are calibrated, and afterwards consider the calibration of the much higher magnetic field coming from the MOT coils when they are used in a Helmholtz configuration. In this section we present data, showing that we have a satisfactory control of these fields.

Each pair of compensation coils is connected to a 12 bit digital to analogue converter (DAC) that can be interfaced over a USB port. To calibrate the magnetic bias field we start by bringing all atoms to the $F = 4$ hyperfine manifold, this is done by using the repumping laser, see sec. 7.1. We now turn on the microwave and do an *adiabatic* sweep of the microwave frequency while we monitor the population in the $F = 4$ hyperfine manifold. The sweep of the microwave will transfer atoms between the hyperfine levels via rapid adiabatic passage [Metcalf et al. 1999]. In figure 7.3 we show how the population evolves during the sweep of the microwave frequency. It is clear that at specific frequencies (times in the sweep) there is a change in the population which is due to the microwave having swept over a hyperfine resonance. Such sweeps are done for several settings of *each* coil pair, an example of the resulting data for a single coil pair is seen in fig. 7.4. By fitting to the expected linear relation, see eq. (2.1), we can find a conversion from DAC values (proportional to the current through the coils) to magnetic field strength. The simplest method would be to simply fit a linear relation to each independent hyperfine transition. Instead of this we combine all data points into one big set, and do a combined fit for all data in one go. In this way we fit (crosses in fig. 7.4) to the data (open circles in fig. 7.4), and to illustrate the individual hyperfine transitions we have connected such points by straight lines. For DAC values in the range of 1700-2200 the difference between the different transitions are so small, that they are hard to distinguish, which is the reason that no data points are found here. There is an almost perfect overlap between the fit and the data points, for all transitions at all magnetic field strengths, from the fit we can deduce two central parameters. From the

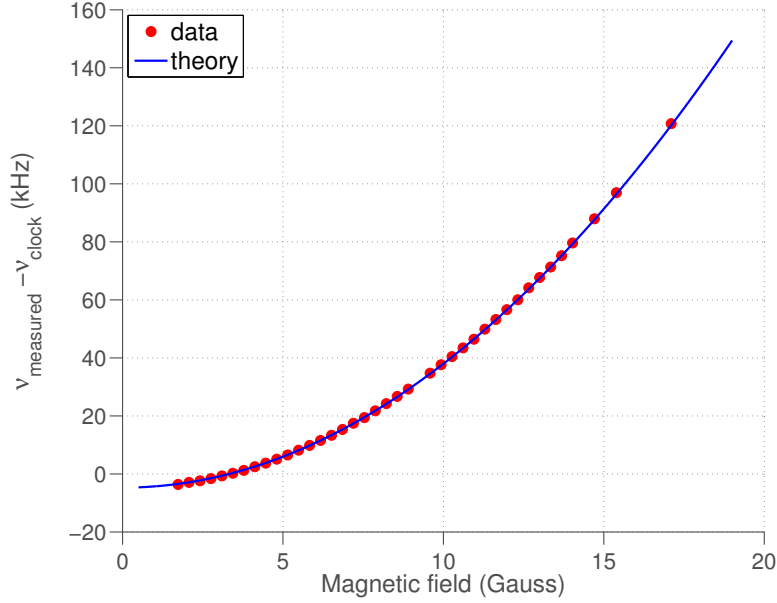


Figure 7.5: Quadratic shift of the clock levels as a function of the magnetic field, from the MOT coils. Note that the zero point of the theoretical curve has been shifted down, to take into account any offsets from the defined clock frequency.

linear relation we find the conversion factor between DAC values and magnetic field strengths. More importantly we also find the DAC value that corresponds to zero magnetic field strengths. If there is no magnetic field, then all the hyperfine levels are degenerate and will have identical transition frequencies. We note that the general offset of all transitions from the defined clock frequency, is expected and comes from other non-magnetic frequency shifts, with the main contribution from AC-Stark shifts.

As it will become clear in sec. 9.1 we need a bias field of tens of Gauss to create the single excitation state. This extra magnetic field is made by using the MOT coils in Helmholtz configuration. For this calibration we will use the transition between the two clock levels, which experience a quadratic Zeeman shift, see chapt. 2. For a given setting of the current through the coils we measure the transition frequency as described in sec. 7.2. From the current and the coil specifications⁴ we can calculate the expected magnetic field. In fig. 7.5 the shift of the transition frequency from the defined clock frequency is plotted as a function of the (from the current through the coils calculated) applied magnetic field. In this plot we have also shown the theoretical expected dependence with a shift of 427 Hz/Gauss^2 . We note that the theoretical curve is here plotted with an offset to take into account any shift that is not dependent on the magnetic field⁵. We see a good agreement between the theoretical expected shifts from the clock frequency and the ones measured in the laboratory. We note that using transitions where $\Delta m_F = \pm 1$ would allow for a higher sensitivity, we tried running a Ramsey sequence on such a transition ($|3\rangle \rightarrow |F=4, m_F=1\rangle$), but observed that we could not do a full transfer of the population via a π -pulse for higher magnetic fields. We expect this is due to fluctuations and inhomogeneities of the magnetic field. This problem was not investigate further due to the good agreement obtained via the quadratic shift of the clock levels.

⁴Radius of 5 mm and 38 windings per coil [Windpassinger 2008].

⁵This could for instance be the AC-Stark shift of the strong laser used for the dipole trap

Squeezing measurements

When all of our standard calibrations are done we are ready to start the “real” experiment. In this chapter we will present results showing the creation and characterization of a spin squeezed state. Note that the experiment was able to create such states (long) before my arrival, and that some credit for the results presented here goes to the pioneering experimentalists mentioned in the preface of this report, and their work have been published in [Appel et al. 2009a; Louchet-Chauvet et al. 2010]. The reason we still present them here is that many of the introduced methods will be useful later and that it is the first time we show squeezing of the single quadrature operators. In this chapter we give a detailed outline of the experimental implementation used to create spin squeezed states. We start by considering how many scattering events (decoherence) a single measurement on the atomic ensemble induces. After this we present the used method to generate the spin squeezed state together with results showing a clear noise reduction. Finally it is discussed how the obtained phase shift measurements can be converted into regularized atomic quadrature operators, when we are in the Holstein-Primakoff approximation. The results presented here have recently been uploaded to the arXiv and submitted to PRL together with methods allowing us to classify the generated state as non-classical [Kiesel et al. 2012].

8.1 Decoherence measurement

As it has been described, in sec. 4.2.1, the reported squeezing is measurement based. The first measurement will introduce scattering events which in effect reduces the number of coherent atoms in the ensemble. As described in sec. 4.2.2 we need to compare the noise of the state claimed to be squeezed *not* with the coherent spin state with the initial number of atoms, but with a coherent spin state with the reduced atom number. We model the reduction in the number of coherent atoms after the first measurement as

$$N_{\text{at}} = \tilde{N}_{\text{at}} \left(1 - e^{\eta N_{\text{ph}}}\right), \quad (8.1)$$

where η is the number of scattering events induced by one photon and \tilde{N}_{at} is the number of coherent atoms before the measurement.

To measure this reduction we consider the Ramsey fringe. As always we start with all atoms in the $|3\rangle$ state, then a $\pi/2$ pulse with $\phi = 0$ is sent to create a coherent spin state. Immediately after an *optional* probe pulse is sent and finally a $\pi/2$ -pulse with a variable phase $\phi \in [0, 2\pi]$. Afterwards the population difference is measured by 18 probe pulses, see fig. 8.1. This is followed by a measurement of the atom number, as described in sec. 8.2. The measured population difference

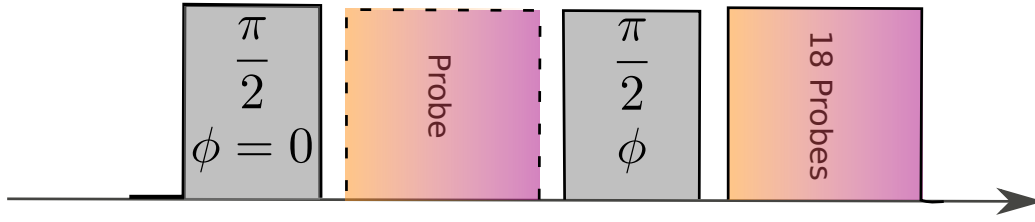


Figure 8.1: The pulse sequence used to measure the reduction of coherent atoms caused by a probe pulse.

is now normalized to the corresponding atom number measurement. With this we can map out the Ramsey fringe. We clearly see that if the phase of the second microwave pulse is zero, the two pulses form a π -pulse which flips the atomic population¹. If the phase of the second pulse is π the two pulses cancel each other and the population is in its initial state, resulting in an amplitude of -1 . Fitting a sine function allows us to deduce the amplitude and phase of the Ramsey fringe. From fig. 8.2, we clearly see that sending a probe pulse, in between the two microwave pulses, results in a lower amplitude of the Ramsey fringe. Since the Ramsey fringe contains information about the number of coherent atoms in the ensemble the fringe reduction is a direct measure of how many scattering events the probe pulse induces. In the Bloch sphere representation this reduction corresponds to a shortening of the Bloch vector ($|\hat{\mathbf{F}}| \propto N_{\text{at}}$). For the particular measurement shown we used $N_{\text{ph}} = 5.25 \cdot 10^6$ per pulse giving a reduction of the fringe amplitude of 5.2 %, corresponding to a decoherence parameter of $\eta = -1 \cdot 10^{-8}$. Later we will use a similar method to show that we can do a state selective excitation to the $F' = 4$ hyperfine manifold.

From the phases of the two Ramsey fringes presented in fig. 8.2 we get an extra, more precise check of the transition frequency and the cancellation of the differential AC-Stark shift. Assuming that the transition frequency is set perfectly then the minimum of the Ramsey fringe (with no probe pulse) should be at $\phi = \pi$. Any deviation from this is a sign that our transition frequency is non-optimal. Knowing the waiting-time in between the two microwave pulses we can calculate how big a correction to the transition frequency we need. By considering the difference between the two minimum positions of the Ramsey fringes we can see how well the two probes cancels the differential AC-Stark shift of the clock levels. If there is any differential shift between the two levels, then when the probe pulse is sent this will correspond to a rotation of the Bloch vector in the equatorial plane. This we would then observe as a shift of the minimum of the fringe with a probe pulse in comparison to the fringe without a probe pulse.

8.2 Squeezing measurement

To do the squeezing measurements, we start by optimizing the experimental apparatus. Below an outline of the central steps in this procedure

1. Optimization of the visibility of the MZI.
2. Balance the two outputs of the MZI.

¹From fig. 8.2 we see that the normalized amplitude does not reach exactly one. The explanation of this lies in the initial state preparation, where we have a small amount of atoms left in other hyperfine states, which the microwave pulse does not address.

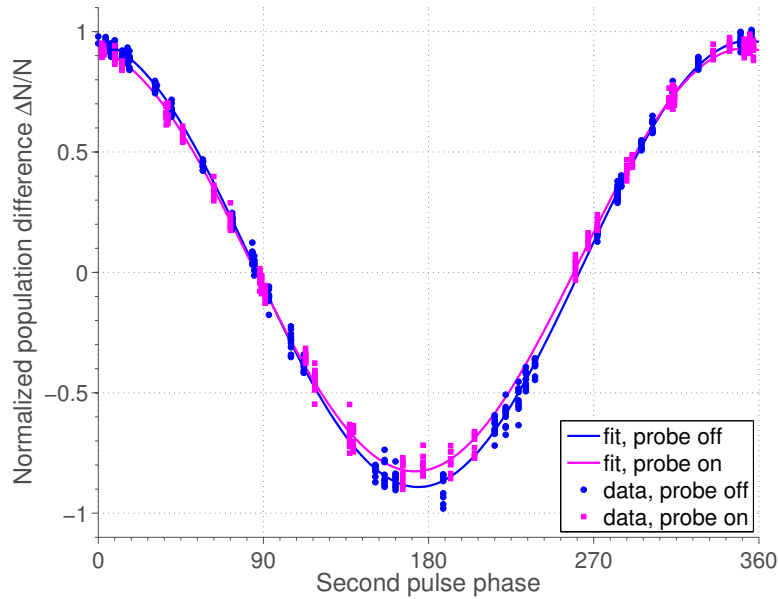


Figure 8.2: Plot of the Ramsey fringe for the decoherence sequence with and without the optional probe pulse in between the microwave pulses. It is seen that if a probe pulse with $5.25 \cdot 10^6$ photons is sent (magenta) the total amplitude is reduced by 5.2% giving $\eta = -1 \cdot 10^{-8}$.

3. Lock the MZI with an offset such that both probes are balanced individually.
4. Optimize $\pi/2$ duration.
5. Optimize the transition frequency.
6. Adjust the detuning of the probes such that the differential AC-Stark shifts of the two clock levels cancel. This can be done by a Ramsey like sequence, where we instead of waiting for a time τ send a probe pulse².
7. Do a decoherence run as described in sec. 8.1, to find η and as an extra check for the transition frequency and the cancellation of the differential AC-Stark shift of the clock levels.
8. Keep everything working around the clock (all locks and computers) for around 3 days.

As always via our state preparation we start with all atoms in the $|3\rangle$ state. Using a microwave $\pi/2$ pulse we create a coherent spin state and then send 20 separate probe pulses. After the last probe pulse we use the MOT repump light to transfer all atoms to the $|4\rangle$ state and again send 20 probe pulses which will allow us to deduce the number of atoms in the ensemble. This is repeated four times, and we thus get measurements for four different atom numbers in one MOT loading. After the last atom number measurements we use on-resonant light to kick out all atoms from the dipole trap. Four calibration measurements, where we measure the MZI baseline, i.e. the noise of the empty interferometer are done. We show a schematic of the measurement procedure in fig. 8.3. The data are acquired using an Agilent oscilloscope, where the full scope trace is saved. The data analysis is done in an *almost* identical manner to [Oblak 2010, sec. 12.2] here we will just outline the main points.

²A different method is to look at the zero point of the Ramsay fringe in fig. 8.2, as described in sec. 8.1.

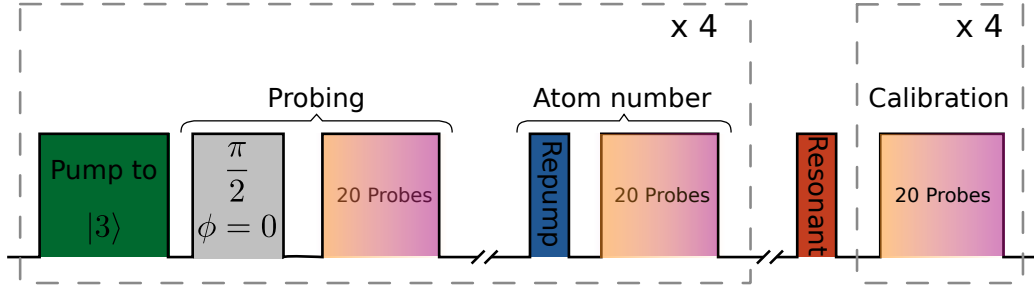


Figure 8.3: Pulsing sequence used for the creation and detection of the spin squeezed state. Starting with all atoms in $|3\rangle$ we create a coherent spin state by a $\pi/2$ -pulse, and afterwards send 20 probe pulses. Then all atoms are moved to the $F = 4$ manifold by using the MOT repump laser. This allows us to send 20 probe pulses from which we can deduce the atom number, this is repeated four times. After this on resonant light is shined onto the ensemble such that all atoms are removed from the trap. Now four calibration measurements of the interferometer baseline (noise) are done. Note that the relevant size of the pulse here do *not* represent the actual ratio of between the pulse durations in the experiment.

- We integrate the scope trace such that we for each pulse get a single value.
- ◊ To compensate for long term drifts of the experimental apparatus we subtract pulses from subsequent MOT cycles to create what we call two-point pulses. This is done *only* to allow us to find the projection noise of the created coherent superposition state. For the data showing the creation of a spin squeezed state, this subtraction is *not* done, which allows us to claim squeezing both in terms of the angular uncertainty of the Bloch vector and in the regularized atomic quadrature operators. This last part of the data analysis has not been presented in [Oblak 2010; Windpassinger 2008].
- From each measurement the corresponding MZI baseline is subtracted.
- The integrated pulse signal is converted to phase shifts, via a power reference measurement.
- The data are filtered, if a data file shows non-normal behaviour it is removed. We note that this is surely a delicate issue but the condition for removal are all based on independent measurements like probe powers and the empty noise of the MZI.
- The final thing is to combine subsequent probe pulses, this is a way of varying the photon number, and thus interaction strength, used in each measurement.

Doing the above, we get data as presented in fig. 8.4 and in the following present an analysis allowing us to characterize the spin squeezed state. We consider two subsequent measurements given by

$$\phi_{1/2} = \underbrace{\frac{\delta n_{1/2}}{n_{1/2}}}_{\text{shot noise}} + \underbrace{\frac{k\Delta N}{n_{1/2}}}_{\text{atomic noise}} . \quad (8.2)$$

We now use the information of ϕ_1 to make the best estimate of the outcome for ϕ_2 by forming the the conditionally reduced variance

$$\text{var}(\tilde{\phi}) = \text{var}(\phi_2 - \zeta\phi_1), \quad (8.3)$$

where ζ describes how much "information" from the first measurement is used to predict the outcome of the second measurement. We now consider the variance of the measurements using that the atomic ensemble is in a coherent spin state

$$\text{var}(\phi_{1/2}) = \text{var}\left(\frac{\delta n_{1/2}}{n_{1/2}}\right) + k^2 \text{var}(\Delta N) \quad (8.4a)$$

$$= \frac{1}{n_{1/2}} + k^2 N_{\text{at}}, \quad (8.4b)$$

we note the *linear scaling* with the atom number. Calculating the variance of $\tilde{\phi}$ we find [Louchet-Chauvet et al. 2010]

$$\text{var}(\tilde{\phi}) = \text{var}(\phi_2) + \text{var}(\zeta\phi_1) - 2\text{cov}(\phi_2, \zeta\phi_1) \quad (8.5a)$$

$$= \frac{1}{n_2} + \frac{1}{1+\kappa^2} k^2 N_{\text{at}}, \quad (8.5b)$$

where we have introduced the measurement strength

$$\kappa^2 = n_1 k^2 N_{\text{at}} \quad (8.6)$$

together with the optimal amount of information from ϕ_1 to use³

$$\zeta = \frac{\text{cov}(\phi_1, \phi_2)}{\text{var}(\phi_1)} = \frac{\kappa^2}{1+\kappa^2}. \quad (8.7)$$

Fitting a combined function to all the data ($\text{var}(\phi_1)$, $\text{var}(\phi_2)$ and $\text{cov}(\phi_1, \phi_2)$), allows us to distinguish different scaling of the noise with the atom number. We first note that we observe a large linear part which according to eq. (8.4b) is a sign of the atomic projection noise (dashed black line). We now compute $\text{var}(\tilde{\phi})$ for the cases where we have *not* subtracted subsequent experimental cycles (purple diamonds in fig. 8.4). We clearly see that the noise is below the expected projection noise, which means we have created a spin squeezed state. To quantify the amount of squeezing we use the criterion introduced in [Wineland et al. 1994] and obtain a noise reduction of -1.7 dB. It has been shown that if we have spin squeezing, in terms of the Wineland criteria, then we can also claim entanglement [Sørensen et al. 2001]. With this we now turn to the question of how the presented phase shift measurements can be converted in to regular quadrature operators together.

8.2.1 Quadrature measurements and tomography efficiency

There are several reasons for considering the atomic quadrature operators, the strongest is that it allows us to simplify the theoretical description of the atomic ensemble substantially. The main reason for this is that in introducing the quadrature operators we invoke the Holstein-Primakoff approximation which allows us to consider the tangential plane of the Bloch sphere instead of the curved surface. An other point is that the analogy to photonic states becomes more clear. From the pseudo-spin operators introduced in eq. (2.4) we introduce corresponding raising and lowering operators⁴ as

$$\hat{F}_{\pm} = \hat{F}_x \pm i\hat{F}_y, \quad (8.8)$$

with the commutator relation

$$[\hat{F}_+, \hat{F}_-] = 2\hat{F}_z. \quad (8.9)$$

³Done by simply minimizing $\text{var}(\tilde{\phi})$ with respect to ζ .

⁴Also called ladder operators.

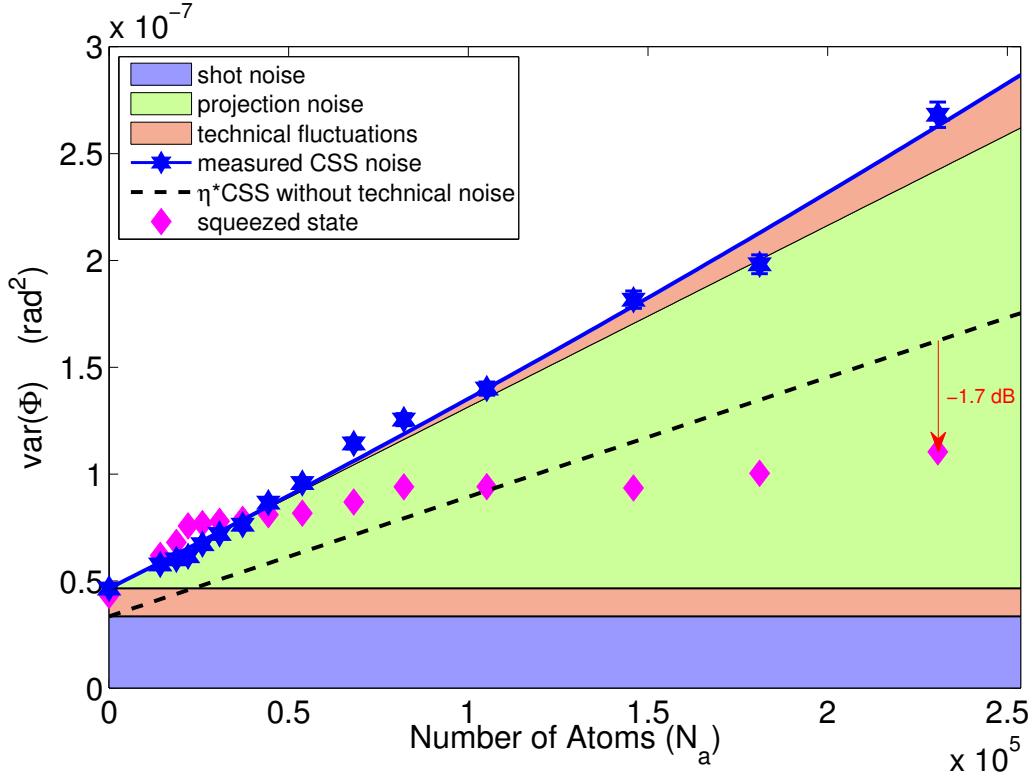


Figure 8.4: Plot of the angular uncertainty as a function of the atom number. By fitting a general quadratic function to the noise of a CSS (blue stars) we can distinguish different noise sources. By using the information obtained by one measurement to predict the outcome of a subsequent measurement we create a spin squeezed state (purple diamonds). We observe -1.7 dB of metrology relevant squeezing.

In the experiment we are in the Holstein-Primakoff approximation [Holstein et al. 1940] where the total spin is large and mainly aligned along⁵ \hat{F}_z direction. This allows us to treat \hat{F}_z classical by approximating by its expectation value, i.e. $\langle \hat{F}_z \rangle \approx f$, and only treat the two remaining spin components quantum mechanically. Using this in eq. (8.9) we get

$$[\hat{F}_+, \hat{F}_-] = 2f. \quad (8.10)$$

To obtain regular quadrature operators we start by rescaling the raising and lowering operators

$$\hat{f}_{\pm} = \frac{\hat{F}_{\pm}}{\sqrt{2f}}, \quad (8.11)$$

which directly leads to the generalized quadrature operator

$$\hat{f}_{\theta} = e^{i\theta} \hat{f}_+ + e^{-i\theta} \hat{f}_-. \quad (8.12)$$

In order to convert our phase shift measurements, ϕ , into samples of the quadrature we renormalizes them according to

$$\bar{f} = \frac{\phi}{\sqrt{\text{var}(\text{CSS}(N_{\text{at}}))}}, \quad (8.13)$$

where $\text{var}(\text{CSS}(N_{\text{at}}))$ denotes the total noise we measure for a coherent spin state with N_{at} atoms.

⁵The choice of considering the spin aligned along this direction is arbitrary, but done here to follow the convention used in [Kiesel et al. 2012].

To quantify how good our quantum state tomography is we consider the central parameter which is the signal to noise ratio of our measurement. Here the signal is the atomic projection noise (green in fig. 8.4) and the noise is everything else (technical noise and light shot noise). This leads us to introduce the effective quantum efficiency of our quadrature measurements

$$\epsilon = \frac{\text{var}(\text{CSS}(N_{\text{at}})) - \text{var}(\text{CSS}(N_{\text{at}} = 0))}{\text{var}(\text{CSS}(N_{\text{at}}))}. \quad (8.14)$$

In the measurements presented in sec. 8.2 we obtain values of $\epsilon = 80\%$, note that this is dependent on the number of atoms. A central point to note is that the contribution of atomic noise to $\text{var}(\text{CSS}(N_a))$ scales quadratically with N_{ph} in the probe, and the shot noise contribution *only* scales linearly [Hammerer et al. 2010]. For tomography applications it is not needed to preserve the non-destructiveness of our QND probing method – that is to preserve the coherence between the states $|3\rangle$ and $|4\rangle$. Therefore, neglecting technical noise, a probe of unlimited strength can in principle be used, and the quantum efficiency of the tomographic measurement can then approach unity.

Towards generation of an atomic Fock state

In this chapter we present preliminary results for our proposed method of creating and detection of a non-Gaussian, state of the atomic ensemble, made by creating a collective single excitation. We start by considering how we can adapt the methods of chapt. 5 to the multilevel structure of Cs and implement it in our setup. After this we consider the requirements one by one, starting with the need for state selective excitation. We show that with a bias field of ≈ 30 Gauss we can see the splitting of the $|F' = 4, m'_F = \pm 1\rangle$ hyperfine states. The single photon detection, where we especially focus on the frequency filtering is discussed. It is shown that we can reject the photons originating from the excitation beam with a ratio of $1 : 10^6$. To support these preliminary results we present a simulation showing that our proposal is feasible. The presented material have recently been submitted to a special issue of the New Journal of Physics on quantum tomography, and can be found on the arXiv [Christensen et al. 2012].

9.1 Implementation in experimental setup

We will again consider the pseudo two level system formed by the clock levels, $|3\rangle$ and $|4\rangle$. As the excited state used to couple the two clock states we use the $|e\rangle \equiv |F' = 4, m'_F = +1\rangle$ state of the D2 transition. To create the single excitation state described by eq. (5.2b) we propose the following procedure: initially all atoms are prepared in the $|4\rangle$ state using our standard state preparation methods, see sec. 7.1. The collective excitation is created by a weak excitation pulse, blue detuned by $\Delta \approx \frac{3}{2}\Gamma$ from the $|4\rangle \rightarrow |e\rangle$ transition. The detuning is chosen such that the optical depth is less than unity¹ which means that all atoms will have roughly the same probability to scatter a photon and the created excitation will be collective, i.e. shared uniformly by the whole ensemble.

To obtain the best spatial overlap between the probe and excitation beam with the atomic ensemble the excitation beam will arrive at the MZI via the same single mode optical fiber as the probe beam. This perfect overlap of the light beams, comes with the constraint that the polarization of the excitation beam and the probe beams are now identical. With the quantization axis (defined by the magnetic bias-field) chosen orthogonal to the propagation direction of the beams, we can only address π or $x = (\sigma^+ - \sigma^-)/\sqrt{2}$ polarized light. In order to obtain the highest efficiency of the atomic tomography it is preferable to use

¹Which is calculated assuming an on resonance optical depth of 10.

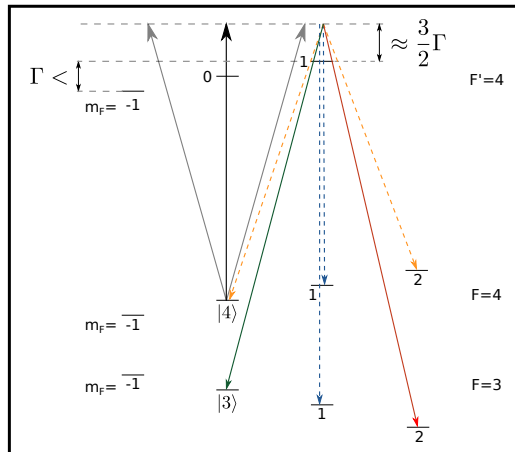


Figure 9.1: The levels of interest in Cs atoms. The dashed lines indicates decay channels which can be filtered out by applying frequency (orange) and polarization filtering (blue), and the full lines decay channels that can *not* be filtered out. Note that the decay to $|F = 3, m_F = 2\rangle$ will be an unavoidable inefficiency of the implementation method.

π -polarized light² [Louchet-Chauvet et al. 2010]. Considering the complicated multi-level structure of the Cs atoms will constrain the excitation and probe geometry. Since the $m_F = 0$ atomic wave functions are symmetric, anti-Stokes photons from the Raman transition $|4\rangle \rightarrow |F' = 4\rangle \rightarrow |3\rangle$ cannot be emitted into the forward direction in the absence of an external magnetic field. In order to break this symmetry and to allow for forward scattering of Raman photons into the $|3\rangle$ level we apply a magnetic bias field and the light polarization is adjusted to contain an x -component, as described in sec. 6.2.1. The applied bias field is approximately 20 Gauss shifting the $|F' = 4, m'_F = -1\rangle$ out of resonance by several line widths (≈ 15 MHz), see fig. 9.1. This combined with the fact that the $|4\rangle \rightarrow |F' = 4, m'_F = 0\rangle$ transition is forbidden by selection rules allows us to achieve the selective excitation to the $|e\rangle$ state, together with the possibility of a forward scattered Raman photon. From the $|e\rangle$ state the atom can undergo spontaneous emission through six possible decay channels, see fig. 9.1. Applying different filtering methods allows us to conclude that if a photon is detected the atom will have decayed via the $|e\rangle \rightarrow |3\rangle$ transition, which signals that the ensemble is in the single excitation state given by equation eq. (5.2b). Photons that are π polarized can be distinguished by using a polarized beam splitter cube or other polarizing selective elements. The harder task is to filter photons that are x polarized coming from decay to the $|F = 4\rangle$ ground state. Since this requires us to distinguish photons with a frequency difference of approximately 9 GHz, see sec. 9.3. To do this we propose to use two identical filter cavities in succession. Assuming this can be done in a satisfactory manner, we can filter out all but one of the undesired decay channels. The photons emitted when the atom decay through the $|e\rangle \rightarrow |F = 3, m_F = 2\rangle$ transition can not be filtered. This decay channel has the same polarization as the desired photon and the frequency difference between them is in the MHz range (the Zeeman splitting of the ground state), making it experimentally very hard to distinguish between them. We will thus accept this implicit imperfection and in sec. 9.5 estimate its effect. It is noted that the branching ratios favour the desired decay by almost a factor of 4.

When the single photon is detected we can now proceed in a similar fashion to the case of the squeezed state, see 8.2. Applying a $\pi/2$ pulse interferes the

²This is due to problems with optical pumping to other hyperfine states which can happen if σ^\pm light is used.

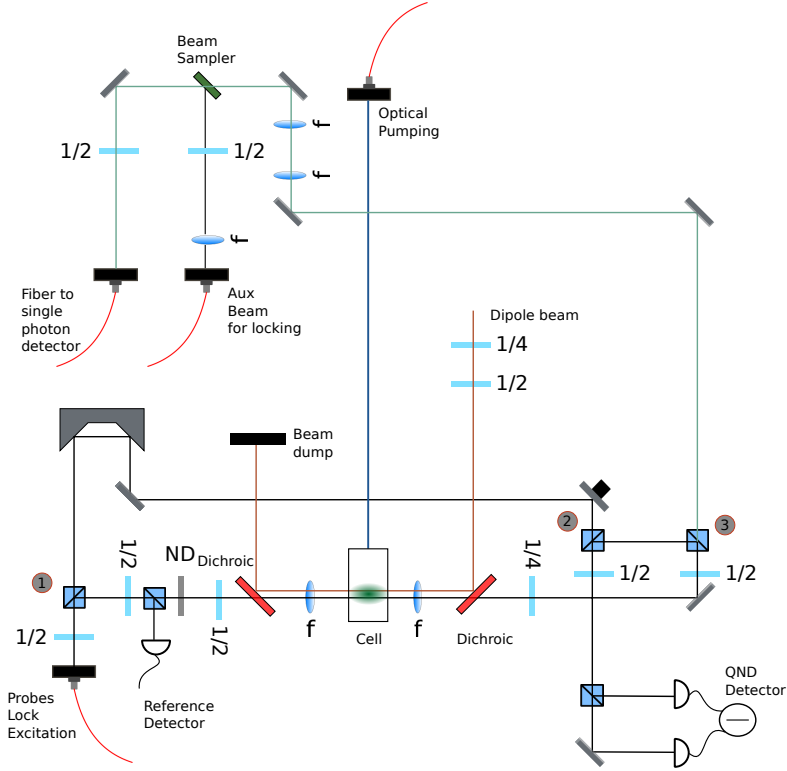


Figure 9.2: Schematic of the setup used to generate and detect the single excitation state.

atoms in the two states. Afterwards performing the dispersive probing we can measure the observable \hat{F}_z . Repeating this procedure several thousands times we can characterize the marginal distributions of \hat{F}_z for the generated atomic state. Since we do not require any QND measurement we can perform a destructive measurement (use many photons) in order to optimize the tomography efficiency, ϵ . Note that due to the cylindrical symmetry of the Wigner function (see fig. 5.3), for the single excitation state the $\pi/2$ rotations can be performed without paying attention to the phase of the microwave pulse which corresponds to the axis of rotation on the Bloch sphere.

Before we continue and present preliminary results we take a quick look at how the last part of the interferometer setup has been changed. If the collective excitation is made, and the desired photon is emitted will get transmitted at the PBS marked 3 on fig. 9.2, due to its x polarization. From here on it is coupled into a single mode fiber with an efficiency of 75%, the output of this fiber is sent through filter cavities before it arrives at the single photon detector. To lock the filter cavities we overlap a bit of extra light onto the single photon path, see sec. 9.3.

9.2 State selective excitation

In this section we present results showing that by using a high magnetic bias field we can split the excited $F' = 4$ hyperfine manifold and thus do the required state selective excitation. The ensemble is prepared such that the Bloch vector is pointing towards the south pole, which means that all atoms are in the $|3\rangle$ state. Doing the pulsing sequence depicted in fig. 9.3, we can map out a Ramsey fringe, we note the similarity to the measurement method described in sec. 8.1. In the following the polarization of the excitation beam contained 20% of x polarization.

We now do measurements as described above for a varying detuning (set by

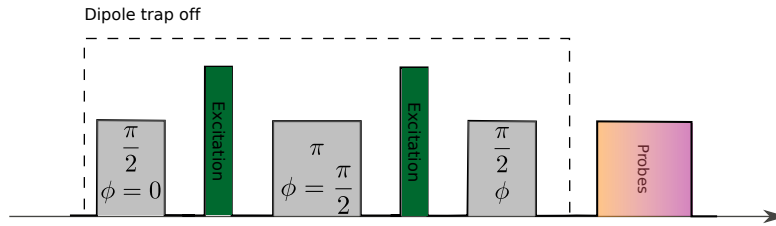


Figure 9.3: The pulsing sequence used to measure the level splitting of the $F' = 4$ excited hyperfine manifold. All atoms are initially prepared in the $|3\rangle$ state, and we then send a microwave $\pi/2$ pulse which creates a coherent superposition state. We now send a short excitation beam with a variable frequency. To cancel inhomogeneities we apply an echo sequence using a π pulse. Finally we rotate the state with a $\pi/2$ pulse with a phase of either $\phi = 0$ or $\phi = 180$. The final state is thus all atoms down or up. With this we can find the Ramsey fringe amplitude, which measures the number of *coherent* atoms we have in the ensemble.

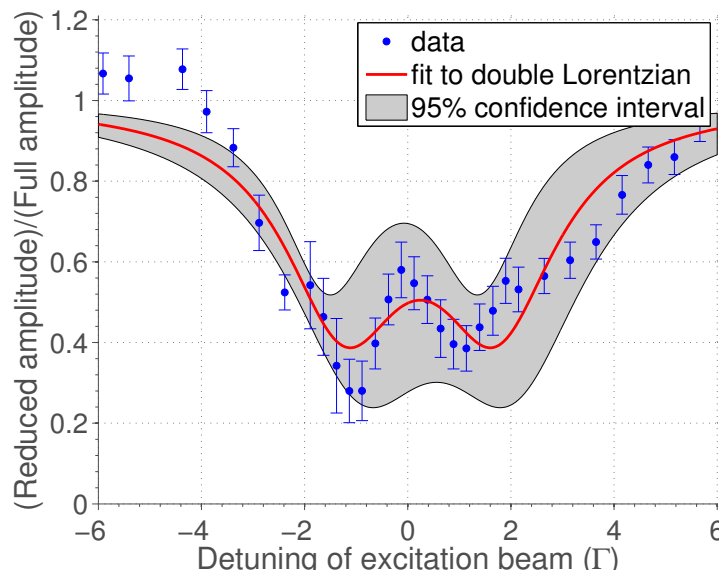


Figure 9.4: The reduction of the Ramsey fringe (coherence of clock states) as a function of the detuning of the excitation beam from the $|4\rangle \rightarrow |F' = 4, m_F = 0\rangle$ transition in units of $\Gamma = 5.2$ MHz. The excitation beam consists of $1.6 \cdot 10^5$ photons with x polarization and $6.3 \cdot 10^5$ photons with π polarization.

an AOM) of the excitation beam. This allows us to measure the reduction of the Ramsey fringe amplitude as a function of the excitation beam detuning, see fig. 9.4. This measurement is done with a magnetic bias field of 30 Gauss. We fit the data by a dual Lorentzian function (forced to go to unity at plus and minus infinity) and see that there are two clear dips, corresponding to transitions to the $|F' = 4, m_F = \pm 1\rangle$. We also see an asymmetry in the data showing a larger absorption for transitions to $|F' = 4, m'_F = -1\rangle$ than $|F' = 4, m'_F = +1\rangle$. This asymmetry could be due to a non-perfect alignment of the magnetic bias field with the vertical direction, such that when the waveplate is turned to obtain the desired polarization mismatch we do not create an equal superposition of σ^+ and σ^- light. Instead we favour the σ^- polarization. From fig. 9.4 we also see that if the excitation is far below the resonance the reduction in fringe amplitude becomes larger than unity. This is clearly non-physical, since we in no way can gain extra atoms by this procedure, at the moment we have no clear explanation for this, but expect it to be linked to the atomic motion.

Before this final sequence we tried methods with the dipole trap on and without

the echo pulse. None of those worked, which is mainly due to the large inhomogeneous broadening of the transition due to the dipole laser. Using the echo sequence we are sure that the last $\pi/2$ pulse takes us to either the minimum or maximum of the Ramsey fringe, which reduces the data acquisition time substantially.

To support the data we calculate the theoretical expected line shape. As described in sec. 8.1 the amplitude of the Ramsey fringe is *not* a direct measure of the absorption but measures the number of *coherent* atoms in our ensemble. We start by defining the fraction of coherent atoms as

$$C(z) \equiv \frac{N_{\text{coh}}(z)}{N_{\text{at}}}, \quad (9.1)$$

Using [Appel et al. 2009a][eq. (S6)] we can write this as

$$C(z) = \exp\left(-\alpha \frac{N_{\text{ph}}(z)}{\mathcal{N}_{\text{col}}}\right), \quad (9.2)$$

where α is the absorption coefficient and \mathcal{N}_{col} is the atomic column density. We now use Lambert-Beer law giving

$$N_{\text{ph}}(z) = N_{\text{ph}}(z=0)e^{-\alpha z}. \quad (9.3)$$

Inserting this into eq. (9.2) and averaging over the atomic ensemble we find

$$\bar{C}(z) = \frac{1}{l_a} \int_0^{l_a} C(z) dz \quad (9.4a)$$

$$= \frac{1}{l_a} \int_0^{l_a} \exp\left[-\alpha \frac{N_{\text{ph}}(z=0)e^{-\alpha z}}{\mathcal{N}_{\text{col}}}\right] dz \quad (9.4b)$$

$$= \frac{1}{\alpha l_a} \int_0^{\alpha l_a} \exp\left[-\alpha \frac{N_{\text{ph}}(z=0)e^{-x}}{\mathcal{N}_{\text{col}}}\right] dx \quad (9.4c)$$

$$= \frac{1}{\text{OD}} \int_0^{\text{OD}} \exp\left[-\text{OD} \frac{N_{\text{ph}}(z=0)e^{-x}}{N_{\text{at}}}\right] dx, \quad (9.4d)$$

which can be solved. We note that the optical depth, OD, is depending on the detuning from a given transition. In this case it is a double Lorentzian function of the detuning, with this we get the line-shape presented in fig. 9.5. It is thus clear that we can resolve the excited state splitting, which was one of the requirements for the generation of the non-Gaussian state. We now consider the requirement of filtering of single photons.

9.3 Single photon detection

One of the big challenges in the creation of the single excitation state is the single photon detection. Detection of photons from the undesired decay channels will result in false positive “clicks”, i.e. we detect a photon but the atomic ensemble is not prepared in the desired single excitation state $|\Psi_1\rangle$. Such “clicks” could be due to dark counts, leakage of the probe-, trap- or excitation-beams. Since the state generation is based on the detection of a single photon with a low success probability, false positives essentially mix in realizations prepared in the vacuum state ($|\Psi'_0\rangle$)

The biggest problem is the possible leak of the excitation beam from either the fundamental or higher order modes of the cavity. The polarization filtering can simply be done with a PBS or other polarizing selective element. The harder task is the required frequency filtering, where we need to distinguish photons with a frequency difference of approximately 9 GHz.

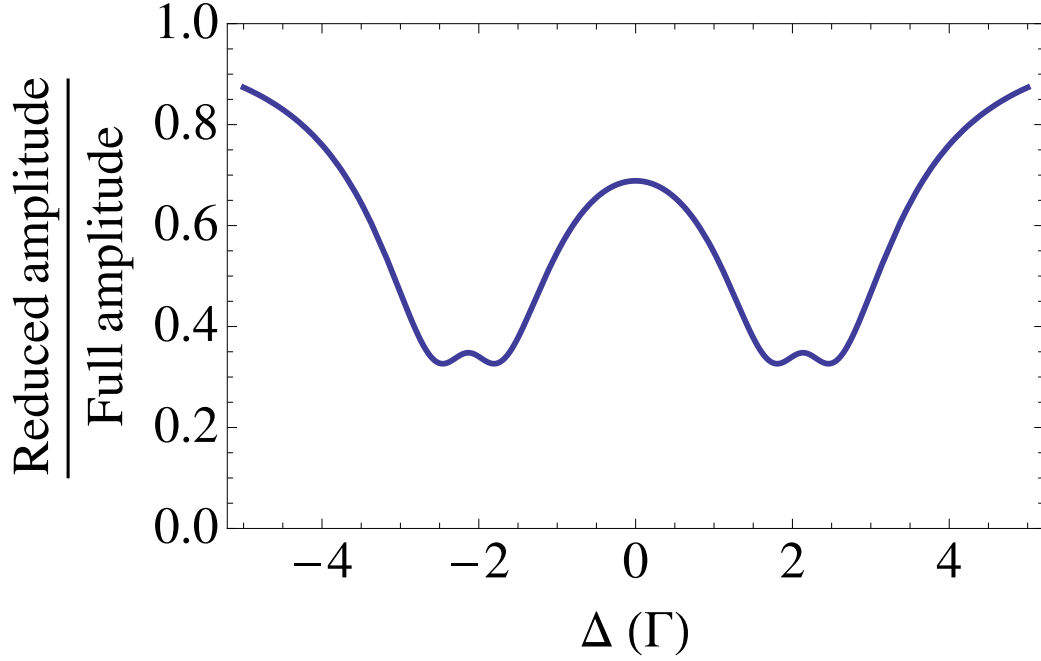


Figure 9.5: The theoretical calculated reduction of the Ramsey fringe amplitude as a function of probe detuning, a resonant optical depth of 10 is assumed. The clear similarity to the data in fig. 9.4 is pointed out.

9.3.1 Filter cavities

The frequency filtering is done with two identical filter cavities in succession, and in this section we will consider the design ideas and characterize of these. The simple goal of the filter cavities is to transmit light at the frequency of the single photon, ν_{SP} , and reject light at the frequency of the excitation beam, ν_E . In the laboratory we do not have light at the frequency of the expected single photon which could be used to lock the cavities. Instead we use light at the frequency of the excitation beam, and when we are expecting the single photon we will do a step of the cavity such that it will be on resonance with the single photon. We design the cavity such that one free spectral range (FSR) equals an integer number of the transversal mode spacing (TMS). We use two identical Layertech mirrors³ with a radius of curvature, $ROC = 250$ mm and a reflectivity of $R = (99.0 \pm 0.5)\%$. We now consider the higher order mode splitting in a confocal cavity given as [Kogelnik et al. 1966]

$$\nu = \text{FSR} \cdot \left[(q + 1) + \frac{m + n + 1}{k} \right], \quad (9.5)$$

where q is the longitudinal mode number and m and n characterize the transverse resonator mode. We have introduced

$$k \equiv \frac{\pi}{\arccos\left(1 - \frac{d}{ROC}\right)}, \quad (9.6)$$

here k is the number of higher order modes inside one FSR and d is the mirror separation. The free spectral range is now

$$\text{FSR} = \frac{c}{2d'}, \quad (9.7a)$$

$$= \frac{c}{2 \cdot \text{ROC} \cdot \left[1 - \cos\left(\frac{\pi}{k}\right)\right]}, \quad (9.7b)$$

³For internal use this mirror is named as M78.

Table 9.1: Table showing the parameters of the filter cavity, for the relevant parameters both the design parameters and the measured are presented.

Parameter	Calculated	Measured
FSR (MHz)	7882	7848
TMS (MHz)	985	981
$\delta\nu_c$ (MHz)	24	26
Finesse	312	301

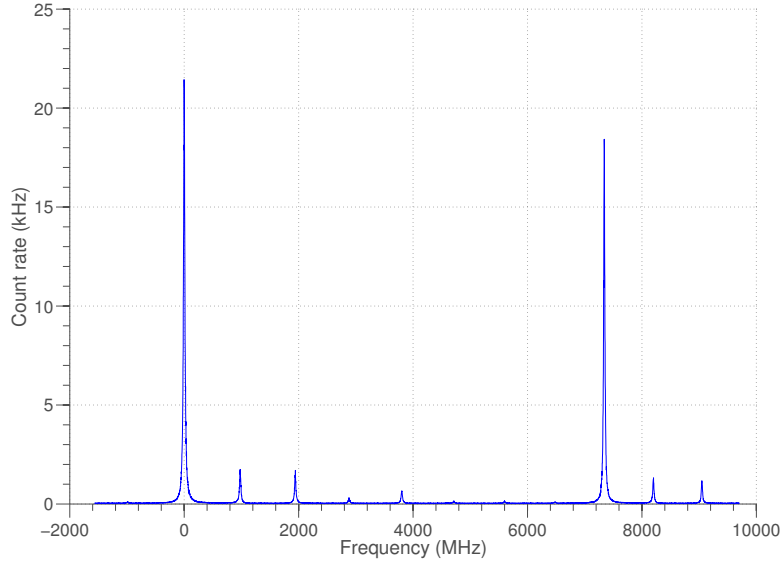


Figure 9.6: A scan over one FSR of the first filter cavity, where we have shifted one of the TEM₀₀ modes to zero. We clearly see the higher order modes present. Using the full piezo scan range we can see around 10 full FSR.

in which we have used the definition of k . The required step should ideally be such that we are right in the middle of two higher order modes of the excitation beam. In terms of the transversal mode splitting the step is given as

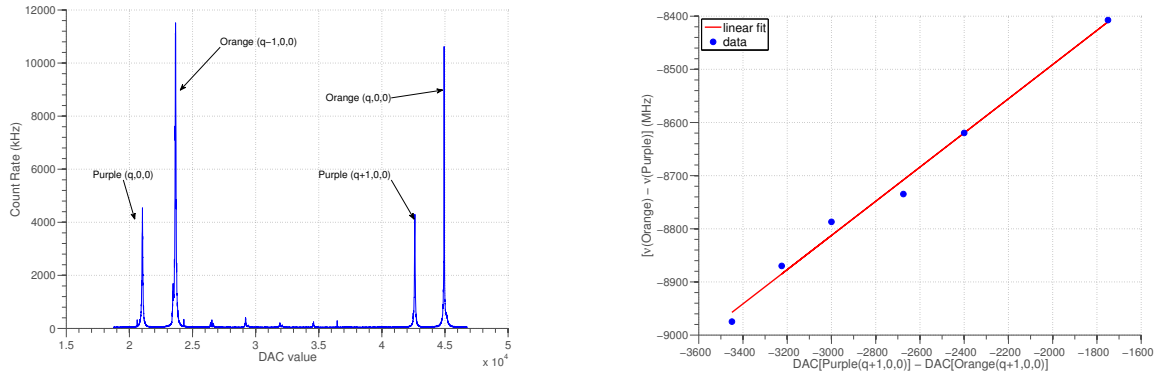
$$s = \frac{\nu_{SP} - \nu_E}{\text{TMS}} \quad (9.8a)$$

$$= (\nu_{SP} - \nu_E) \frac{2 \cdot \text{ROC} \cdot k}{c} \left[1 - \cos\left(\frac{\pi}{k}\right) \right] \quad (9.8b)$$

Calculating for a few values of k we find that if we take the 8th higher order mode to overlap with one FSR, the single photon is expected to be roughly in between two cavity modes of the excitation beam. With this criteria we get a mirror separation of $d = 19$ mm and calculate the relevant cavity parameters, see table 9.1.

The cavity is build inside a Thorlabs lens tube, with one of the mirrors mounted on a low voltage piezo allowing us to scan the cavity length. The piezo is controlled by an 18 bit digital to analogue converter (DAC) which is connected to an Atmel microcontroller chip that can be interfaced over USB. Scanning the piezo position, we obtain the cavity spectrum see fig. 9.6. Note that we have shifted the first TEM₀₀ mode to be our zero point and converted DAC values to frequencies⁴. We see that the first few higher order modes are clearly present

⁴How this conversion has be found will be explained in a bit.



(a) A scan of the cavity with both the orange and purple probe, with the orange having approximately twice the power of the purple, allowing us to distinguish resonances for each probe.

(b) The frequency difference as a function of difference in DAC values of the $(q + 1, m = 0, n = 0)$ purple mode and the $(q, m = 0, n = 0)$ mode of the orange probe.

Figure 9.7: Converting DAC values to frequencies and estimating the FSR of the cavity.

in the cavity spectrum, but they are strongly suppressed in comparison to the TEM_{00} mode. To find the cavity line width, $\delta\nu_c$, we fit a Lorentzian function to the TEM_{00} peak and get $\delta\nu_c = 26$ MHz.

Naively we could also find the FSR from the cavity scan in fig. 9.6 by fitting a dual Lorentzian. The problem with this is that the piezo position is a non-linear function of the applied voltage. This effect is most significant over large scales, and to suppress it we will try to work in a range where we only consider smaller differences in DAC values. The other thing we need is a known frequency reference in the cavity spectrum.

We use the two probe lasers (orange and purple), with the orange being twice as strong and send them through the cavity. We now record the cavity spectrum for a few settings of the frequency difference between the orange and purple probes. From the spectrum we can find the difference in DAC values between the $(q, m = 0, n = 0)$ of the orange laser and the $(q + 1, m = 0, n = 0)$ mode of the purple laser see fig. 9.7(a). The difference in DAC values will be in the order of a few thousands DAC values, and we will thus have minimized the effect of the piezo non-linearity. Now fitting a linear function, see fig. 9.7(b) to the data points we can find the frequency conversion to be 0.322 MHz/DAC. By extrapolating to zero difference in DAC values we find $FSR = 7848$ MHz, which is in good agreement with the desired design parameters, see table 9.1. Having characterized the cavities we now turn to the task of how to lock them.

Cavity locking

To lock the cavities we will implement a jitter lock, in this section we will outline the methods used together with a characterization of the lock itself. We start by considering the experimental setup, see fig. 9.8. The output from the fiber is sent through two dichroic mirrors which will reflect any leak light from the dipole trap with $\lambda = 1064$ nm, and transmit the single photon and excitation light with $\lambda = 852$ nm. Next the light gets coupled into the first filter cavity, and with a beam sampler we split off around 5% of the transmitted light (the cavity transmission is just below 80%) which will be used to lock the first cavity. In the beam path we have installed a mechanical shutter which can be used to block the beam. After the shutter the light gets overlapped with the transmission from the

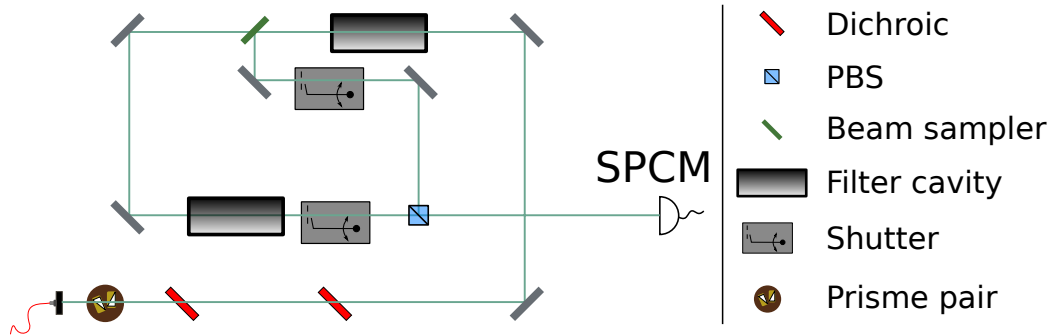


Figure 9.8: A schematic of the optics used to do the frequency filtering before the single photon counter. To lock both cavities we use the SPCM.

second cavity on a PBS before it hits the single photon counting module⁵ (SPCM). The light which gets transmitted through the beam sampler gets coupled into the second filter cavity, whose output goes to the overlapping PBS and then onto the SPCM. We have also inserted a shutter into this beam path.

The first thing required for the locking is that we are able to set the piezo to a position within the capture range of the lock, which is roughly three cavity line widths⁶. This is done by quickly scanning the cavity over one FSR, and count photons at every piezo position. To avoid the problem of the non-linear piezo and thermal drifts, the scan is repeated in a smaller range around the found maximum. This procedure is done repeatedly until the scan range is on the order of the cavity line width. After this we position the piezo where we found the highest count rate and switch on the lock. The locking is done by jittering the piezo around the assumed peak position in steps of half the cavity linewidth. If we get more counts one side compared to the other, we adjust the piezo accordingly. In fig. 9.9 we show the central parameters of the lock, especially note how the count rate on each side of the resonance is identical, and that it is half of the on-resonant count rate. With the first cavity now locked the light used to lock the first cavity is blocked, and the transmitted light from the second cavity onto the SPCM is unblocked. A similar procedure is now done, allowing us to find the maximum in transmission for the second cavity. To keep both cavities locked, we jitter the two cavities individually and again adjust the piezo accordingly.

Rejection

The final, and most relevant parameter of our cavity system is the total rejection. To measure this we use three lasers, the two probes (orange and purple) together with the excitation beam. We set the frequency of the orange probe to be identical to that of the excitation beam and the purple probe is set to be identical to the frequency of the expected single photon. The idea is the following

1. The cavities are locked to the excitation beam.
2. We step the cavity such that they are on resonance with the expected frequency of the single photon (done by using the purple probe).
3. Turn on the orange laser with an adjustable amount of power.

⁵We use a PerkinElmer SPCM-AQR-12

⁶The capture range is set by how long we count photons at each piezo position. For the lock to work, we have to count for long enough such that we can clearly distinguish photons transmitted through the cavity from the background

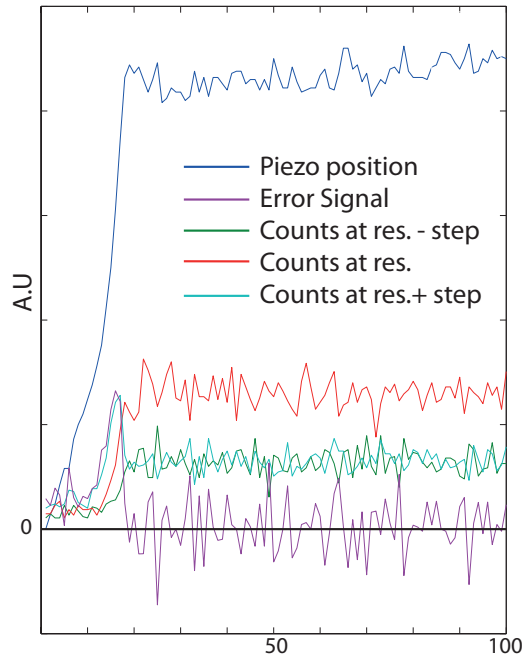


Figure 9.9: A plot showing the central parameters during 100 lock jitters. Note how it only takes around 20 lock jitters for us to find the maximum.

4. The cavity is scanned over a range which is so small that we do *not* see the fundamental mode of the high power orange laser, which would saturate the SPCM.

To be able to adjust the orange power we use a set of calibrated attenuators, this allows us to calculate the on-resonance count rate for the orange laser. Knowing this together with the count rate at the resonance for the single photon we find a rejection on the order of $1 : 1 \cdot 10^6$. As it will be explained in sec. 9.5 we need to distinguish 1 in 13000 photons, and with this rejection we will be able to.

9.4 Projection noise limited

It is clear that one of the biggest demands for the implementation is for our experimental apparatus to be projection noise limited at the required high bias field. To show this we have made an experimental run similar to the squeezing run, see chapt. 8, with a bias field of 20 Gauss. Performing our normal noise scaling analysis to distinguish the different noise sources, see fig. 9.10, we see a clearly linear scaling indicating the large contribution of atomic noise. We also note a larger amount of quadratic noise compared to the noise scaling performed for the spin squeezing state, see 8.2. This is due to the extra magnetic bias from the MOT coils which add extra noise.

9.5 Simulation

In this section we present a way to show and quantify the non-Gaussian character of the single polariton state. We calculate the expected marginal distributions for *experimentally valid* parameters and perform a simulation similar to Dubost et al. [Dubost et al. 2012]. The first goal is to estimate the probability that if a single photon is detected the atomic ensemble is in the single excitation state. In order to do this we assume that the excitation pulse is so weak that the probability of creating an excitation in the atomic ensemble is 5%. To obtain this creation

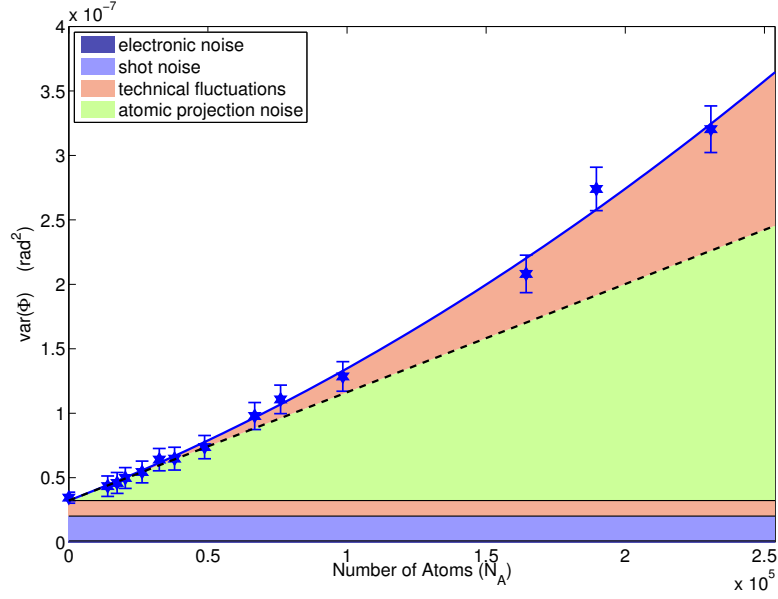


Figure 9.10: Plot of the variance of the measured angular uncertainty as a function of atom number, with different noise contributions singled out via a noise scaling analysis.

Table 9.2: Conditioned on obtaining a click, we show the probability of the most probable origins.

Origin of photo-count	State	Probability (%)
Dark count	$ \Psi_0\rangle$	8.7
Excitation leakage	$ \Psi_0\rangle$	0.6
$ e\rangle \rightarrow F = 3, m_F = 2\rangle$	$ \Psi_0\rangle$	19.1
$ e\rangle \rightarrow 3\rangle$	$ \Psi_1\rangle$	71.5

probability we need 13250 photons in the excitation beam and take its duration to be $10\mu\text{s}$. We use the following parameters for the simulation, the polarization filtering can be done by a polarizing beam splitter cube which has a rejection of $1 : 7 \cdot 10^3$. For the frequency filtering we obtain rejections of $1 : 5 \cdot 10^7$ by using two filter cavities in succession each having a transmission of 75%. We note that a different number is used here than the $1 : 1 \cdot 10^6$ measured in sec. 9.3.1. The justification for this is that measuring the rejection of the first cavity alone we find $1 : 700$. With identical cavities we expect a similar rejection for the second cavity, giving a total rejection of $1 : 5 \cdot 10^7$, we thus expect to improve the rejection presented in sec. 9.3.1. The detection efficiency of the single photon mode is taken to be 80%, and the quantum efficiency is 40% and we will assume the effective quantum efficiency of the tomography to be $\epsilon = 0.5$. With this we can estimate the probability that *if a photon is detected* whether it came from a specific decay channel, whether it was a dark count of the detector or light leakage. The most interesting cases are shown in table 9.2, note that we have only kept the most important origins, and neglected cases where the probability is smaller than 0.5%.

With these parameters we can now estimate the marginal distributions we would obtain by the proposed implementation. We model the state as a statistical mixture

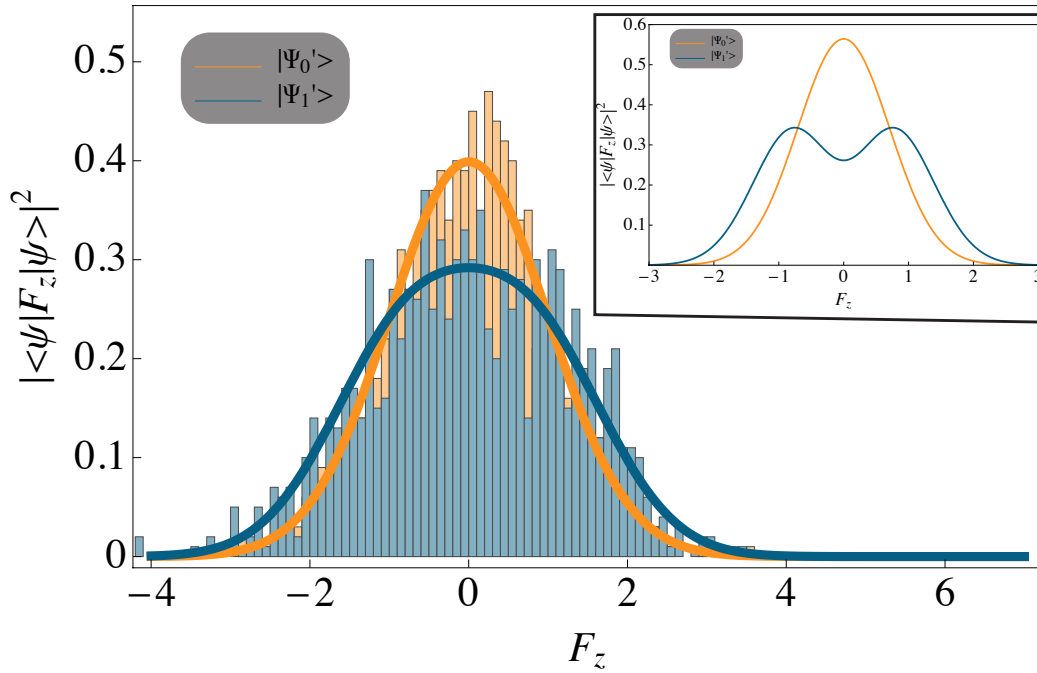


Figure 9.11: Marginal distributions for the single polariton state (blue) and the CSS (orange), both corrected for the decrease in detection efficiency, with a histogram based on 1000 samples from each distribution. Insert show marginal distributions which are *not* corrected for the decrease in detection efficiency. We clearly note that the detection washes away the non-Gaussian feature, and how hard it is to distinguish the two histograms.

of $|\Psi_1'\rangle$ and $|\Psi_0'\rangle$ weighted by their corresponding probabilities, see table 9.2

$$\hat{\rho} = p|\Psi_0'\rangle\langle\Psi_0'| + (1-p)|\Psi_1'\rangle\langle\Psi_1'|. \quad (9.9)$$

As all other measurements our dispersive probing will add extra noise to the real marginal distributions. Our meter is light and our detection is shot noise limited, thus the extra noise contribution will be the shot noise of light. Following the approach in [Appel et al. 2007] we can model this as a decrease in detection efficiency. In effect this degrades the non-Gaussianity of our state, see fig. 9.11.

As it is clear from the discussion in [Dubost et al. 2012] the detection of a non-Gaussian marginal distribution is an experimental challenge. One of the main reasons for this is that an experiment does not have access to the full probability distributions (here the marginal distribution) of the underlying quantum state, but only to a finite number of samples from these distribution. To illustrate this we have drawn 1000 samples from the marginal distribution which is binned and plotted as a histogram in fig. 9.11. From this it is clear that distinguishing the two sets of sampled data and thus detecting the non-Gaussianity of the quantum state is experimentally hard. Due to this several different methods have been developed in order to quantify the non-Gaussianity and/or non-classicality [Kot et al. 2012; Vogel 2000]. In the following we present a simulation based on the ideas in [Dubost et al. 2012] where the non-Gaussianity is quantified in terms of the cumulants.

The cumulants, κ_n of a distribution can be written as polynomials in the moments, μ_n of the distribution as

$$\kappa_n = \mu_n - \sum_{k=1}^{n-1} \binom{n-1}{k-1} \kappa_k \mu_{n-k}, \quad (9.10)$$

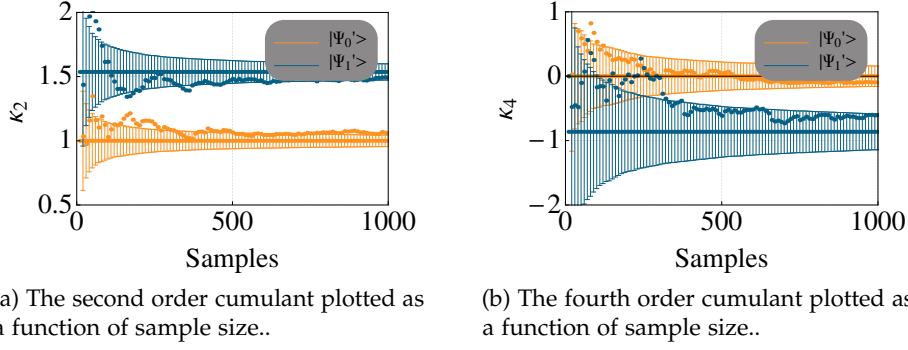


Figure 9.12: Plot of the cumulants as a function of the sample size. Dotted points is data from one realization simulation.

where μ_i denotes the i 'th moment. We will be dealing with the second and fourth cumulants given as

$$\kappa_2 = \mu_2, \quad (9.11a)$$

$$\kappa_4 = \mu_4 - 3\mu_2^2, \quad (9.11b)$$

we note that κ_2 is just the variance. In an experiment we will always be dealing with a finite number of samples from the continuous distribution. This means we can only estimate the cumulants, this is done using k-statistics [Dubost et al. 2012]. The main reason to consider cumulants is outlined in the following: if we measure a signal $Z = X + Y$, where X is the real value of Z and Y is noise which is uncorrelated then cumulants have the marvellous property that

$$\kappa_n(Z) = \kappa_n(X) + \kappa_n(Y). \quad (9.12)$$

The reason this property is interesting is that if we take Y to be a Gaussian function with zero mean value, which is the case for many common noise sources. Then we get

$$\kappa_n(Z) = \kappa_n(X) \quad \text{for } n > 2. \quad (9.13)$$

and the extra noise does then not affect the higher order cumulants. In the following simulation we do not directly use this property for the presented simulation but for the real experiment this feature might be very useful. We simulate our experiment as follows: From the known marginal distributions we draw random samples and use these to calculate the second, and fourth order cumulants, for varying sample sizes. Repeating this 1000 times allows us to calculate the corresponding standard deviations, see fig. 9.12. We start by considering the second order cumulant. From fig. 9.12(a) it is clear that we only need around 250 samples before we can clearly distinguish between the distribution of the expected single polariton state and the expected CSS. We thus expect that careful investigation of κ_2 will allow us to clearly classify our data as originating from either the expected single polariton state or the CSS under the assumptions that these are the only possible distributions. In order to claim that our state is non-Gaussian we need to consider the derivations from the expected mean value of κ_4 for the CSS, in the case considered here we thus need to distinguish it from zero, see fig. 9.12(b). In this case we require around 500 samples to clearly distinguish it from the case of a CSS which has $\kappa_4 = 0$ by two standard deviations. The performed simulations are based on realistic parameters, many already measured, and we can thus conclude that our proposed implementation is experimentally feasible.

Part III
Outlook

Conclusion

In this thesis we have been dealing with the creation and detection of exotic quantum states in an atomic ensemble, with a focus on spin squeezed and single excitation states. We have presented the theory behind the creation of spin squeezed states of the ensemble, via quantum non-demolition measurements. The method is implemented and a spin squeezed state is created and characterized. The characterization is done via a dispersive QND interaction between the light and atoms, which measures the ensemble population difference. By considering the fluctuations of the population difference a scaling analysis is performed allowing us to discriminate different noise sources against each other. First we see a large linear scaling which is a clear signature of atomic projection noise. The experimental challenge in resolving the projection noise is non-trivial. It requires that all parts of the apparatus do not introduce angular fluctuations of the Bloch vector larger than $1/\sqrt{N_{\text{at}}} \approx 0.003$, on the time scale of the whole experiment. By using the measurement based squeezing technique we are able to claim squeezing not only in the angular uncertainties but also in the atomic quadrature operators, introduced in the Holstein-Primakoff approximation. We have presented data showing a noise reduction of -1.7 dB below the projection noise limit. These results together with a theoretical discussion and implementation of a method to detect the non-classicality of the created state have recently been submitted to PRL.

Having created and characterized a spin squeezed state we turn to another non-classical state of the atomic ensemble, a collective single excitation state. We have presented a method, based on the DLCZ protocol, allowing for the realization of this state. This is done by creating a collective single excitation of the atomic ensemble. Detection of a single forward scattered Raman photon heralds the creation of the desired collective single state. This experiment not only has the demands of being projection noise limited, but also requires detection of a single photon together with the capability of doing state selective excitation in the $F' = 4$ hyperfine manifold. Experimental results showing that we can perform the state selective excitation, single photon detection together with the projection noise limited sensitivity have been presented. The preliminary results are supported by a simulation which for *experimentally valid* parameters show that the detected marginal distribution, even with experimental imperfections, retain its non-Gaussian features. From the simulation, an analysis method based on cumulants is presented. This shows that for a reasonable number of samples we will be able to characterize the created quantum state. It is thus clear that the method described is experimentally feasible, and that we in our setup are close to creating and characterizing the single excitation state.

Next steps and improvements

In this chapter I will outline the future plans, not just for the remaining time of my Ph.D. but hopefully some of the ideas and plans will be relevant also on longer time-scale. We will divide this into two separate sections. First we consider the next line of work related to the generation and detection of the single excitation state. This is followed by ideas on how the dipole trapped setup could be improved together with new possible directions. After this an overview of the latest experimental endeavours of a light-atom quantum interface based on a tapered nanofiber is discussed.

11.1 Dipole trapped atomic ensemble

The work presented in this report has a natural short-term goal, namely the creation and characterization of the single excitation state. In order to achieve this goal a few challenges still need to be overcome.

Projection noise: Results showing that we are projection noise limited at the required magnetic bias field of ≈ 20 Gauss was presented. In the data we did not take into account that the excitation beam will induce scattering into different hyperfine levels. Our fear is that the number of induced scattering events and their distribution among the hyperfine levels will fluctuates from shot to shot. This would directly add noise due to the fluctuations of the number of coherent atoms [Oblak 2010, chapt. 6].

Single photon detection: The initial results and calibration presented here are promising. What still needs to be measured is the full transmission of the single photon path, i.e. if there is N_{ph} at the atomic ensemble how many of these gives clicks at the detector.

Detection of non-classicality: We have presented one method, based on the cumulants, which allows us to detect and quantify the non-Gaussianity of the single excitation state. What we are mainly interested in claiming is that the created state is non-classical. Several approaches on how to detect non-Gaussianity and non-Classicality have been proposed [Kot et al. 2012; Vogel 2000]¹. Following the Vogel criteria it can be shown that no matter how big a vacuum fraction that is mixed on top of the single excitation state, the mixed state is still non-classical [Lvovsky et al. 2002]. This is good news, and the challenge is now to detect this non-classicality with a minimum

¹These two papers defines the term non-classicality in different ways, with [Kot et al. 2012] giving the most stringent criteria.

number of samples. One possible approach is to use atomic non-classicality quasiprobabilities as introduced in [Kiesel et al. 2012].

After we (hopefully with great success) have completed the measurements of the single excitation state we are entering an interesting time of the experiment, below we present some of the possible directions that could be taken.

New states: With the possibility to combine the creation of squeezed and discrete excitation states in the atomic ensemble we should be able to create many interesting quantum states. Examples of such states would be squeezed single excitation states (first create the single excitation state and afterwards using a QND measurement to squeeze) and Schrödinger cat states. Here we again see the clear analogy to the photonic system, in which such methods is being used.

Full state tomography: It would be interesting to perform a full state tomography (reconstruct the Wigner function) of both the squeezed state and the single excitation state. Several tries on performing this quantum tomography have been tried, unsuccessfully. The main problem is a inhomogeneous coupling strengths of the microwave over the atomic sample. For the spin squeezed state we are limited by a phase dependent inhomogeneous coupling of the microwave pulse to the atomic ensemble [Oblak 2010, sec. 12.6]. For the single excitation state, which in theory is symmetric, this might not be a problem. Tomography of such states have been performed, also taking into account the curvature of the Bloch sphere [Schmied et al. 2011].

Cavity: Implementing a cavity around the trapped atomic ensemble, would increase the light-atom coupling, which is the central parameter of the interface. Several experiments have shown the creation of spin squeezed states of atomic ensemble in such a cavity based setup [Chen et al. 2011; Leroux et al. 2010; Schleier-Smith et al. 2010]. It has thus been shown that such cavity based light-atom interfaces are useful for quantum state engineering.

Having considered the future perspectives of the experiment dealing with a dipole trapped atomic ensemble, we now consider the case where the light-atom interface is based on a tapered nanofiber.

11.2 Fiber based atomic trap

Besides the experimental apparatus described in this work we² are in the process of setting up a new experiment. Where the light-atom interface will be based on a tapered nanofiber. So far two groups have successfully trapped and detected atoms around a tapered nanofiber [Goban et al. 2012; Vetsch et al. 2010], both are based on the proposal in [Le Kien et al. 2004]. The tapered nanofibers are made by carefully heating and pulling standard optical fibers (diameter of $125\mu\text{m}$) down to sub-wavelength diameters of around 500 nm through an adiabatic transition. It has been shown that making such nanofibers with a high degree of reproducibility and high transmissions (above 95 %) can be done [Ding et al. 2010]. If light is sent through such a sub-wavelength fiber, it will be guided by the fiber core, but it will have a strong evanescent field. Using a combination of red and blue detuned trapping lasers one can form trapping potentials outside the nanofiber. see fig. 11.1. My involvement in the nanofiber experiment have mainly been in the

²Here we is used to describe the subgroup of QUANTOP which I am part of.

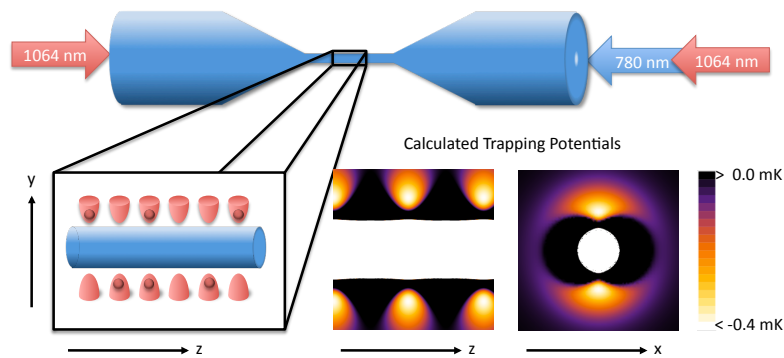


Figure 11.1: The idea behind atomic traps based on tapered nanofibers, shown together with plots of the relevant potentials. The figure has been made by Eva Bookjans and is reprinted here with her permission.

initial stage of the experiment, assembling the vacuum chamber and testing that the nanofiber can withstand the need trap powers. These test showed that the nanofiber gets heated significantly by the trap light making it expand, this work is being summarized in a paper which is in its final stages of preparation. Further more I have been part of the development team³ of the dispersive detection method, based on Lodewyck et al. 2009, which is being implemented into this setup. At the moment the status of the experiment is that a MOT can be created⁴ and are now looking to implement the proposed detection method. Below we present some of the possible experimental directions that could be taken with a full blown light-atom interface based on a tapered nanofiber, none of these are experiments that will be done in the next months, but they serve as an outline of what we are aiming for.

Quantum state engineering: One route to follow would be to implement the ideas outlined in this thesis to the new interface. In respect to quantum state engineering, a key aspect of these traps is that they obtain optical depths of up to ≈ 50 for as few as $N_{\text{at}} \approx 2000$ [Goban et al. 2012]. In comparison to our dipole trap setup where we need $N_{\text{at}} \approx 10^5$ to obtain comparable optical depths. Since classical noise scales quadratically with the number of atoms we would be much less sensitive to classical noise, making it a lot easier to reach the required projection noise limited sensitivity.

Magnetometry: Atomic ensembles are widely used to perform precision measurements of magnetic fields [Romalis et al. 2007]. It has been shown that using spin squeezed atomic states can improve the measurement precision of such magnetometers [Wasilewski et al. 2010]. An atomic magnetometer where the atomic ensemble is trapped around a tapered nanofiber allows for a proof of principle demonstration. Due to the low atom numbers it should be possible to reach the projection noise limit which combined with the high spatial resolution will open up a new class of atomic magnetometers, we note that the low atom numbers, will limit the absolute sensitivity.

Cavity: To improve the light-atom coupling a standard method is to build a cavity around the atoms, this gives an increase in light-atom coupling proportional to the finesse. In the case of nanofiber traps two approaches can be taken, in order to implement cavities. One is to make fiber Bragg mirrors in the fiber and afterwards perform the required pulling. In this

³Together with Jürgen Appel, Jean-Baptiste Béguain and Jörg H. Müller.

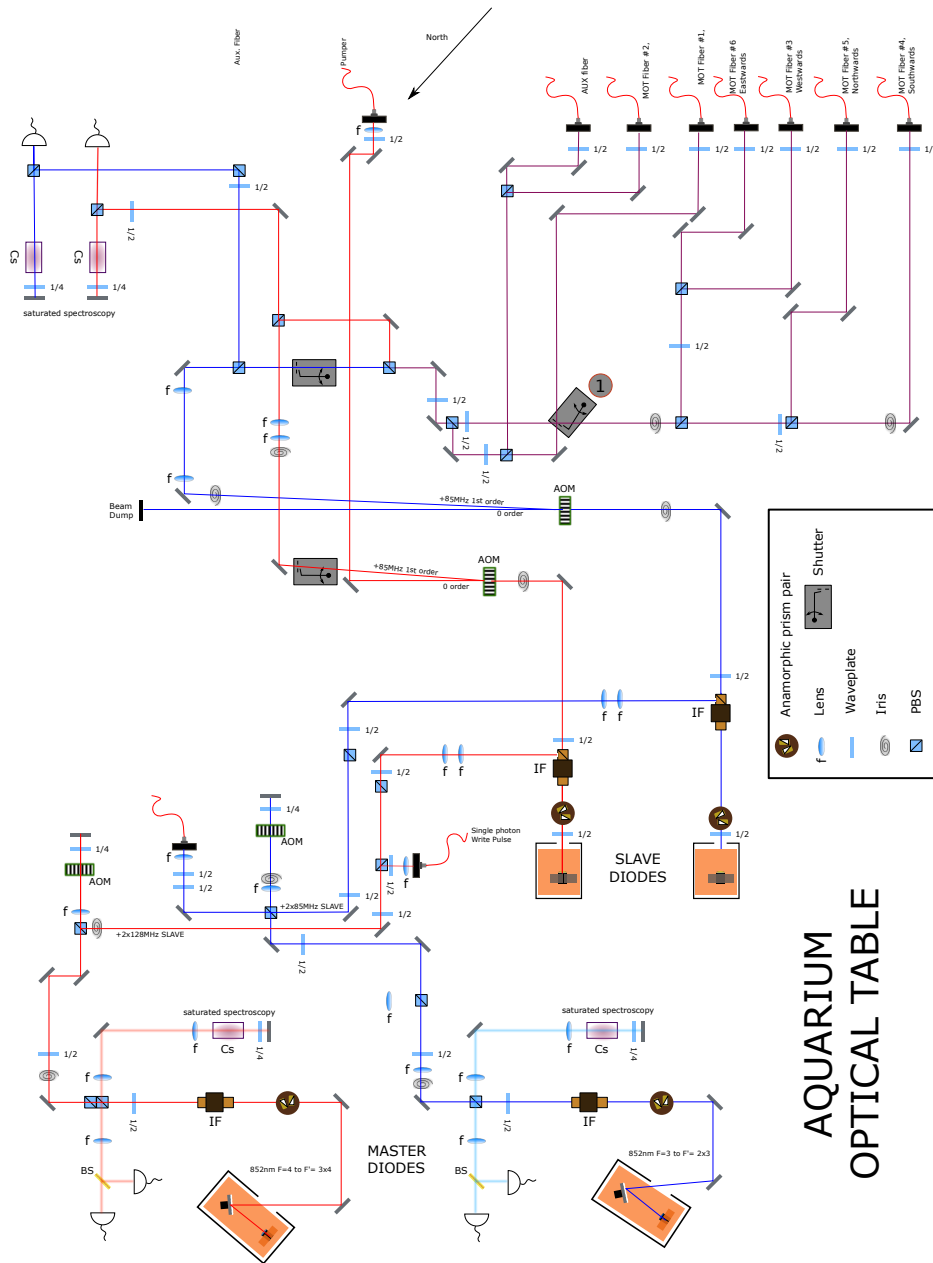
⁴Work here mainly due to Eva Bookjans and Jean-Baptiste Béguain.

way a standard Fabry-Pérot cavity with finesse of $F \approx 80$ is formed around the nanofiber section. It has been shown that, with such a method, the strong coupling regime can be reached [Wuttke et al. 2012]. If we are in the strong coupling regime several interesting cavity quantum electro-dynamics (CQED) experiments could be performed. A different idea would be to create fiber loops [Sumetsky et al. 2006], this can be done by simply twisting the fiber while the two ends are pushed together. Such fiber loop resonators have been shown to have finesse of $F \approx 10$, it is still an open question if such fiber loop resonators will allow one to reach the regime of CQED.

Scalability: Since the nanofiber used for the light-atom interface are made from ordinary fibers it would be relatively easy to consider the interaction between two or more ensembles. Many quantum information processing protocols have been shown in such a dual ensemble setting [Choi et al. 2010; Sherson et al. 2006; Krauter et al. 2011]. All of these would be improved if implemented in the nanofiber based interface.

As it has hopefully become clear from this chapter, there are still many interesting ideas and possibilities for the two considered light-atom interfaces, or to put it in laymans terms, the future looks bright!

Part IV
Appendices



AQUARIUM
OPTICAL TABLE

Figure 12.2: A full schematic for the setup used to generate the MOT, the setup has been around for three generation of graduate students which is clearly seen. The drawing was initially made by Jean-Baptiste Béguin.

Bibliography

- [Appel et al. 2009a] J. Appel, P. J. Windpassinger, D. Oblak, U. B. Hoff, N. Kjærgaard, and E. S. Polzik (2009). Mesoscopic atomic entanglement for precision measurements beyond the standard quantum limit. *P Natl Acad Sci Usa* **106.27**, pp. 10960–10965. DOI: 10.1073/pnas.0901550106.
- [Appel et al. 2007] J. Appel, D. Hoffman, E. Figueroa, and A. I. Lvovsky (2007). Electronic noise in optical homodyne tomography. *Phys. Rev. A* **75.3**, pp. 1–4. DOI: 10.1103/PhysRevA.75.035802.
- [Appel et al. 2009b] J. Appel, A. MacRae, and A. I. Lvovsky (2009). A versatile digital GHz phase lock for external cavity diode lasers. *Measurement Science & Technology* **20.5**, pp. 1–5. DOI: 10.1088/0957-0233/20/5/055302.
- [Brask et al. 2010] J. Brask, I. Rigas, E. Polzik, U. Andersen, and A. Sørensen (2010). Hybrid Long-Distance Entanglement Distribution Protocol. *Phys. Rev. Lett.* **105.16**, pp. 1–4. DOI: 10.1103/PhysRevLett.105.160501.
- [Chen et al. 2011] Z. Chen, J. Bohnet, S. Sankar, J. Dai, and J. Thompson (2011). Conditional Spin Squeezing of a Large Ensemble via the Vacuum Rabi Splitting. *Phys. Rev. Lett.* **106.13**, pp. 1–4. DOI: 10.1103/PhysRevLett.106.133601.
- [Choi et al. 2008] K. S. Choi, H. Deng, J. Laurat, and H. J. Kimble (2008). Mapping photonic entanglement into and out of a quantum memory. *Nature* **452.7183**, pp. 67–71. DOI: 10.1038/nature06670.
- [Choi et al. 2010] K. S. Choi, A. Goban, S. B. Papp, S. J. van Enk, and H. J. Kimble (2010). Entanglement of spin waves among four quantum memories. *Nature* **468.7322**, pp. 412–416. DOI: 10.1038/nature09568.
- [Christensen et al. 2012] S. L. Christensen, J.-B. Béguin, H. L. Sørensen, E. Bookjans, D. Oblak, J. H. Müller, J. Appel, and E. S. Polzik (2012). Towards quantum state tomography of a single polariton state of an atomic ensemble. *arXiv quant-ph:1208.1415v1*.
- [Ding et al. 2010] L. Ding, C. Belacel, S. Ducci, G. Leo, and I. Favero (2010). Ultralow loss single-mode silica tapers manufactured by a microheater. *Applied Optics* **49.13**, pp. 2441–2445. DOI: 10.1364/AO.49.002441.
- [Duan et al. 2001] L. M. Duan, M. D. Lukin, J. I. Cirac, and P. Zoller (2001). Long-distance quantum communication with atomic ensembles and linear optics. *Nature* **414**, pp. 413–418. DOI: 10.1038/35106500.
- [Dubost et al. 2012] B. Dubost, M. Koschorreck, M. Napolitano, N. Behbood, R. J. Sewell, and M. W. Mitchell (2012). Efficient Quantification of Non-Gaussian

- Spin Distributions. *Phys. Rev. Lett.* **108.18**, pp. 1–5. DOI: 10.1103/PhysRevLett.108.183602.
- [Gerry et al. 2005] C. Gerry and P. Knight (2005). *Introductory Quantum Optics*. Cambridge University Press. ISBN: 9780521527354.
- [Goban et al. 2012] A. Goban, K. Choi, D. Alton, D. Ding, C. Lacroûte, M. Pototschnig, T. Thiele, N. Stern, and H. Kimble (2012). Demonstration of a State-Insensitive, Compensated Nanofiber Trap. *Phys. Rev. Lett.* **109.3**, pp. 1–5. DOI: 10.1103/PhysRevLett.109.033603.
- [Grimm et al. 1999] R. Grimm, M. Weidemüller, and Y. B. Ovchinnikov (1999). Optical dipole traps for neutral atoms. *arXiv physics.atom-ph:9902072*.
- [Gross et al. 2010] C. Gross, T. Zibold, E. Nicklas, J. Estève, and M. K. Oberthaler (2010). Nonlinear atom interferometer surpasses classical precision limit. *Nature* **464.7292**, pp. 1165–1169. DOI: 10.1038/nature08919.
- [Hammerer et al. 2010] K. Hammerer, A. S. Sørensen, and E. S. Polzik (2010). Quantum interface between light and atomic ensembles. *Rev. Mod. Phys.* **82.2**, pp. 1041–1093. DOI: 10.1103/RevModPhys.82.1041.
- [Holstein et al. 1940] T. Holstein and H. Primakoff (1940). Field Dependence of the Intrinsic Domain Magnetization of a Ferromagnet. *Physical Review* **58**, pp. 1098–1113. DOI: 10.1103/PhysRev.58.1098.
- [Kiesel et al. 2012] T. Kiesel, W. Vogel, S. L. Christensen, J.-B. Béguin, J. Appel, and E. S. Polzik (2012). Atomic nonclassicality quasiprobabilities. *arXiv quant-ph:1207.3314*.
- [Kitagawa et al. 1993] M. Kitagawa and M. Ueda (1993). Squeezed spin states. *Phys. Rev. A*, pp. 5138–5143. DOI: 10.1103/PhysRevA.47.5138.
- [Kogelnik et al. 1966] H. Kogelnik and T. Li (1966). Laser Beams and Resonators. *Applied Optics* **5.10**, pp. 1550–1567. DOI: 10.1364/AO.5.001550.
- [Kot et al. 2012] E. Kot, N. Grønbech-Jensen, B. M. Nielsen, J. S. Neergaard-Nielsen, E. S. Polzik, and A. Sørensen (2012). Breakdown of the Classical Description of a Local System. *Phys. Rev. Lett.* **108**, pp. 1–5. DOI: 10.1103/PhysRevLett.108.233601.
- [Krauter et al. 2011] H. Krauter, C. A. Muschik, K. Jensen, W. Wasilewski, J. M. Petersen, J. I. Cirac, and E. S. Polzik (2011). Entanglement Generated by Dissipation and Steady State Entanglement of Two Macroscopic Objects. *Phys. Rev. Lett.* **107.8**, pp. 1–5. DOI: 10.1103/PhysRevLett.107.080503.
- [Le Kien et al. 2004] F. Le Kien, V. I. Balykin, and K. Hakuta (2004). Atom trap and waveguide using a two-color evanescent light field around a subwavelength-diameter optical fiber. *Phys. Rev. A* **70.6**, pp. 1–9. DOI: 10.1103/PhysRevA.70.063403.
- [Leonhardt 1997] U. Leonhardt (1997). *Measuring the Quantum State of Light*. Cambridge Studies in Modern Optics. Cambridge University Press. ISBN: 9780521497305.
- [Leroux et al. 2010] I. D. Leroux, M. H. Schleier-Smith, and V. Vuletić (2010). Implementation of Cavity Squeezing of a Collective Atomic Spin. *Phys. Rev. Lett.* **104.7**, pp. 1–4. DOI: 10.1103/PhysRevLett.104.073602.

- [Lodewyck et al. 2009] J. Lodewyck, P. Westergaard, and P. Lemonde (2009). Nondestructive measurement of the transition probability in a Sr optical lattice clock. *Phys. Rev. A* **79.6**, pp. 1–4. DOI: 10.1103/PhysRevA.79.061401.
- [Louchet-Chauvet et al. 2010] A. Louchet-Chauvet, J. Appel, J. J. Renema, D. Oblak, N. Kjaergaard, and E. S. Polzik (2010). Entanglement-assisted atomic clock beyond the projection noise limit. *New J. Phys.* **12.6**, pp. 1–17. DOI: 10.1088/1367-2630/12/6/065032.
- [Lvovsky et al. 2002] A. I. Lvovsky and J. H. Shapiro (2002). Nonclassical character of a statistical mixture of the single-photon and vacuum optical states. *Phys. Rev. A* **65**, pp. 1–6. DOI: 10.1103/PhysRevA.65.033830.
- [Ma et al. 2011] J. Ma, X. Wang, C. P. Sun, and F. Nori (2011). Quantum spin squeezing. *Physics Reports* **509.2-3**, pp. 89–165. DOI: 10.1016/j.physrep.2011.08.003.
- [MacRae et al. 2012] A. MacRae, T. Brannan, R. Achal, and A. Lvovsky (2012). Tomography of a High-Purity Narrowband Photon from a Transient Atomic Collective Excitation. *Phys. Rev. Lett.* **109.3**, pp. 1–4. DOI: 10.1103/PhysRevLett.109.033601.
- [Matsukevich et al. 2004] D. N. Matsukevich and A. Kuzmich (2004). Quantum state transfer between matter and light. *Science* **306.5696**, pp. 663–666. DOI: 10.1126/science.1103346.
- [Metcalf et al. 1999] H. J. Metcalf and P. Van Der Straten (1999). *Laser Cooling and Trapping*. Graduate Texts in Contemporary Physics. Springer. ISBN: 9780387987286.
- [Milonni et al. 2010] P. Milonni and J. Eberly (2010). *Laser Physics*. John Wiley and Sons. ISBN: 9780470409701.
- [Neergaard-Nielsen et al. 2006] J. S. Neergaard-Nielsen, B. M. Nielsen, C. Hettich, K. Mølmer, and E. S. Polzik (2006). Generation of a superposition of odd photon number states for quantum information networks. *Phys. Rev. Lett.* **97.8**, pp. 1–4. DOI: 10.1103/PhysRevLett.97.083604.
- [Nielsen et al. 2000] M. Nielsen and I. Chuang (2000). *Quantum computation and quantum information*. Cambridge Series on Information and the Natural Sciences. Cambridge University Press. ISBN: 9780521635035.
- [Oblak 2010] D. Oblak (2010). *Quantum State Engineering in Cold Cesium Atoms*. PhD thesis. Niels Bohr Institute University of Copenhagen.
- [Ohliger et al. 2012] M. Ohliger and J. Eisert (2012). Efficient measurement-based quantum computing with continuous-variable systems. *Phys. Rev. A* **85.6**, pp. 1–12. DOI: 10.1103/PhysRevA.85.062318.
- [Ourjoumteev et al. 2007] A. Ourjoumteev, H. Jeong, R. Tualle-Brouiri, and P. Grangier (2007). Generation of optical ‘Schrödinger cats’ from photon number states. *Nature* **448.7155**, pp. 784–786. DOI: 10.1038/nature06054.
- [Poizat et al. 1994] J. P. Poizat, F. J. Rock, P. Grangier, and. Roch (1994). Characterization of quantum non-demolition measurements in optics. *Ann. Phys. Fr.* **19.3**, pp. 265–297. DOI: 10.1051/anphys:01994001903026500.
- [Romalis et al. 2007] M. V. Romalis and D. Budker (2007). Optical magnetometry. *Nat Phys* **3**, pp. 227–234. DOI: 10.1038/nphys566.

- [Saffman et al. 2009] M. Saffman, D. Oblak, J. Appel, and E. Polzik (2009). Spin squeezing of atomic ensembles by multicolor quantum nondemolition measurements. *Phys. Rev. A* **79.2**, pp. 1–8. DOI: 10.1103/PhysRevA.79.023831.
- [Sakurai 1978] J. Sakurai (1978). *Advanced quantum mechanics*. Advanced Quantum Mechanics. Addison-Wesley Publishing Company. ISBN: 9780125054027.
- [Schleier-Smith et al. 2010] M. H. Schleier-Smith, I. D. Leroux, and V. Vuletić (2010). Squeezing the collective spin of a dilute atomic ensemble by cavity feedback. *Phys. Rev. A* **81.2**, pp. 1–4. DOI: 10.1103/PhysRevA.81.021804.
- [Schmied et al. 2011] R. Schmied and P. Treutlein (2011). Tomographic reconstruction of the Wigner function on the Bloch sphere. *New J. Phys.* **13.6**, pp. 1–18. DOI: 10.1088/1367-2630/13/6/065019.
- [Schwinger 1952] J. S. Schwinger (1952). *On angular momentum*. Report (U.S. Atomic Energy Commission). U.S. Atomic Energy Commission.
- [Sherson et al. 2006] J. F. Sherson, H. Krauter, R. K. Olsson, B. Julsgaard, K. Hammerer, I. Cirac, and E. S. Polzik (2006). Quantum teleportation between light and matter. *Nature* **443.7111**, pp. 557–560. DOI: 10.1038/nature05136.
- [Sørensen et al. 2001] A. Sørensen and K. Mølmer (2001). Entanglement and Extreme Spin Squeezing. *Phys. Rev. Lett.* **86.20**, pp. 4431–4434. DOI: 10.1103/PhysRevLett.86.4431.
- [Steck 2010] D. A. Steck (2010). Alkali D Line Data, pp. 1–31.
- [Sumetsky et al. 2006] M. Sumetsky, Y. Dulashko, J. M. Fini, A. Hale, and D. J. DiGiovanni (2006). The microfiber loop resonator: theory, experiment, and application. *J. Lightwave Technol.* **24.1**, pp. 242–250. DOI: 10.1109/JLT.2005.861127.
- [Vetsch et al. 2010] E. Vetsch, D. Reitz, G. Sagué, R. Schmidt, S. T. Dawkins, and A. Rauschenbeutel (2010). Optical Interface Created by Laser-Cooled Atoms Trapped in the Evanescent Field Surrounding an Optical Nanofiber. *Phys. Rev. Lett.* **104.20**, pp. 1–4. DOI: 10.1103/PhysRevLett.104.203603.
- [Vogel 2000] W. Vogel (2000). Nonclassical States: An Observable Criterion. *Phys. Rev. Lett.* **84.9**, pp. 1849–1852. DOI: 10.1103/PhysRevLett.84.1849.
- [Walls et al. 2008] D. F. Walls and G. J. Milburn (2008). *Quantum optics*. 2nd ed. Springer, Berlin : ISBN: 9783540285731 9783540285748.
- [Wasilewski et al. 2010] W. Wasilewski, K. Jensen, H. Krauter, J. J. Renema, M. V. Balabas, and E. S. Polzik (2010). Quantum Noise Limited and Entanglement-Assisted Magnetometry. *Phys. Rev. Lett.* **104.13**, pp. 1–4. DOI: 10.1103/PhysRevLett.104.133601.
- [Windpassinger et al. 2009] P. Windpassinger and M. Kubasik (2009). Ultra low-noise differential ac-coupled photodetector for sensitive pulse detection applications. *Measurement Science & Technology* **20**, pp. 1–7.
- [Windpassinger 2008] P. Windpassinger (2008). *Non-destructive quantum state measurements and spin squeezing*. PhD thesis. Niels Bohr Institute University of Copenhagen.

- [Wineland et al. 1994] D. Wineland, J. Bollinger, and W. Itano (1994). Squeezed atomic states and projection noise in spectroscopy. *Phys. Rev. A* **50.1**, pp. 67–88. doi: 10.1103/PhysRevA.50.67.
- [Wu et al. 1986] L.-A. Wu, H. J. Kimble, J. L. Hall, and H. Wu (1986). Generation of Squeezed States by Parametric Down Conversion. *Phys. Rev. Lett.* **57**, pp. 2520–2523. doi: 10.1103/PhysRevLett.57.2520.
- [Wuttke et al. 2012] C. Wuttke, M. Becker, S. Brueckner, M. Rothhardt, and A. Rauschenbeutel (2012). Nanofiber Fabry-Perot microresonator for nonlinear optics and cavity quantum electrodynamics. *Opt Lett* **37.11**, pp. 1949–1951. doi: 10.1364/OL.37.001949.